Strahlinduzierte Depolarisation am transversal polarisierten Wasserstofftarget des HERMES-Experiments

Beam-Induced Depolarisation at the HERMES Transversely Polarised Hydrogen Target

Den Naturwissenschaftlichen Fakultäten
der Friedrich-Alexander-Universität Erlangen-Nürnberg
zur
Erlangung des Doktorgrades

vorgelegt von

Philip Tait

aus

Sheffield

Als Dissertation genehmigt von den Naturwissenschaftlichen
Fakultäten der Universität Erlangen-Nürnberg

Tag der mündlichen Prüfung: 24. Februar 2006

Vorsitzender der Promotionskommission: Prof. Dr. D.-P. Häder

Erstberichterstatter: Prof. Dr. E. Steffens

Zweitberichterstatter: Prof. Dr. U. Katz

Contents

Zusammenfassung

I would rather decline two drinks than one German adjective.

A friend of Mark Twain's in Heidelberg

Diese Arbeit beschäftigt sich mit dem polarisierten Wasserstofftarget des HERMES-Experiments bei DESY in Hamburg. Das HERMES-Target basiert auf der Hyperfeinaufspaltung von Wasserstoffniveaus in einem externen Magnetfeld und stellt kernpolarisierten Wasserstoff für das HERMES Experiment zur Verfügung. Insbesondere wird in dieser Arbeit das Phänomen der strahlinduzierten Depolarisation untersucht. Der HERA Elektronenstrahl besteht aus kurzen Bündeln, die ein hochfrequenzes Magnetfeld erzeugen. Eine Fourier-Entwicklung dieser Bündel führt zu eine Serie von Harmonischen, basierend auf der Grundfrequenz von etwa 10.4 MHz. Diese Harmonischen können einen Übergang zwischen Hyperfeinniveaus bewirken. Nur durch eine sorgfältige Auswahl des äußeren Magnetfelds können diese unerwünschten Übergänge und die daraus resultierende Depolarisation vermieden werden.

Messungen dieser Resonanzen wurden schon in der ersten HERMES-Betriebsperiode 1995-2000 präsentiert. Im Jahre 2001 wurde ein Umbau des Targetbereichs vorgenommen, um HERMES zum ersten Mal mit *senkrecht* zur Strahlrichtung polarisiertem Wasserstoff zu versorgen. Dieser Umbau gibt HERMES Zugang zur sogenannten „Transversity“, führt aber zu zusätzlichen Resonanzen im Target, die vorher durch Auswahlregeln verboten waren. Die Messung und Minimierung dieser „Sigma-Resonanz“ werden vorgestellt.

Eine Besonderheit des HERMES-Experiments ist seine neuartige Speicherzelle, die es ermöglicht, dass Atome mehrmals durch den HERA-Strahl fliegen können. Eine genaue Beschreibung der strahlinduzierten Depolarisation muss deshalb die Geometrie der Speicherzelle und die Verteilung des Magnetfelds in der Zelle berücksichtigen. Rechnungen zur Depolarisation erfolgen durch Lösung der zeitabhängigen Schrödingergleichung mittels Störungstheorie erster Ordnung. Es wurden ein einfaches, analytisches Modell und eine Molekularfluß-Monte-Carlo Simulation benutzt, um die genaue Form der Resonanzen vorherzusagen. Die erstmalige Messung der Resonanzen mit einem transversalen Magnetfeld werden präsentiert und mit den Simulationen verglichen.

Summary

This thesis describes the polarised hydrogen target of the HERMES experiment at DESY in Hamburg. The HERMES target is based on hyperfine-splitting of hydrogen in an external magnetic field and provides nuclear-polarised hydrogen for the HERMES experiment. Particular emphasis is placed on the phenomenon of beam-induced depolarisation. The HERA electron beam consists of short bunches which produce a high-frequency magnetic field. A Fourier analysis of these bunches leads to a series of harmonics, based on the fundamental frequency of roughly 10.4 MHz, which can cause a transition between hyperfine states of the target atoms. Only through careful setting of the external magnetic field is it possible to avoid these transitions and the resulting depolarisation of the target gas.

Measurements of these resonances were made during the first HERMES run 1995-2000. The target region was modified in 2001 to allow HERMES to use hydrogen polarised *perpendicularly* to the direction of the electron beam. This modification gave HERMES access to the so-called “Transversity” distribution for the first time, but also allows additional resonances in the target, which were previously forbidden by selection rules. The measurement and minimisation of these “Sigma resonances” are presented.

A distinctive feature of the HERMES experiment is its novel storage cell which allows target atoms to make multiple passes of the HERA beam. An exact description of beam-induced depolarisation must therefore consider the geometry of the storage cell and the distribution of the magnetic field throughout the cell. Calculations of the depolarisation can be made by solving the time-dependent Schrödinger equation using first-order perturbation theory. A simple analytical model and a molecular-flow Monte-Carlo are used to predict the exact shape of the resonances. The first measurements of the resonances with a transverse magnetic holding field are presented and compared with the simulations.

Chapter 1

Introduction

Als man ankam wollte man werden, die Geschichte schreiben, die Doofen sollen sterben, der Plan als man damals nach Hamburg kam.

M. Wiebusch

1.1 The Hera Accelerator

The HERA accelerator at DESY in Hamburg was built to allow the structure of the proton to be studied. HERA consists of a superconducting proton storage ring which is capable of a final energy of 920 GeV, and an electron[1] storage ring which can reach an energy of 27.5 GeV. The ring is roughly 6.3 km long, so that the highly-relativistic accelerated particles make over 47000 revolutions per second. The protons and electrons are brought to collision at two points in the ring, and the resulting reactions can be observed by the experiments H1 and ZEUS. The electron beam can become transversely polarised through emission of synchrotron radiation, a process known as the Sokolov-Ternov effect. Spin-rotators, situated before and after an experiment allow the experiment to use longitudinally polarised electrons. Such a scheme was first used at HERA for the HERMES experiment, and then also installed for H1 and ZEUS during the 2001 upgrade. As HERMES uses only the electron beam from HERA, we will concentrate on the properties of the electron storage ring for the remainder of this section.

1.1.1 Parameters of the Electron Storage Ring

The electrons must be accelerated to 12 GeV before they enter the HERA ring [Sch84]. This is achieved by passing the electrons through "a complex maze of pre-accelerators" [HER03] with increasing energy before they are finally injected from the PETRA ring into the HERA ring. Once the HERA electron ring is filled with sufficient electrons, they can be brought to the final energy. The HERA electron ring consists of four straight sections, each 360 m long and four curved sections with a radius of 779 m. The straight sections are home to the four experiments, and the north and south straight sections contain also the RF cavities used to accelerate the electron beam.

The RF cavities operate at 499.667 MHz, and as a result the electrons are contained in short bunches, with a typical length of around 9 mm. The storage ring is operated so that 220 equally spaced buckets can be used, but typically only 180 of these buckets are filled.

[1] HERA can be used with either electrons or positrons. Throughout this work the term electrons is used, irrespective of how the machine was configured.

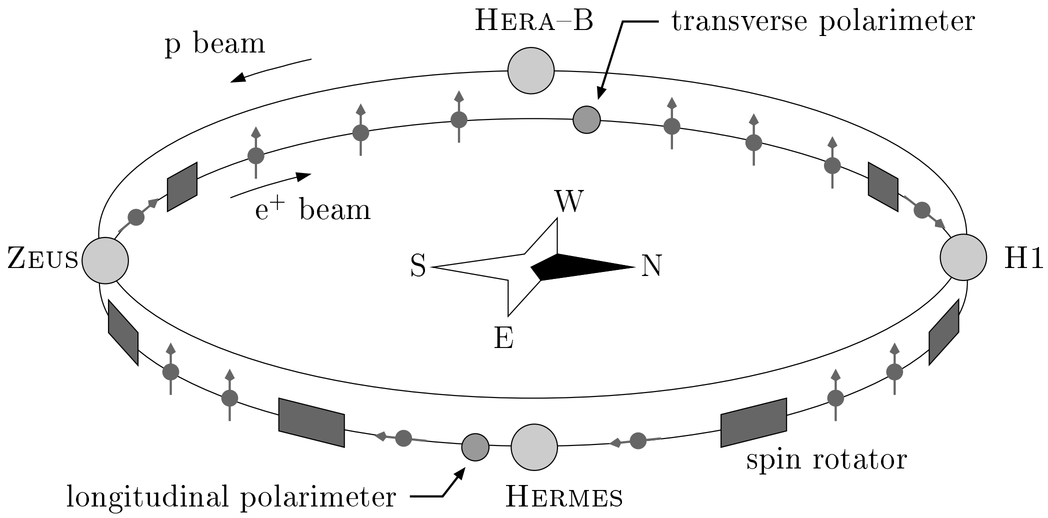

Figure 1.1: A schematic view of the HERA accelerator, showing the positions of the four experimental areas and the electron beam polarisation orientation throughout the ring. The electron and proton beams are brought to collision at the ZEUS and H1 experiments. The polarisation of the electron beam is measured at two points in the ring by the transverse [Bar93] and longitudinal [Bec02] polarimeters.

The frequency between two buckets (known as the bunch frequency) is 10.4097MHz, which corresponds to a distance of roughly 28.8 m between successive bunches. The extremely short bunches, which are 9.3 mm long, enable high luminosities for the experiments using colliding beams as the electron bunches are brought into collision with similarly tightly bunched protons.

The stored electrons can be lost due to scattering on residual gas particles in the beam tube or by collisions within the beam. The beam current drops therefore approximately exponentially with time, from a starting point of up to 50 mA. After around 12 hours the beam is kicked out of the ring (dumped) and refilled.

1.2 The Hermes Experiment

The HERMES experiment uses the polarised electron beam of the HERA accelerator together with a fixed polarised gas target. The energy of the accelerated electrons is sufficient to probe deep into the nucleons of the target and to interact with a quark. This process is known as Deep-Inelastic Scattering (DIS), and at HERMES allows the spin-properties of the quarks to be examined. The gas target is internal to the HERA electron ring, and will be described in detail in section 3. HERMES has been running since 1995, and has observed many millions of DIS events from polarised hydrogen, deuterium and ^{3}He. The first run lasted from 1995 until 2000, and during this time the target spin was aligned parallel to the electron beam. Since 2001 the target spin has been aligned perpendicular to the electron beam, which, as we shall see in the next section, allows measurements to be made which are not only new to HERMES, but new to the whole field.

1.2.1 Spin-Dependent Quark Distributions

The quark structure of the proton can be described in Quantum Chromo Dynamics (QCD) by three structure functions. These are the unpolarised quark distribution $q(x)$, the quark helicity distribution $\Delta q(x)$ and the so-called "transversity" or transverse polarisation distribution $\delta q(x)$. x is here the Bjorken scaling variable, and can be interpreted as the fraction of the nuclear momentum carried by the struck quark. The quark distributions can be given a probabilistic interpretation.

- $q(x)$: This function describes the probability of a quark in the proton carrying the momentum fraction x. This function is well known from unpolarised DIS experiments, such as H1 and ZEUS. For polarised quarks it is the sum of the two opposite spin states.

$$q(x) = q^{\stackrel{\rightarrow}{\Rightarrow}}(x) + q^{\stackrel{\leftarrow}{\Rightarrow}}(x) \tag{1.1}$$

  where $\rightarrow$ represents the spin of the quark, and $\Rightarrow$ the spin of the target proton.

- $\Delta q(x)$: The spin of a quark in a proton can be aligned parallel, or antiparallel to the nuclear spin. This function represents the difference in probability of these two cases, under the condition that the target spin is parallel to the direction of the electron beam.

$$\Delta q(x) = q^{\stackrel{\rightarrow}{\Rightarrow}}(x) - q^{\stackrel{\leftarrow}{\Rightarrow}}(x) \tag{1.2}$$

  As the electron beam is longitudinally polarised, a virtual photon can only be absorbed by a quark if the quark spin is antiparallel to the spin of the photon. The main aim of HERMES run 1 was to measure $\Delta q(x)$ using the asymmetry in DIS cross-section which arises from this requirement [Air04]. Other measurements of this structure function have been made at other experiments [SMC97, E143].

- $\delta q(x)$: If the target proton has a spin which is perpendicular to the electron beam, then the quark distribution is described by the transverse polarisation distribution function, $\delta q(x)$. This function is also known as "Transversity". Analogously to its longitudinal polarisation counterpart $\Delta q(x)$, it can be expressed as

$$\delta q(x) = q^{\uparrow\Uparrow}(x) - q^{\uparrow\Downarrow}(x) \tag{1.3}$$

  At first sight one might ask what difference there is between $\Delta q(x)$ and $\delta q(x)$, for all that we have done is to rotate the proton spin by 90° (or, depending on your viewpoint, have changed the direction of our probe by 90°). So why should this seemingly trivial change require a new distribution function? Indeed, in the non-relativistic case δq and Δq are identical, but as the electrons used to probe the proton are highly relativistic, separate descriptions are needed.

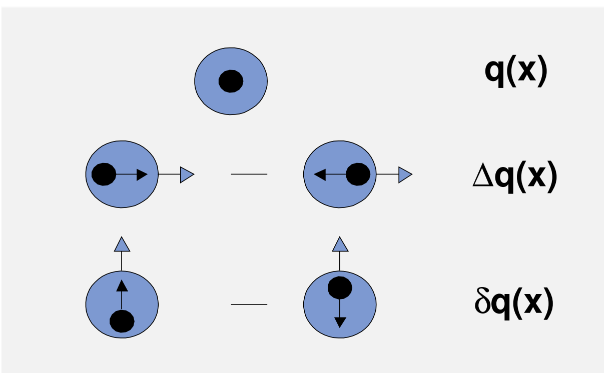

Figure 1.2: The probabilistic interpretations of the three leading twist quark distribution functions.

Having accepted that $\delta q(x)$ is worth measuring, one could ask how it is possible for HERMES to measure this function, or why a longitudinally polarised electron should care whether the target proton has spin pointing up or down? From a simple parton model one would expect that the DIS cross-section would be independent of the transverse orientation of the target spin. This turns out to be not exactly the case, once detailed QCD calculations are made, and inclusive measurements of longitudinally polarised electrons on transversely polarised targets do show a target-spin asymmetry, which can be used to find the polarised structure function g_2. This function has no probabilistic interpretation, and can only be measured if both the target protons and the electron beam are polarised. Measurements of g_2 have already been made measured at the E155 experiment [E155]. Thus this function, which was the original motivation behind a transversely polarised target at HERMES [Her93], is no longer the sole point of interest of a transversely polarised target.

Transversity cannot be observed in inclusive DIS processes with a quark as this would require a helicity flip of both the electron and proton, which is forbidden. A process in which helicity is flipped is known as a "chiral odd" process. HERMES can therefore only measure $\delta q(x)$ if it is combined with another chiral odd function, such as the Collins fragmentation function. Fragmentation functions are used in semi-inclusive DIS to describe the probability of a struck quark of a certain flavour fragmenting into a certain hadron type. The Collins function describes the fragmentation for transversely polarised quarks and produced hadrons which are unpolarised. The semi-inclusive cross section contains products of distribution functions and fragmentation functions. The product of transver-

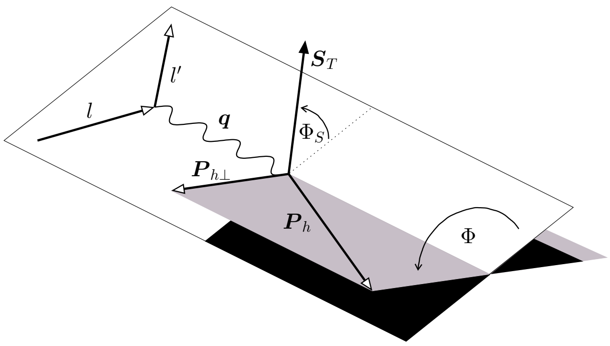

Figure 1.3: A schematic diagram of deep inelastic scattering of an electron (labelled l) on a proton, P, which is transversely polarised. See text for details.

sity and Collins function arises in the cross section with a sine modulation of the sum of the two azimuthal angles ϕ and ϕ_s, as defined in figure 1.3. The momentum vectors of the incoming and scattered electron form a plane, known as the "scattering plane". The target spin, shown here as S_T forms an angle ϕ_S to this plane. The struck quark is detected as a hadron, with momentum P_h. The hadron scattering plane is defined by the momentum vector P_h and the momentum vector of the virtual photon, q. The angle between the hadron and electron scattering planes is then ϕ.

In order to extract the relevant sine amplitudes of the azimuthal cross-section which contains the product of $\delta q(x)$ with the Collins fragmentation function, it is common to measure azimuthal asymmetries:

$$A_{UT}(\phi, \phi_S) = \frac{1}{S_\perp} \frac{N^\uparrow(\phi, \phi_S) - N^\downarrow(\phi, \phi_S)}{N^\uparrow(\phi, \phi_S) + N^\downarrow(\phi, \phi_S)} \tag{1.4}$$

where $\uparrow$ and $\downarrow$ refer to the orientation of the target spin, the indices $_{UT}$ means that the beam is unpolarised and the target transversely polarised, and $S_\perp$ is the target polarisation.

In order to investigate the properties of transversity, the HERMES spectrometer must be used to its full capability, for the scattered electron and produced hadron must both be correctly identified, and their paths and momenta must be accurately reconstructed.

More complete and much less naive discussions of spin-dependent quark distributions at HERMES can be found in [Sei04, Die04]. A review of the whole topic of transversity can be found at [Bar01]. The first published results of the azimuthal asymmetries are presented in [Her04].

The measurement of transversity is the "headline" event for HERMES run II, and the reason for the transversely polarised target, but is only a part of the overall HERMES program. An overview of the many and varied studies of nuclear and sub-nuclear physics at HERMES, including of course transverse polarisation, can be found in [Rit02].

1.2.2 The Hermes Spectrometer

The HERMES spectrometer is described in detail in [Ack98], and is shown schematically in figure 1.4. It is a forward spectrometer with a dipole magnet providing an integral field of 1.3 Tm. The spectrometer is constructed as two identical halves mounted above and below the beam pipes. The acceptance covers angles of ±170 mrad in the horizontal direction, and ±140 mrad in the vertical direction.

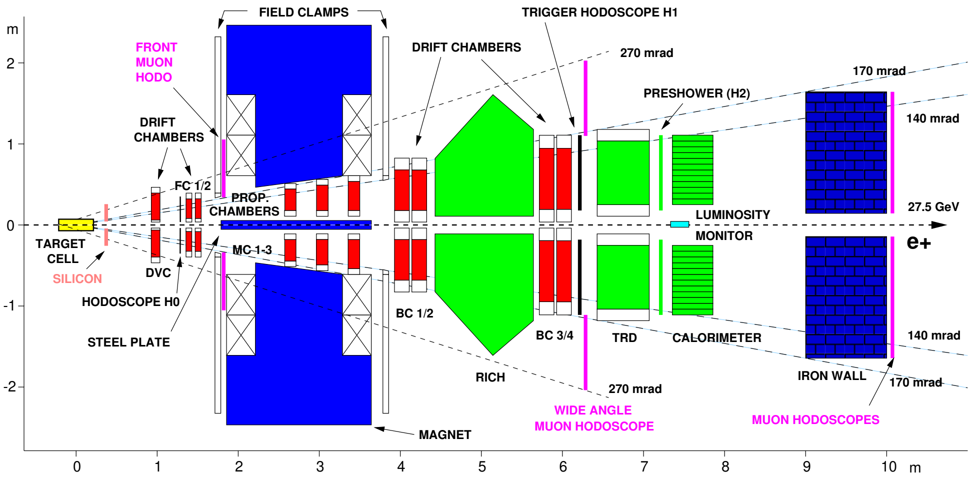

Figure 1.4: A side view of the HERMES spectrometer, showing the various detectors. Tracking chambers (coloured red) before, inside and behind the magnet are used to measure the paths of reaction products from the cell, whilst several detectors (coloured green) are predominantly used for particle identification.

1.2.3 Outline for the Thesis

The HERA accelerator, the transverse polarisation distribution and the HERMES spectrometer are important for this thesis, for they dictate the circumstances in which the polarised target will work. The rest of this thesis will concentrate on the polarised target, but builds upon the framework described here. We shall see that the requirement of transverse target polarisation, needed to measure δq, and the requirement of tightly packed electron bunches, needed to drive the collider experiments, combine to create a particularly interesting effect in the polarised target, that of beam-induced depolarisation. But first we must understand how hydrogen atoms can be polarised, and exactly how the HERMES polarised target works. This will take up the next two chapters. Then we will be able to discuss in full detail the consequences of this effect, and the efforts made to keep it under control.

Chapter 2

Theory of the Hydrogen Atom in a Magnetic Field

If you ever tried to set your washing machine to "Hyperfeinwäsche", you might just be an atomic physicist

2.1 Hyperfine Structure of Hydrogen

The energy levels of a hydrogen atom are governed by the Coulomb interaction between the proton and electron. The Hamiltonian describing such an atom is

$$\mathcal{H}_C = \frac{\mathbf{P^2}}{2\mu} - \frac{q^2}{4\pi\epsilon_0 r}. \tag{2.1}$$

A more exact description of the energy levels must also consider the contributions resulting from the spins of the electron and proton. Here we will consider only the ground state of hydrogen, with principal quantum number $n = 1$, and orbital angular momentum $l = 0$. Thus no interactions concerning the orbital angular momentum of the electron (known as fine-splitting) need to be considered. The modified Hamiltonian, considering spin-related effects in an external field $\mathbf{B}$ is

$$\mathcal{H} = \mathcal{H}_C + \mathcal{A}\mathbf{I}.\mathbf{S} + \frac{\mathbf{g_s}\mu_\mathbf{B}}{\hbar}\mathbf{B}.\mathbf{S} - \frac{\mathbf{g_I}\mu_\mathbf{N}}{\hbar}\mathbf{B}.\mathbf{I}. \tag{2.2}$$

In the first additional term, $\mathcal{A}$ is a constant describing the strength of the interaction between the proton and electron spins. The second and third additional terms concern the interactions between the external field and the electron ($\mathbf{S}$) and proton ($\mathbf{I}$) spins respectively. $\mu_B = \frac{e\hbar}{2m_e}$ is the Bohr Magneton, and μ_N is its proton equivalent. $g_s \simeq 2.0023$ and $g_I \simeq 5.5857$ are the respective gyro-magnetic factors.

In the representation $|\,\mathbf{S^2}, \mathbf{I^2}; \mathbf{m_S}, \mathbf{m_I}\,\rangle$ (where m_S and m_I refer to the operators S_z and I_z), a basis for the Hamilton operator is given by

$$|\uparrow +\rangle \quad , \quad |\uparrow -\rangle \quad , \quad |\downarrow -\rangle \quad , \quad |\downarrow +\rangle \tag{2.3}$$

where the arrow refers to the electron and the sign to the proton spin. Using this basis, we can then expand the terms $\mathbf{S}.\mathbf{I}, \mathbf{B}.\mathbf{S}, \mathbf{B}.\mathbf{I}$ in a matrix form, for

$$\mathbf{S}.\mathbf{I} = S_z I_z + \frac{1}{2}\left(S_+ I_- + S_- I_+\right) \tag{2.4}$$

where $I_\pm = I_x \pm iI_y$ and $S_\pm = S_x \pm iS_y$. Taking into account that $S_z = I_z = \pm\frac{\hbar}{2}$, one can write equation 2.4 in the following matrix representation:

$$\mathbf{S}\cdot\mathbf{I} = \frac{\hbar^2}{4}\begin{pmatrix} 1 & 0 & 0 & 0 \\ 0 & -1 & 0 & 2 \\ 0 & 0 & 1 & 0 \\ 0 & 2 & 0 & -1 \end{pmatrix} \tag{2.5}$$

For the terms of 2.2 representing the interactions with the external magnetic field, we have:

$$\mathbf{S}\cdot\mathbf{B} = S_zB_z + \frac{1}{2}S_+(B_x - iB_y) + \frac{1}{2}S_-(B_x + iB_y) \tag{2.6}$$

and correspondingly

$$\mathbf{I}\cdot\mathbf{B} = I_zB_z + \frac{1}{2}I_+(B_x - iB_y) + \frac{1}{2}I_-(B_x + iB_y) \tag{2.7}$$

In case of a static magnetic field along the z direction, $\mathbf{B} = (0, 0, B)$ and defining the variable $x = \frac{B}{B_C}$, the matrix representations of (2.6) and (2.7) are:

$$\frac{\mathbf{B}}{B_C}\cdot\mathbf{S} = \frac{\hbar}{2}\begin{pmatrix} x & 0 & 0 & 0 \\ 0 & x & 0 & 0 \\ 0 & 0 & -x & 0 \\ 0 & 0 & 0 & -x \end{pmatrix} \tag{2.8}$$

and

$$\frac{\mathbf{B}}{B_C}\cdot\mathbf{I} = \frac{\hbar}{2}\begin{pmatrix} x & 0 & 0 & 0 \\ 0 & -x & 0 & 0 \\ 0 & 0 & -x & 0 \\ 0 & 0 & 0 & x \end{pmatrix} \tag{2.9}$$

If $B_c = \frac{\mathcal{A}\hbar^2}{g_s\mu_B}$, then equation 2.2 can be written in the form

$$\mathcal{H} = \mathcal{H}_C + \mathcal{A}\hbar^2\left[\frac{\mathbf{S}\cdot\mathbf{I}}{\hbar^2} + \frac{\mathbf{B}}{B_C}\cdot\left(\frac{\mathbf{S}}{\hbar} - \varepsilon\frac{\mathbf{I}}{\hbar}\right)\right] \tag{2.10}$$

with $\varepsilon = \frac{g_I\mu_N}{g_s\mu_B}$. This leads to the static Hamiltonian representing the hyperfine interactions, $\mathcal{H}_0^{\mathrm{st}}$.

$$\mathcal{H}_0^{\mathrm{st}} = \frac{\mathcal{A}\hbar^2}{4}\begin{pmatrix} 1+2x(1-\varepsilon) & 0 & 0 & 0 \\ 0 & -1+2x(1+\varepsilon) & 0 & 2 \\ 0 & 0 & 1-2x(1-\varepsilon) & 0 \\ 0 & 2 & 0 & -1-2x(1+\varepsilon) \end{pmatrix} \tag{2.11}$$

Since the matrix (2.11) is not diagonal, the basis (2.3) does not represent a set of eigenstates of (2.10). The diagonalisation of (2.11) can be performed by means of an orthogonal transformation:

$$\mathcal{H}_1^{\mathrm{st}} = U_0\mathcal{H}_0^{\mathrm{st}}U_0^T \tag{2.12}$$

where the orthonormal matrix U_0 is given by

$$U_0 = \begin{pmatrix} 1 & 0 & 0 & 0 \\ 0 & \cos\theta & 0 & \sin\theta \\ 0 & 0 & 1 & 0 \\ 0 & -\sin\theta & 0 & \cos\theta \end{pmatrix} \tag{2.13}$$

In order that the resulting matrix is diagonal, the relation

$$2x\,(1+\varepsilon)\cos\theta\sin\theta = \cos^2\theta - \sin^2\theta \tag{2.14}$$

must be fulfilled. This is equivalent to the equations

$$\cos 2\theta \;=\; \frac{x(1+\varepsilon)}{\sqrt{x^2(1+\varepsilon)^2+1}} \qquad \sin 2\theta \;=\; \frac{1}{\sqrt{x^2(1+\varepsilon)^2+1}} \tag{2.15}$$

relating x and θ, which can be combined to give the relation

$$\tan 2\theta = \frac{1}{x\,(1+\varepsilon)}. \tag{2.16}$$

The diagonal elements, and therefore the eigenenergies of $\mathcal{H}_1^{\mathrm{st}}$ are:

$$\begin{aligned} E_1 &= \tfrac{E_{\mathrm{HFS}}}{4}(1+2x(1-\varepsilon)) & E_3 &= \tfrac{E_{\mathrm{HFS}}}{4}(1-2x(1-\varepsilon)) \\ E_2 &= \tfrac{E_{\mathrm{HFS}}}{4}(-1+2\sqrt{x^2(1+\varepsilon)^2+1}\,) & E_4 &= \tfrac{E_{\mathrm{HFS}}}{4}(-1-2\sqrt{x^2(1+\varepsilon)^2+1}\,) \end{aligned} \tag{2.17}$$

where $E_{\mathrm{HFS}} = \mathcal{A}\hbar^2$. The hydrogen hyperfine splitting is usually known in terms of the

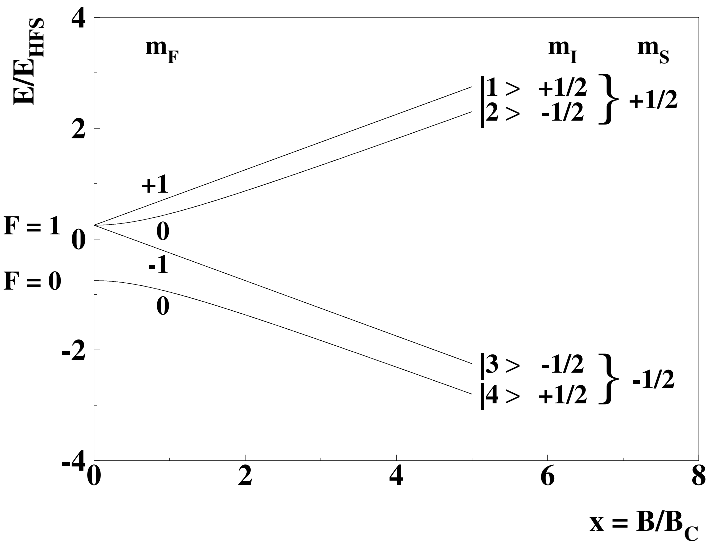

Figure 2.1:
Hyperfine energy levels of hydrogen plotted as functions of the magnetic holding field (Breit-Rabi diagram). The energies are scaled to the hyperfine energy E_{HFS} and the field values to the critical field B_C.

frequency $\nu_{\mathrm{HFS}} = \frac{E_{\mathrm{HFS}}}{2\pi\hbar} = 1420.4\,\mathrm{MHz}$. In figure 2.1 the hydrogen hyperfine eigenenergies are plotted as functions of the variable x.

The new basis is composed by eigenstates of the Hamilton operator.

$$\begin{aligned} |\,1\,\rangle &= |\!\uparrow +\rangle & |\,3\,\rangle &= |\!\downarrow -\rangle \\ |\,2\,\rangle &= \cos\theta\,|\!\uparrow -\rangle + \sin\theta\,|\!\downarrow +\rangle & |\,4\,\rangle &= \cos\theta\,|\!\downarrow +\rangle - \sin\theta\,|\!\uparrow -\rangle \end{aligned} \tag{2.18}$$

2.1.1 Polarisation Definitions

The electron and nuclear polarisations (P_e and P_z) of the state $|\,i\,\rangle$ are given by the expectation values of the operators $\frac{2}{\hbar}S_z$ and $\frac{2}{\hbar}I_z$ respectively. For a sample of atoms one has:

$$P_e \;=\; \sum_{i=1}^{4} n_i\,\langle\, i\,|\,\frac{2}{\hbar}S_z\,|\,i\,\rangle = n_1 - n_3 + (n_2 - n_4)\cos 2\theta \tag{2.19}$$

$$P_z \;=\; \sum_{i=1}^{4} n_i\,\langle\, i\,|\,\frac{2}{\hbar}I_z\,|\,i\,\rangle = n_1 - n_3 - (n_2 - n_4)\cos 2\theta \tag{2.20}$$

where n_i is the relative population of state $|\, i\,\rangle$, undergoing the following normalisation condition:

$$\sum_i n_i = 1 \tag{2.21}$$

P_e and P_z for the different hydrogen hyperfine states are plotted in figure 2.2 as function of the applied magnetic field.
The critical field B_C marks the boundary between two field regions:

- $B \ll B_C \Longleftrightarrow \theta \to \frac{\pi}{4}$, Zeeman limit.
  The interaction with the external field can be treated perturbatively. A basis is given by the eigenstates of $|\, F, m_F\,\rangle$. The pure states $|\,1\,\rangle$ and $|\,3\,\rangle$ are polarised ($P_e = P_z = \pm 1$), whereas $|\,2\,\rangle$ and $|\,4\,\rangle$ are unpolarised ($P_e = P_z \simeq 0$):

$$\begin{aligned}
|\,1\,\rangle &\simeq |\,F=1, m_F=+1\,\rangle &=& \;|\uparrow +\rangle \\
|\,2\,\rangle &\simeq |\,F=1, m_F=0\,\rangle &=& \;\frac{1}{\sqrt{2}}(|\uparrow -\rangle + |\downarrow +\rangle) \\
|\,3\,\rangle &\simeq |\,F=1, m_F=-1\,\rangle &=& \;|\downarrow -\rangle \\
|\,4\,\rangle &\simeq |\,F=0, m_F=0\,\rangle &=& \;\frac{1}{\sqrt{2}}(|\uparrow -\rangle - |\downarrow +\rangle)
\end{aligned} \tag{2.22}$$

- $B \gg B_C \Longleftrightarrow \theta \to 0$, Paschen-Back limit.
  The spin-spin interaction can be treated perturbatively. Now the eigenstates can be represented by the basis (2.3) where all the states are polarised.

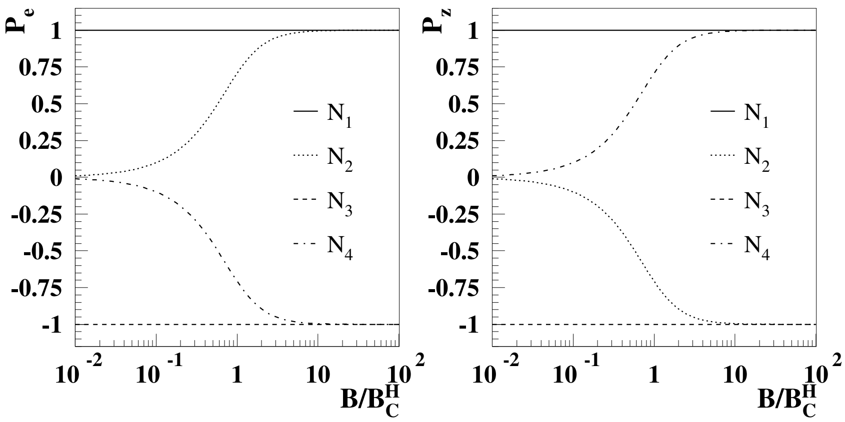

Figure 2.2:
The electron (left) and nuclear polarisations of the four hydrogen hyperfine states plotted as functions of the external magnetic field. The field values are normalised to the critical field B_C.

2.2 Hyperfine Transitions

Let us consider once more the Hamilton operator (2.2) applying the Schrödinger equation to its wavefunction in the original basis, Ψ:

$$i\hbar \frac{\partial \Psi}{\partial t} = \mathcal{H}\Psi \tag{2.23}$$

We wish to transform the original set of functions using the transformation

$$\chi = U_0 \Psi \tag{2.24}$$

which is equivalent to

$$\Psi = U_0^T \chi \tag{2.25}$$

Inserting this into the Schrödinger equation (eq. 2.23) gives

$$\mathcal{H}(U_0^T\chi) = i\hbar\frac{\partial}{\partial t}(U_0^T\chi) \tag{2.26}$$

which can be expanded and rearranged, remembering that U_0^T and χ may both be time dependent, giving:

$$i\hbar U_0^T\frac{\partial\chi}{\partial t} = \mathcal{H}(U_0^T\chi) - i\hbar\frac{\partial U_0^T}{\partial t}\chi \tag{2.27}$$

Multiplying both sides of this equation with U_0, and remembering that $U_0U_0^T = 1$, we get

$$i\hbar\frac{\partial\chi}{\partial t} = U_0\mathcal{H}(U_0^T\chi) - i\hbar\frac{\partial U_0^T}{\partial t}U_0\chi \tag{2.28}$$

$$i\hbar\frac{\partial\chi}{\partial t} = \left(\mathcal{H}_1^{\mathrm{st}} - i\hbar\frac{\partial U_0^T}{\partial t}U_0\right)\chi \tag{2.29}$$

The term $i\hbar\frac{\partial U_0^T}{\partial t}U_0$ is non-zero if the external magnetic field is time dependent. In such a case, the resulting distortion of the eigenstates may originate transitions between pairs of hyperfine states.
Each transition is characterised by a defined angular frequency ω_{ab} related to the energy difference between the two hyperfine states:

$$\omega_{ab} = \frac{|E_a - E_b|}{\hbar} \tag{2.30}$$

The holding field dependence of the energy levels (see eq. 2.17) is of course transferred to the transition frequencies.
Hyperfine transitions can be classified depending on the relative orientations of the static holding field $\mathbf{B}^{\mathrm{st}}$ and the time dependent one $\mathbf{B}(t)$. Transitions caused by the component of $\mathbf{B}(t)$ parallel to the static one, which fulfil the selection rule $\Delta m_F = 0$ are called σ transitions, whereas transitions generated by the perpendicular component of $\mathbf{B}(t)$ and fulfilling the selection rule $\Delta m_F = \pm 1$ are known as π transitions.

2.2.1 σ Transitions

Let us consider an external magnetic field having the following form:

$$\mathbf{B} = (0, 0, B^{\mathrm{st}} + B(t)) \tag{2.31}$$

so that the static component of the field B^{st} and the time dependent one $B(t)$ are parallel. The time dependent part of the hydrogen Hamiltonian contained in (2.29) becomes

$$\mathcal{H}_1^\sigma = i\hbar\begin{pmatrix} 0 & 0 & 0 & 0 \\ 0 & s\dot{s}+c\dot{c} & 0 & -s\dot{c}+c\dot{s} \\ 0 & 0 & 0 & 0 \\ 0 & s\dot{c}-c\dot{s} & 0 & s\dot{s}+c\dot{c} \end{pmatrix} \tag{2.32}$$

$$= i\hbar\begin{pmatrix} 0 & 0 & 0 & 0 \\ 0 & 0 & 0 & -\dot{\theta} \\ 0 & 0 & 0 & 0 \\ 0 & \dot{\theta} & 0 & 0 \end{pmatrix} \tag{2.33}$$

$$= \frac{i\hbar}{2}\dot{x}\begin{pmatrix} 0 & 0 & 0 & 0 \\ 0 & 0 & 0 & \sin^2 2\theta \\ 0 & 0 & 0 & 0 \\ 0 & -\sin^2 2\theta & 0 & 0 \end{pmatrix} \tag{2.34}$$

where $c = \cos\theta$, $s = \sin\theta$, the dot over a variable indicates that it is to be differentiated with respect to time, and the constant $\varepsilon \ll 1$ has been neglected.
Hence, the superposition of a time dependent magnetic field parallel to the holding field results in the connection of hyperfine states $|\,2\,\rangle$ and $|\,4\,\rangle$ of hydrogen. This leads to the possible transition

$$\sigma\,|\,2\,\rangle \leftrightarrow |\,4\,\rangle \qquad\qquad (\Delta F = \pm 1, \Delta m_F = 0)$$

2.2.2 π Transitions

Let us choose now the time-dependent component of the field to be perpendicular to the holding field so that $B(t)$ is either directed along x or along y. In order to describe this scenario, one has to rewrite the matrix form of the Hamilton operator (2.10) in the following way:

$$\mathcal{H}_0 = \mathcal{H}_0^{\mathrm{st}} + \mathcal{H}_0^{\pi} \tag{2.35}$$

where $\mathcal{H}_0^{\mathrm{st}}$ designates the static part of the Hamiltonian and the index 0 denotes the representation given by the basis (2.3). If the time-dependent field lies along the x axis, so that

$$\mathbf{B} = (B(t), 0, B_z^{\mathrm{st}}) \tag{2.36}$$

then the part of the Hamiltonian responsible for the disturbance is

$$\mathcal{H}_0^{\pi} = \frac{g_s \mu_B}{\hbar} B(t) \sigma_x \tag{2.37}$$

where σ_x is the Pauli spin matrix. In the basis $|\,m_S, m_I\,\rangle$ the matrices σ_x and σ_y are

$$\sigma_x = \tfrac{\hbar}{2}\begin{pmatrix} 0 & 0 & 0 & 1 \\ 0 & 0 & 1 & 0 \\ 0 & 1 & 0 & 0 \\ 1 & 0 & 0 & 0 \end{pmatrix} \qquad \sigma_y = \tfrac{\hbar}{2}\begin{pmatrix} 0 & 0 & 0 & -i \\ 0 & 0 & -i & 0 \\ 0 & i & 0 & 0 \\ i & 0 & 0 & 0 \end{pmatrix}. \tag{2.38}$$

We can see that the result for a time-dependent field in the y direction will differ only by a factor of i. Proceeding with the field only in the x direction, we find

$$\mathcal{H}_0^{\pi} = \frac{g_s \mu_B}{2} B(t) \begin{pmatrix} 0 & 0 & 0 & 1 \\ 0 & 0 & 1 & 0 \\ 0 & 1 & 0 & 0 \\ 1 & 0 & 0 & 0 \end{pmatrix} \tag{2.39}$$

Applying the orthogonal transformation (2.13) to $\mathcal{H}_0^{\pi}$ gives

$$\mathcal{H}_1^{\pi} = U_0 \mathcal{H}_0^{\pi} U_0^T \tag{2.40}$$

neglecting the constant $\varepsilon \ll 1$, we get

$$\mathcal{H}_1^{\pi} = \frac{g_s \mu_B}{2} B(t) \begin{pmatrix} 0 & \sin\theta & 0 & \cos\theta \\ \sin\theta & 0 & \cos\theta & 0 \\ 0 & \cos\theta & 0 & -\sin\theta \\ \cos\theta & 0 & -\sin\theta & 0 \end{pmatrix} \tag{2.41}$$

Thus, from the (2.41) one can conclude that the presence of a time dependent field perpendicular to the static one connects the four pairs of hyperfine states, leading to the following possible transitions:

$$\begin{array}{ll} \pi \,|\,1\,\rangle \leftrightarrow |\,2\,\rangle & (\Delta F = 0, \Delta m_F = \pm 1) \\ \pi \,|\,2\,\rangle \leftrightarrow |\,3\,\rangle & (\Delta F = 0, \Delta m_F = \pm 1) \\ \pi \,|\,1\,\rangle \leftrightarrow |\,4\,\rangle & (\Delta F = \pm 1, \Delta m_F = \pm 1) \\ \pi \,|\,3\,\rangle \leftrightarrow |\,4\,\rangle & (\Delta F = \pm 1, \Delta m_F = \pm 1) \end{array}$$

In figure 2.3 the resonance frequencies of all hydrogen transitions are plotted as function of the holding field.

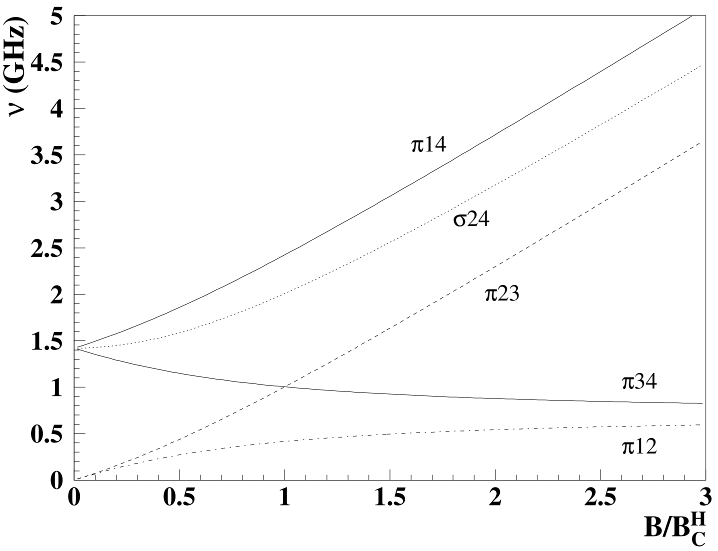

Figure 2.3:
Frequencies of hydrogen hyperfine transitions plotted as functions of the holding field. The field values are normalised to the critical field B_C.

2.2.3 Transition Probability

If a system which is in a stationary state experiences a perturbation, then the transition probability, as given by first-order time-dependent perturbation theory is

$$P(t) = |c(\tau)|^2 \tag{2.42}$$

where the coefficient $c(\tau)$ is given by the integral

$$c(\tau) = \frac{1}{i\hbar} \int_0^{\tau} \exp\left(i\omega_{ab}t\right) H_{ab}(t)dt \tag{2.43}$$

where $t = 0$ is the time when the perturbation starts. Before this time, the system is certain to be in state $|\,a\,\rangle$. As our perturbation will be sinusoidal, we can proceed by separating H_{ab} into a constant and time-dependent part, so

$$H_{ab}(t) = H_{ab}\cos(\omega t) \tag{2.44}$$

and

$$c(\tau) = \frac{H_{ab}}{i\hbar} \int_0^{\tau} \exp\left(i\omega_{ab}t\right) \cos(\omega t)dt. \tag{2.45}$$

For a fixed interaction time τ, the transition probability between states $|\,a\,\rangle$ and $|\,b\,\rangle$ for an atom is given at the first perturbative order by [Coh99]:

$$P_{ab} = \frac{|H_{ab}|^2}{4\hbar^2} F(\tau, \omega - \omega_{ab}) \tag{2.46}$$

where the function F is defined as

$$F(\tau, \omega - \omega_{ab}) = \left(\frac{\sin\left[(\omega - \omega_{ab})\,\tau/2\right]}{(\omega - \omega_{ab})/2} \right)^2 \tag{2.47}$$

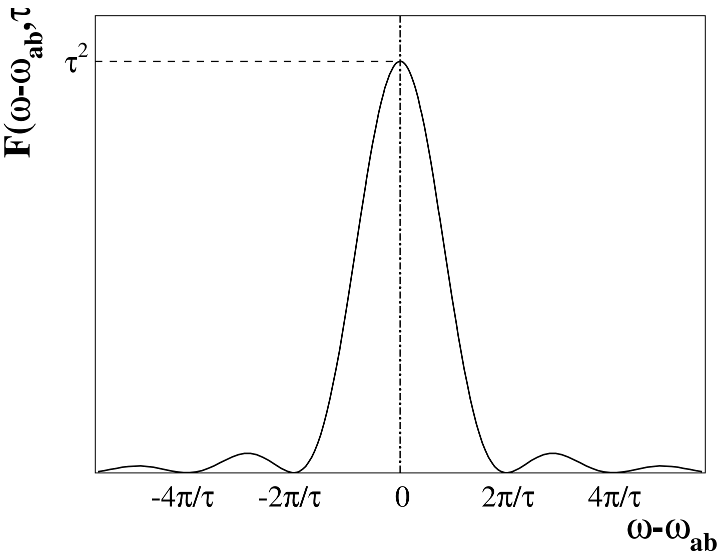

Figure 2.4:
The function $F(\omega-\omega_{ab},\tau)$ at fixed τ. The expression $\omega-\omega_{ab}=\frac{2\pi}{\tau}n$ $(n=\pm1,\pm2,...)$ defines the zeros of the function. At the resonant condition $\omega=\omega_{ab}$, $f(\omega-\omega_{ab},\tau)=\tau^2$.

Figure 2.4 shows the behaviour of (2.47) for a fixed time τ. The function is basically zero outside the range $|\omega-\omega_{ab}|\leq\frac{2\pi}{\tau}$, whereas it reaches its maximum value τ^2 at the *resonance condition*

$$\lim_{\omega\to\omega_{ab}} F(\omega-\omega_{ab},\tau)=\tau^2 \tag{2.48}$$

If (2.48) holds, the transition probability from eq. 2.46

$$P_{ab}=\frac{|H_{ab}|^2}{4\hbar^2}\tau^2 \tag{2.49}$$

In order to complete the picture of transition probabilities, we must first take the general equation for a σ transition (2.34) and insert the sinusoidal field as defined in 2.44. The resulting elements will be

$$H_{42}=-H_{24}=\frac{-i\hbar\omega_{24}}{2}\frac{B_{\|}}{B_c}\sin^2(2\theta) \tag{2.50}$$

where ω_{24} has entered the equation through differentiation of the field w.r.t time. It can be shown, using the energy levels in equation 2.17 and the mixing angle relations in equation 2.15, that the relation between the transition energy $\hbar\omega_{24}$ and the hyperfine splitting energy, E_{HFS}, is given by

$$\hbar\omega_{24}=\frac{E_{\mathrm{HFS}}}{\sin(2\theta)} \tag{2.51}$$

Remembering that $g_s\mu_B=E_{\mathrm{HFS}}/B_c$, and approximating g_s with 2, we get a matrix containing the complete set of probabilities for hyperfine transitions.

$$P=\frac{\mu_B^2\tau^2B_{\perp,\|}^2}{4\hbar^2}\begin{pmatrix} 0 & \sin^2\theta & 0 & \cos^2\theta \\ \sin^2\theta & 0 & \cos^2\theta & \sin^2 2\theta \\ 0 & \cos^2\theta & 0 & \sin^2\theta \\ \cos^2\theta & \sin^2 2\theta & \sin^2\theta & 0 \end{pmatrix} \tag{2.52}$$

where $b_\perp$ or $b_\|$ is the amplitude of the high-frequency field, so

$$B(t)=B_{\perp,\|}\cos\omega t \tag{2.53}$$

The probability is proportional to the square of the disturbing field, and to the square of the time for which the resonance condition is held. Of course the conditions regarding field orientation still apply. The holding field dependence of the transition probability is given by the matrix elements, which are plotted in figure 2.5.

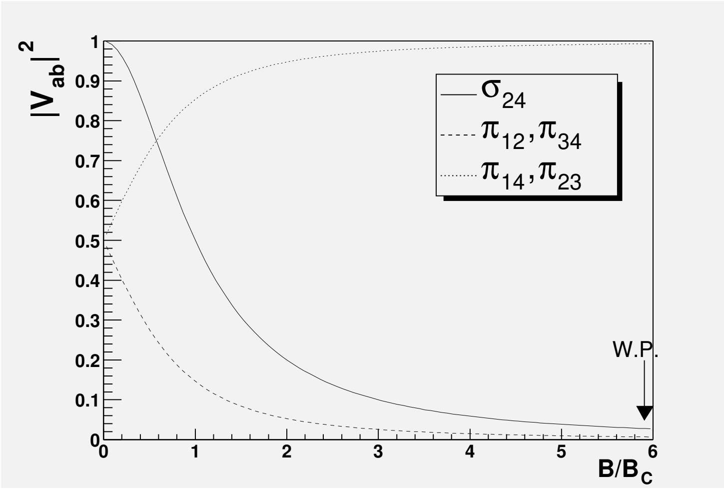

Figure 2.5: The probability matrix elements V_{ab}, as a function of holding field. Note that the σ transitions and those π transitions where the nuclear spin is flipped are suppressed for high holding field values. The working point of the transverse target is marked (WP).

2.3 Depolarising Resonances from the Hera Beam

The current carried by the electron bunches in the HERA beam produces transient magnetic fields, which can cause hyperfine transitions. In order to calculate the frequencies of harmonics of the HERA electron beam, it is necessary to perform a Fourier analysis on the beam structure, so that the transient fields can be represented as a sum of sinusoidal fields. We can then use the results which we just found in order to calculate a probability of the transition occurring.

In the simplest model, the HERA beam is assumed to consist of 220 equally spaced Gaussian bunches, each carrying the same current. This means that the bunch structure repeats after a time interval, T, corresponding to the time between successive bunches (see figure 2.6). For HERA, $T = T_{\text{bunch}} \simeq 96\,\text{ns}$. The 1 σ length of the bunches is around 30 ps, which is 0.03% of the time between two bunches, or around one part in 3000. This is a rather good approximation of a delta function, so we can expect rather a lot of harmonics as we express this structure using a Fourier expansion.

Any physical beam structure, $I(t)$, can be represented as an infinite sum of sine and cosine terms:

$$I(t) = \frac{a_0}{2} + \sum_{k=1}^{\infty}\left(a_k \cos\left(\frac{2\pi kt}{T}\right) + b_k \sin\left(\frac{2\pi kt}{T}\right)\right) \tag{2.54}$$

where the coefficients a_0, a_k and b_k can be found as following.

$$\begin{aligned}
a_0 &= \frac{2}{T}\int_{-\frac{T}{2}}^{\frac{T}{2}} I(t)\; dt \\
a_k &= \frac{2}{T}\int_{-\frac{T}{2}}^{\frac{T}{2}} I(t)\cos\left(\frac{2\pi kt}{T}\right)\; dt \\
b_k &= \frac{2}{T}\int_{-\frac{T}{2}}^{\frac{T}{2}} I(t)\sin\left(\frac{2\pi kt}{T}\right)\; dt
\end{aligned} \tag{2.55}$$

For a Gaussian bunch structure it helps to use a complex notation for the Fourier coeffi-

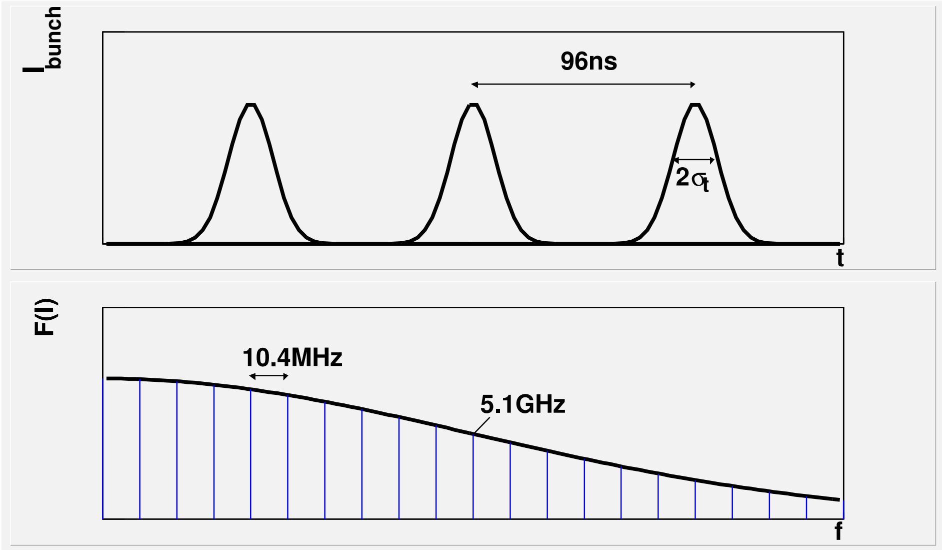

Figure 2.6: Current structure and Fourier harmonics for a repeated Gaussian bunch. The bunch length is described by the 1 σ value of 31 ps. Harmonics are spaced by $f_{\mathrm{bunch}} = \frac{1}{T}$ and the envelope of the harmonics has a width of 5.1 GHz, corresponding to the bunch length.

cients

$$a_k + ib_k = \frac{2}{T} \int_{-\frac{T}{2}}^{\frac{T}{2}} I(t) \exp\left(\frac{2\pi ikt}{T}\right) dt \tag{2.56}$$

The bunch current is described by the function

$$I(t) = I_0 \exp(-\alpha t^2), \tag{2.57}$$

and inserting this into equation 2.56, this gives

$$a_k + ib_k = \frac{2I_0}{T} \int_{-\frac{T}{2}}^{\frac{T}{2}} \exp(-\alpha t^2) \exp\left(\frac{2\pi ikt}{T}\right) dt. \tag{2.58}$$

Assuming that the bunch width is small compared to the time between bunches, the upper and lower integral limits can be changed to $-\infty$ and ∞ respectively, and the integral then becomes a standard integral, leading to the solution

$$a_k + ib_k = \frac{2I_0}{T} \sqrt{\frac{\pi}{\alpha}} \exp\left(\frac{-\pi^2 k^2}{T^2 \alpha}\right), \tag{2.59}$$

which gives the amplitudes of the series of harmonics based on the fundamental frequency, f_{bunch}, given by $\frac{1}{T}$, which is equal to $\simeq 10.4097$ MHz. This result is shown graphically in figure 2.6. It is helpful to express α in terms of the standard deviation of the bunch current, so that

$$\alpha = \frac{1}{2\sigma_t^2} \tag{2.60}$$

By replacing k in equation 2.59 with fT, where f represents the frequency of the harmonic, this equation can be written

$$a_k + ib_k = \frac{2I_0}{T} \sqrt{\frac{\pi}{\alpha}} \exp\left(-\frac{f^2}{2\sigma_f^2}\right), \tag{2.61}$$

with

$$\sigma_f = \frac{1}{2\pi\sigma_t} \tag{2.62}$$

which for a typical 1 σ bunch length of 9.3 mm corresponds to a frequency of 5.1 GHz, or a harmonic number of $k \simeq 500$. Thus if the resonant frequency for a transition, as defined by equation 2.30, matches a multiple of f_{bunch}, then it is possible that the hyperfine state of an atom will be changed.

2.3.1 Position and Spacing of Beam Induced Resonances

The values of the target holding field for which resonances occur can be found using the energy levels from equation 2.17 together with the requirement that $\Delta E = k \cdot h \cdot f_{\text{bunch}}$. The results are shown in figure 2.7 and in table 2.1.

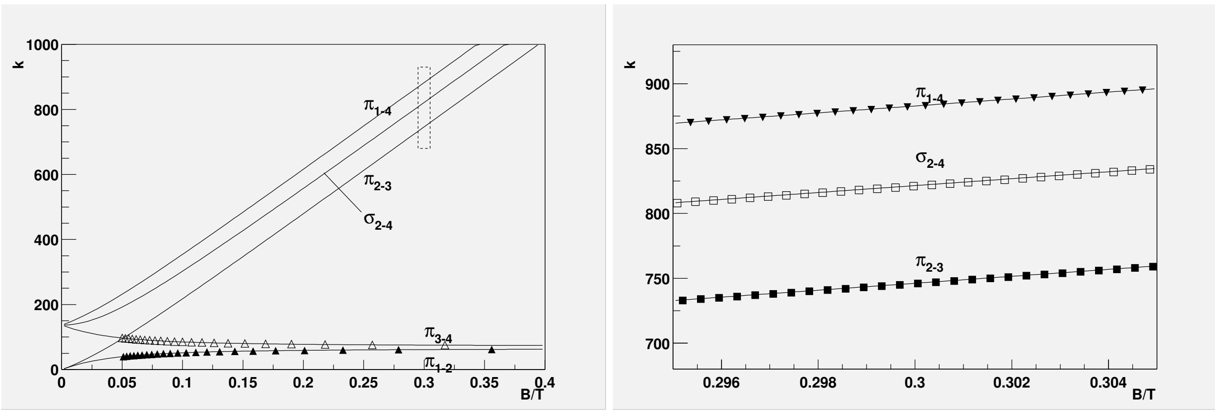

Figure 2.7: Left: the magnetic fields at which resonances can occur are marked. For fields where $\frac{dE}{dB}$ is large, such as in the box, the resonances can only be seen by zooming in (right picture).

It is evident that the larger the gradient, $\frac{dE}{dB}$ is, the narrower the spacing of the resonances becomes. If we take the energy level differences from equation 2.17, ignoring the nuclear contribution, and differentiate with respect to x, then we get the following relations:

$$\begin{aligned}
\frac{d(E_1-E_2)}{dx} = \frac{d(E_4-E_3)}{dx} &= \frac{E_{\text{HFS}}}{2}\left(1-\frac{x}{\sqrt{x^2-1}}\right)\\
\frac{d(E_1-E_4)}{dx} = \frac{d(E_2-E_3)}{dx} &= \frac{E_{\text{HFS}}}{2}\left(1+\frac{x}{\sqrt{x^2+1}}\right)\\
\frac{d(E_2-E_4)}{dx} &= E_{\text{HFS}}\frac{x}{\sqrt{x^2+1}}
\end{aligned} \tag{2.63}$$

Using the identities from equation 2.15 then the results are

$$\begin{aligned}
\pi_{12}, \pi_{34}: \qquad & \Delta B = \frac{B_c}{\nu_{\text{HFS}}}\frac{1}{\sin^2\theta}\Delta\nu\\
\pi_{23}, \pi_{14}: \qquad & \Delta B = \frac{B_c}{\nu_{\text{HFS}}}\frac{1}{\cos^2\theta}\Delta\nu\\
\sigma_{24}: \qquad & \Delta B = \frac{B_c}{\nu_{\text{HFS}}}\frac{1}{\cos 2\theta}\Delta\nu
\end{aligned} \tag{2.64}$$

Setting $\Delta\nu$ to be $f_{\text{bunch}} = 10.4097$ MHz, we find that $\frac{B_c \Delta\nu}{\nu_{\text{HFS}}} = 0.37$ mT. In the low field limit, where $\theta = \frac{\pi}{4}$, the spacing will be 0.74 mT for π transitions, and will approach infinity for σ transitions. In the high field limit the spacing of the nuclear π transitions approaches infinity, and that for the electron π and σ transitions 0.37 mT.

Holding Field/mT	Resonance	k
202.5	π_{12}	59
215.7	π_{34}	77
235.0	π_{12}	60
253.7	π_{34}	76
282.1	π_{12}	61
311.8	π_{34}	75
362.3	π_{12}	62

Table 2.1: The position of the nuclear π resonances between 200 and 400mT. A holding field for the transverse target of 297mT, which is at the mid-point between the 61_{st} π_{12} resonance and the 76_{th} π_{34} resonance was chosen. These values are calculated using a bunch frequency, f_{bunch}, of 10.4097 MHz.

Chapter 3

The Hermes Target

A "Fixed Target" is one that is stationary, and not necessarily one which has been repaired.

Peter H. Garbincius (paraphrased)

Polarised gas targets have a long and distinguished history, as detailed in [SH03] and [Hae67]. The HERMES target holds the record for all time production of polarised Hydrogen and Deuterium atoms, as a result of optimisation studies during the design process and of its longevity: the ABS has been running more or less continuously since 1996. Although higher intensity sources have since been built, the HERMES target will remain the prime example of use of a polarised internal target at a storage ring for years to come, especially in terms of reliability and suppression of systematic errors.

The HERMES target [Her05] is shown schematically in figure 3.1. Nuclear polarised atoms are continuously injected from the Polarised Atomic Beam Source (ABS) into the elliptical target cell. Most atoms leave the cell through either of the open ends of the cell, whilst a small sample exit through the sample tube and can be analysed by either the Target Gas Analyser (TGA), which measures the ratio of atoms to molecules, or the Breit-Rabi Polarimeter (BRP), which measures the atomic polarisation. Electrons from the HERA storage ring can scatter from the atoms in the target cell. The cell is surrounded by a magnet (not shown), whose field defines the polarisation axis of the atoms and inhibits depolarisation during the atom's presence in the cell. In order to prevent a direct passage from ABS to BRP, both are tilted by 30° to the horizontal.

3.1 The Polarised Atomic Beam Source (ABS)

The ABS [Nas02] works on the principle of Stern-Gerlach separation together with High Frequency Transitions (HFTs) in order to inject nuclear polarised atoms into the target cell. Hydrogen gas is dissociated in a 13.56 MHz water-cooled RF plasma, and then enters the differential high-vacuum pumping system of the ABS through a cooled nozzle (typically at 100 K). Two diaphragms, known as the skimmer and collimator, create an atomic beam with narrow divergence. The beam then passes through the sextupole magnets, which focus atoms with electron spin, $m_S = +\frac{1}{2}$ and defocus atoms with $m_S = -\frac{1}{2}$. The ABS appendix, labelled as chamber IVa in figure 3.2, contains two HFTs, which can be used to transform the electron-polarised beam into a nuclear-polarised beam. The ABS is capable of an injection rate of $6.6 \cdot 10^{16}$ atoms/s, with an injected nuclear polarisation of 98% for a holding field in the strong field limit ($\lim_{\theta \to 0}$).

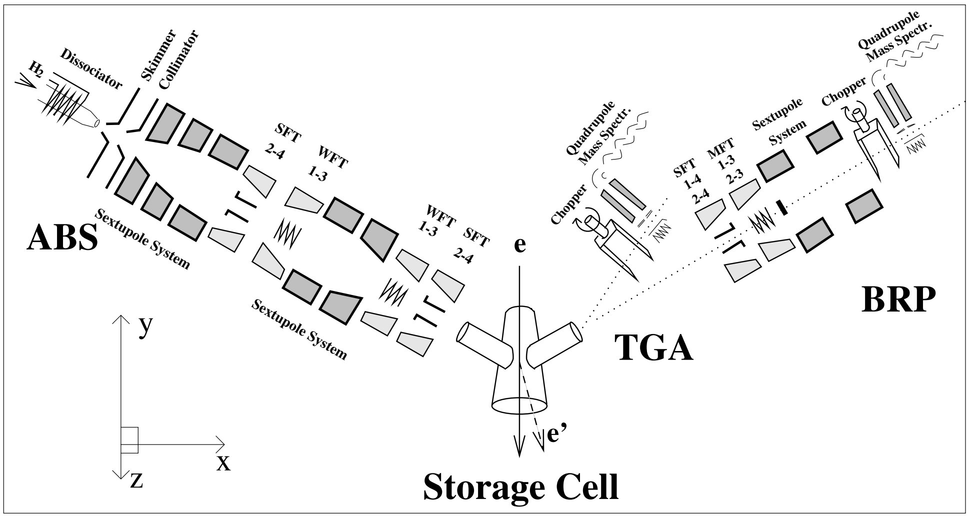

Figure 3.1: The HERMES target, with its components listed. The HERMES coordinates system is also shown.

3.1.1 The Radio Frequency Dissociator (RFD)

Hydrogen gas is supplied to the dissociator at a typical flow-rate of 1.5 mbar·l/s. Dissociation is achieved by electron impact in a cold plasma, induced by an LC circuit driven by a 13.56 MHz RF generator with an applied power of 300 W. The impedance of the circuit can be matched by means of a tuning circuit with two variable capacitors.

The Plasma occurs inside a discharge tube, made from either Pyrex or Quartz glass. The outer surface of the discharge tube is cooled by a flow of 18°C water, which is contained within a glass tube concentric to the discharge tube. In order to increase the degree of dissociation, a small amount of oxygen (typically 0.1% by volume) is added to the hydrogen gas entering the dissociator. Test studies have shown that a degree of dissociation, defined by

$$\alpha = \frac{I_a}{I_a + 2I_m} \tag{3.1}$$

of around 80% [Koc99] is reached under these conditions. The dissociated gas can then exit the discharge tube through an aluminium nozzle kept at 100 K using a 120 W closed-cycle Helium cold head. The exact nozzle temperature is controlled by an additional heater current.

Water molecules are a by-product of the Plasma, and therefore over time a layer of ice develops on the cold nozzle. This has the positive effect of decreasing the probability of hydrogen atoms recombining on the nozzle, for the recombination probability is lower on ice than on aluminium. However, if the ice layer becomes too thick, the aperture through which atoms can pass through the nozzle is reduced, and the pressure in the discharge tube (typically around 1mbar) builds up, leading to increased volume recombination. At this point (typically after 4-5 days continuous operation), it is necessary to warm the nozzle in order to remove the ice layer. The speed of ice formation depends on the rate at which oxygen is admitted, thus it is of importance to keep the oxygen flow as low as possible.

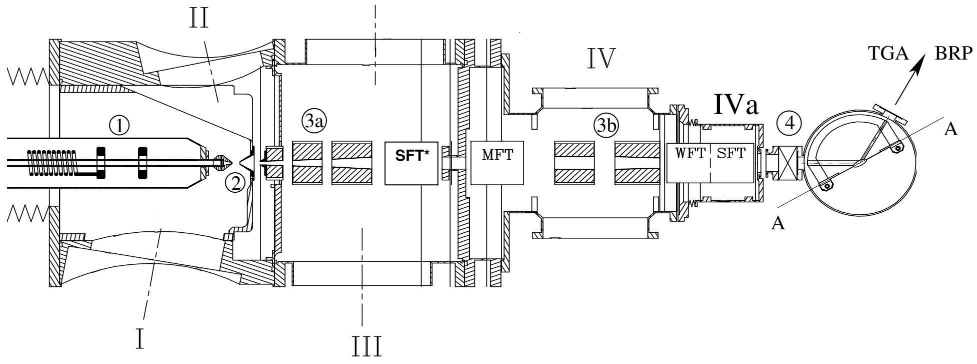

Figure 3.2: The components of the ABS are shown. The four vacuum chambers (labelled I to IV/IVa) are shown, together with the RF dissociator (1), the beam forming system (2), the sextupole magnets (3a and 3b) and the HFTs. The valve separating the ABS from the HERA vacuum is shown (4), as is the horizontal plane (A-A).

3.1.2 The Sextupole Magnets

After exiting the nozzle and passing through the skimmer and collimator, the atomic beam enters the sextupole magnet system, which deflects the hyperfine states $|\,3\,\rangle$ and $|\,4\,\rangle$ from the beam. These are high grade permanent magnets, consisting of 24 segments made of Vacodym[1], with a maximum pole-tip field of 1.5 T. To prevent chemical destruction by hydrogen, the magnets are enclosed in vacuum-tight stainless steel cans. In order to restrict a pressure increase inside the magnets from deflected atoms, the set of magnets in the first sextupole chamber is split into three sections. Additionally the magnets are tapered, to allow a maximum acceptance angle and to enable achromatic focusing. A second set of magnets in the second sextupole chamber focuses the atomic beam, which ideally only consists of atoms in states $|\,1\,\rangle$ and $|\,2\,\rangle$ into the injection tube. As the field gradient on the beam axis is zero, a small fraction of atoms with $m_S = -\frac{1}{2}$ pass through the sextupole system. This effect is very small, however, (less than 0.1% [Nas02]) and after passing through the sextupole system, the beam has roughly half the intensity and is strongly electron polarised.

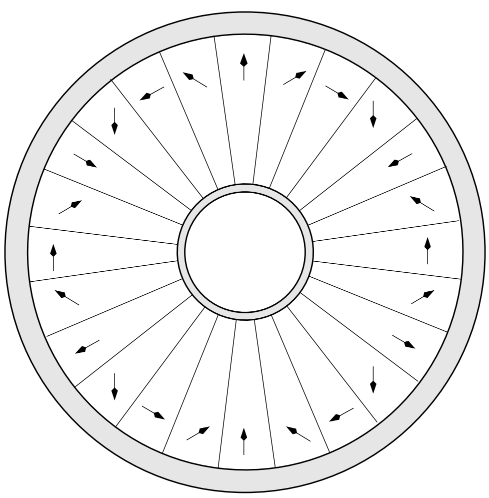

Figure 3.3: A cross section of a sextupole magnet

[1] Trademark of Vacuumschmelze GmbH

3.1.3 High Frequency Transitions

Adiabatic High Frequency Transition units are used to convert the electron polarisation into nuclear polarisation. These units all require a high frequency field to supply photons to enable the transition, and a holding field which defines the exact energy difference between the two hyperfine states. These two fields must be correctly aligned (parallel for a σ transition, perpendicular for a π). For transitions within the $F = 1$ triplet, the high frequency field is 10-70 MHz, which can be supplied by a simple solenoid coil. These are also known as Weak Field Transitions (WFTs) or Medium Field Transitions (MFTs). Transitions between the $F = 1$ triplet and the $F = 0$ singlet must overcome the hyperfine splitting energy (E_{HFS}), and in this case a strip-line cavity is needed to provide the 1430 MHz HF field, and the transition is known an a Strong Field Transition (SFT). In order to achieve a transition efficiency of close to 100%, the holding field consists of a homogeneous field, superimposed by a gradient field, with a resulting field which increases (or decreases) along the beam path.

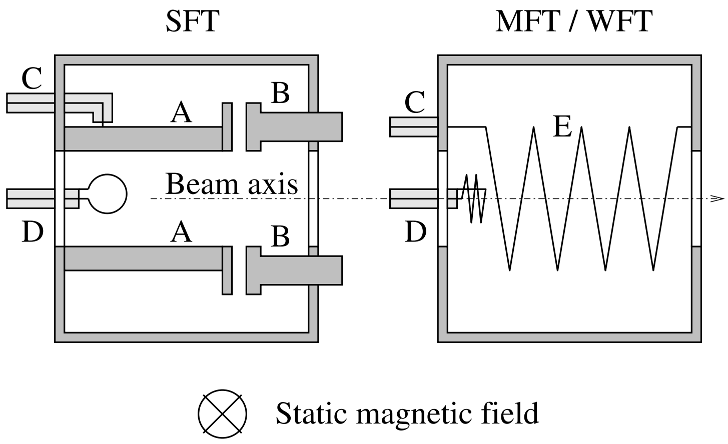

Figure 3.4: A schematic view of the SFT resonator and the MFT/WFT coil system. The components shown are the resonator rods (A), the adjustable capacitor which controls the resonant frequency of the cavity (B), the RF power input (C), the pick-up loop (D) and the RF coil (E).

The SFTs are particularly sensitive to temperature changes, as the resonant frequency of the cavity depends on the capacitative load, as shown in figure 3.4. In order to keep these effects low, the ABS SFTs are air-cooled. The SFTs can be kept in frequency using a feedback loop, as described in [Bra95], and the gradient field ensures that the resonance is wide enough to take account of a small frequency drift.

The ABS contains four HFTs. Two of these, as already stated, are located in the ABS Appendix, whilst the other two are located between the two sets of sextupole magnets. If a transition occurs here, then the atoms affected will not be able to pass the second set of sextupole magnets, and only one of the original four states can proceed to the target cell. The complete set of possible injection modes of the ABS is presented in table 3.1. Because of spacial constraints, the two transitions in the ABS appendix cannot work concurrently, and it is not possible to inject two states with negative electron polarisation. .

3.2 Microwave Dissociator Development

An alternative dissociator, known as the Microwave Dissociator (MWD) [Koc99b, Boe97], based on a plasma source which couples a 2.45 GHz surface wave to the discharge in air-cooled Pyrex glass has been developed. Tests showed that this dissociator provided a higher degree of dissociation compared to the RFD, particularly for higher hydrogen flow rates. This would potentially enable a higher output intensity of the ABS. The Magnetron for the plasma source can achieve a power of 1200 W.

HFT (betw. 6-poles)	HFT (appendix)	Inj. States	P_e	P_z	Use
-	-	$\|1\rangle, \|2\rangle$	+1	0	Cal
-	WFT 1-3	$\|2\rangle, \|3\rangle$	0	-1	Data
-	SFT 2-4	$\|1\rangle, \|4\rangle$	0	+1	Data
SFT 2-4	-	$\|1\rangle$	+1	+1	Cal
WFT 1-3	-	$\|2\rangle$	+1	-1	Cal
SFT 2-4	WFT 1-3	$\|3\rangle$	-1	-1	Cal
WFT 1-3	SFT 2-4	$\|4\rangle$	-1	+1	Cal
WFT 1-3, SFT 2-4	-	none	-	-	Cal

Table 3.1: The possible injection modes of the ABS. Only two modes are used for polarised HERMES data collection. The others are for target calibrations only. The polarisations shown are for the ideal cases of sextupole and HFT efficiencies.

The air-cooling of the MWD is achieved using a rotary pump with nominal pumping speed of 140 m^3/h that sucks air through the region outside the glass discharge tube. This cooling was found, however, not to be as effective as the water-cooling of the RFD, and the amount of oxygen which must be added is 2-3 times higher. This added oxygen content means that the nozzle of the ABS must be regenerated much more often. Although the dissociator has been designed to allow a regeneration to occur inside the time needed for protons and electrons to be injected into the HERA ring (under three hours), the resulting regeneration time for the air-cooled MWD of roughly two days is too short, bearing in mind that the time between fills is also needed for target calibrations and studies. Each regeneration also places a mechanical stress on the glass tube.

A liquid-cooled MWD could provide the higher intensities reported for the air-cooled MWD, but without the disadvantage of shorter regeneration times. The specifications of such a liquid, are:

- No appreciable absorption of 2.45 GHz radiation.
- Compatability with the ABS vacuum pumps and gauges, in case of a glass tube breaking.
- Compatability with the HERMES safety regulations.

The obvious cooling candidate, water, fails the first requirement, and tests [Nas01] showed that a silicon based cooling agent (Syltherm XLT)[2] caused long term contamination of the vacuum chamber in the event of the discharge tube breaking. It was therefore suggested that alcohol, cooled by a Lauda T4600[3] , despite its flammability, was the best option for the cooling agent. Tests made with this agent will be described in the following section.

3.2.1 The MWD Test Bench

The test bench enables preliminary testing of the dissociator. Dissociated atoms can recombine in a copper recombination block, and the degree of dissociation found by observing the temperature of the block, which is heated due to the exothermic nature of

[2]Syltherm XLT is a trademark of the Dow Corning Corporation
[3]Product of Lauda Dr. R. Wobser GmbH & Co. KG

hydrogen recombination. The pressure in the discharge tube is controlled by a throttle valve, which takes the place of the nozzle aperture in a real ABS. The recombination block

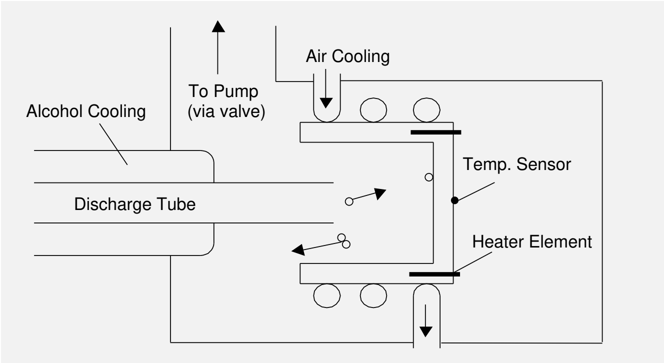

Figure 3.5: A schematic diagram of the recombination block calorimeter. Atoms from the discharge tube recombine on the wall of the copper block, depositing energy to the block.

must be calibrated in order to find a degree of dissociation in the discharge tube. A cooling flow of air, controlled by a needle valve, is supplied to the recombination block in order to ensure that thermal equilibrium is quickly reached. A temperature-power calibration curve can be found by means of a heater cartridge, implanted in the block. It is assumed that all atoms recombine on the surface of the block, and that the energy deposited by the atoms to reach a certain stable temperature is equivalent to the electrical energy from the heater cartridge needed to reach the same temperature. Given the temperature-power

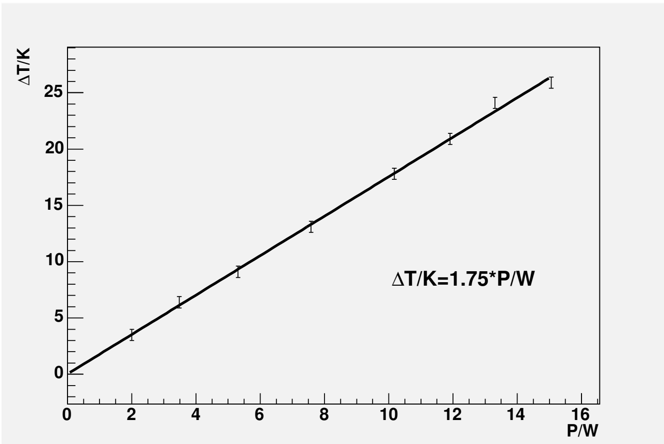

Figure 3.6: Temperature-power calibration curve of the recombination block calorimeter.

calibration, together with the information that the recombination energy of hydrogen is 435.99 KJ/mol, it is possible to calculate the number of molecules reformed per second, N_{ref}. The number of hydrogen molecules entering the discharge per second, N_{flow} is measured by the flow-meter, situated before the discharge tube. Assuming that there is no leak in or out of the system, the degree of dissociation is then given by

$$\alpha = N_{\mathrm{ref}}/N_{\mathrm{flow}}. \tag{3.2}$$

Another useful indicator of the degree of dissociation is the length of the plasma. As the plasma emits visible radiation (roughly magenta in colour), the length can easily be observed. Both α and the plasma length are shown in figure 3.7. At very low oxygen flows, the discharge becomes much shorter, and changes colour from the typical magenta to a whitish colour, as observed by Koch. This measurement, made with a hydrogen flow of 90 sccm confirms that the oxygen flow needed is lower than for the air-cooled dissociator. For this measurement, the alcohol was kept at 18° C, and the microwave power at 80% of its maximum value of 1200 W.

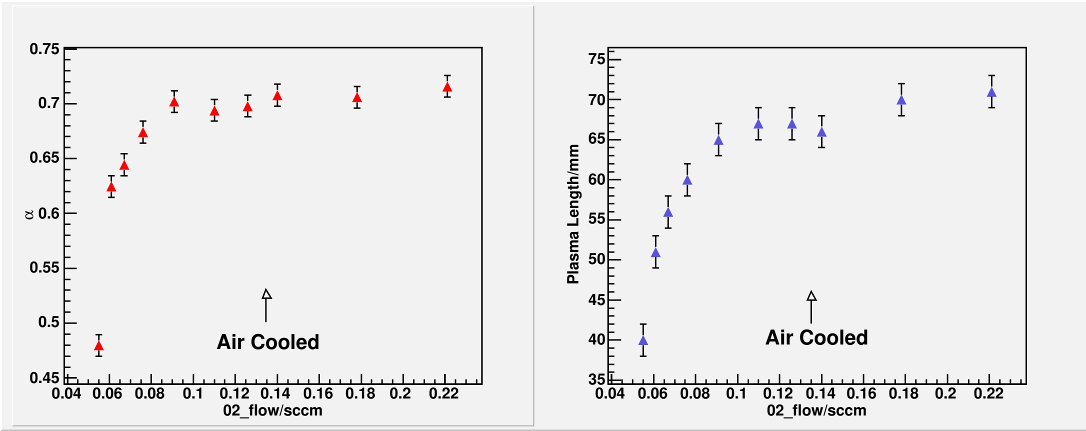

Figure 3.7: Left: Degree of dissociation, α, as a function of oxygen flux. Right: Plasma length as function of oxygen flux. The hydrogen flux was 90 sccm (or 1.5 mbar· l/s).

3.2.2 The ABS Test Stand

In order to test the performance of the ABS dissociator, the ABS test stand was built [Koc99]. The design is similar to that of the HERMES ABS as shown in figure 3.2, but without the sextupole magnets and transition units. A quadrupole mass spectrometer (QMS) situated in chamber IV allows the degree of dissociation of the atomic beam to be found. Further tests on the alcohol-cooled Microwave Dissociator (MWD) were made

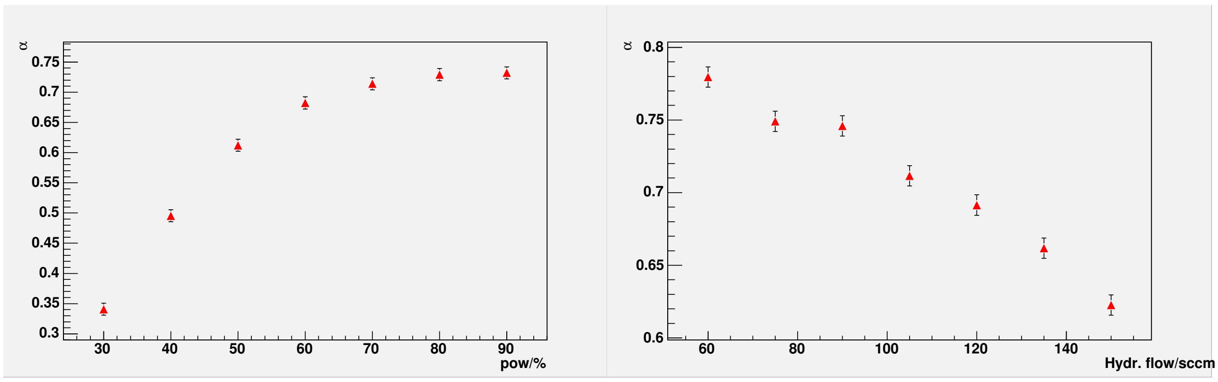

Figure 3.8: Left: α versus microwave power for a flow of 90 sccm and a nozzle temperature of 120K. The power is shown as a percentage of 1200 W. Right: α versus H_2 flow for a nozzle temperature of 120 K and 80% power. For Hydrogen flows above 100 sccm the oxygen flow was increased from 0.1 sccm to 0.2 sccm.

on the ABS test stand. This allowed tests to be made with a cold nozzle, and for the degree of dissociation as found by the recombination calorimeter to be cross-checked with that from the QMS. As it is no longer necessary to wait for thermal equilibrium to be reached between the heating and cooling effects in the calorimeter, the time needed for a measurement is drastically reduced. This enabled the measurements shown in figure 3.8 to be made, which show saturation for high power levels for a 90 sccm flow, and the decrease in α for higher flows.

A further parameter which was tested here was the dependence on the temperature of the cooling fluid. The surface recombination coefficient, γ_{glass}, which is the probability of an atom recombining for a single collision with the glass surface, can be parametrised by an exponential function [Koc99], based on data in [Kim91]

$$\gamma_{\text{glass}} = 8.41 \cdot 10^{-6} \exp\left(4.82 \cdot 10^{-3} \cdot \frac{T_s}{K}\right) . \tag{3.3}$$

Thus it would be expected that reducing the temperature of the cooling agent would lead to an increase in α. This effect is seen in figure 3.9. The lowest temperature in the plot reflects the limit of the cooling power of the Lauda. If lower temperatures were required, it would be recommended to thermally insulate the cooling lines. Of course, condensation builds up on any glass and metal surfaces of the dissociator which are exposed to the atmosphere at cold temperatures, which may be a reason for not operating such a system below 0°C. The improvement in the degree of dissociation achieved by cooling could not be achieved by further increasing the oxygen flux.

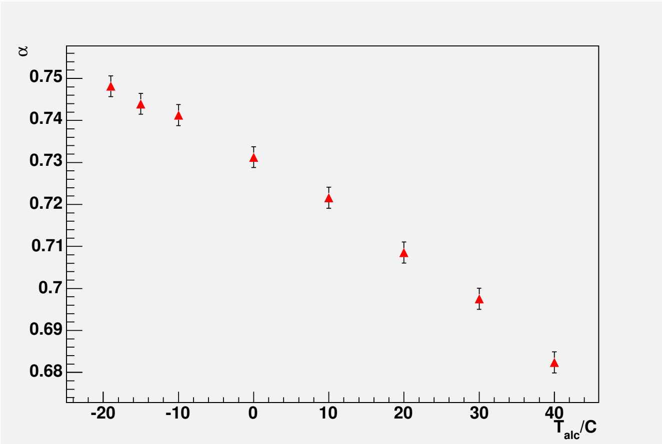

Figure 3.9: α as a function of Alcohol Temperature, taken with a nozzle temperature of 120 K, a hydrogen flow of 90 sccm, an oxygen flow of 0.16 sccm, and a microwave power of 80% of its maximum value of 1200 W. For each point, if necessary, the surfatron was tuned so as to bring the reflected power to zero. This measurement was made on the ABS test stand.

3.2.3 Summary of the Alcohol-Cooling Tests

Koch presented α values of up to 80% for the air-cooled dissociator, the values presented here remained lower. This could be due to a degradation of the surface of the discharge tube: for all measurements shown here were made with a single discharge tube. Although the tubes were prepared as detailed in [Koc99], this seems the most likely explanation.

The alcohol-cooled dissociator allows a reduced oxygen flow compared to the air-cooled version, which would make it more suitable for use in an accelerator such as HERA. The oxygen flux needed is comparable to that required by the RF dissociator, which gives arise to the prospect of a dissociator which combines the advantage of the air-cooled Microwave Dissociator (high atomic flux) with the advantage of the RFD (long regeneration period). This must, however, be offset against the safety considerations of the alcohol cooling circuit.

The water in the cooling circuit for the RFD at HERMES is cooled to 18°C, and figure 3.9 raises the question of whether further cooling of this circuit would bring an increase in α. The answer to this depends on the reasons for recombination on the discharge tube, which depends on the properties of the glass surface. Would a perfectly prepared glass tube, running with α at 80% or above, benefit from liquid cooling below 18°C? Haeberli [Hae67] noted that "the proper treatment of the glass surfaces of the discharge vessel is the subject of much folk lore", whilst thirty years later Koch observed that recombination coefficients for quartz glass presented in literature "vary strongly". Three years of experience have not diminished the ability of seemingly identical glass tubes prepared in seemingly identical fashion to spring unexpected results on the author.

Before the alcohol-cooled dissociator could be used in an accelerator environment it would be necessary to show that the lower α values really were due to the glass surface of this particular tube, and that the dissociator is reliable over time periods of several weeks.

3.2.4 Dissociation of Nitrogen

A nucleus of a nitrogen (^{14}N) atom has a spin, I = 1, whilst the total electron angular momentum, J = $\frac{3}{2}$. The electron configuration in the ground state is $^4S_{\frac{3}{2}}$. The possibility has been raised [Dun82] that an ABS could be used select some of the 12 hyperfine states and create a polarised nitrogen target. This would be of interest to nuclear scattering experiments, but has also a possible application in high energy physics.

Deeply-virtual Compton scattering (DVCS) [GPV01] is a process in which an electron emits a (deeply) virtual photon, which interacts with a quark from the target nucleon, but unlike for DIS leaves the nucleon intact. The virtual photon transfers part of its momentum to the target nucleon, and a real photon is emitted. If both this photon and the scattered electron can be measured then it is possible to draw conclusions as to the structure of the nucleon.

DVCS is difficult to observe directly, as it competes with another process, known as the Bethe-Heitler process, which produces the same end result, and generally has a much larger reaction cross-section. Fortunately the amplitudes for the two processes, τ_{DVCS} and τ_{BH} add coherently, so that an interference term between the two processes is formed. This term is much larger than the DVCS amplitude alone, and allows DVCS processes to be observed at HERMES.

HERMES has an extensive program of DVCS research, examining polarised and unpolarised hydrogen and deuterium targets, and unpolarised nitrogen, neon and krypton targets. Interest has been expressed of whether it would be possible to measure DVCS on heavier polarised targets [Pol02], such as a polarised nitrogen target [Ama02]. The Bethe-Heitler cross-section scales with the square of the atomic number, so the interference term would be much larger for nitrogen than for hydrogen.

The first, and crucial stage of a polarised nitrogen source is production of atomic nitrogen in the required quantities. Molecular nitrogen has a dissociation energy of 945KJ/mol, or 9.8 eV. This is, incidentally, the strongest bond of any homodinuclear molecule. Tests with an 20 MHz RF dissociator [Dun82] produced less than 5% dissociation. The Microwave Dissociator (MWD) can, however, provide electrons with higher energies, and could be able to provide a larger degree of dissociation than the RF Dissociator.

Tests were made using the alcohol-cooled MWD in the ABS test stand. The resulting plasma was a very light blue in colour. The QMS is able to measure the relative intensities of atomic and molecular nitrogen in the beam, with a correction for dissociation occurring in the ionising volume of the QMS. The correcting factor was found by measuring the mass 14 rate with the dissociator turned off. The resulting degree of dissociation is less than 2% (see figure 3.10), a result confirmed by measurements with the recombination block of the test bench. An admixture of hydrogen (suggested by [Sou98] as an effective additive) produces an increased relative dissociation rate, but this small improvement cannot hide the overall disappointing results. QMS measurements showed that when hydrogen was added, there were no measurable signals at masses 15,16 or 17 (NH, NH_2 and NH_3) respectively, which shows that the problem is not recombination, but insufficient dissociation in the first place. An oxygen admixture produced no discernible effect.

It appears that the N_2 bond is too strong, and that a better prospect to produce atomic nitrogen would be, as suggested in [Dun82], to use ammonia (NH_3), nitric oxide (N0) or nitrous oxide ($N0_2$) instead of molecular nitrogen, as the bonds to be broken are weaker. Each of these gases, however, produces safety concerns and concerns regarding the effect on vacuum pumps and gauges and would require a special layout of the vacuum system which was not available. Therefore these studies have not been continued.

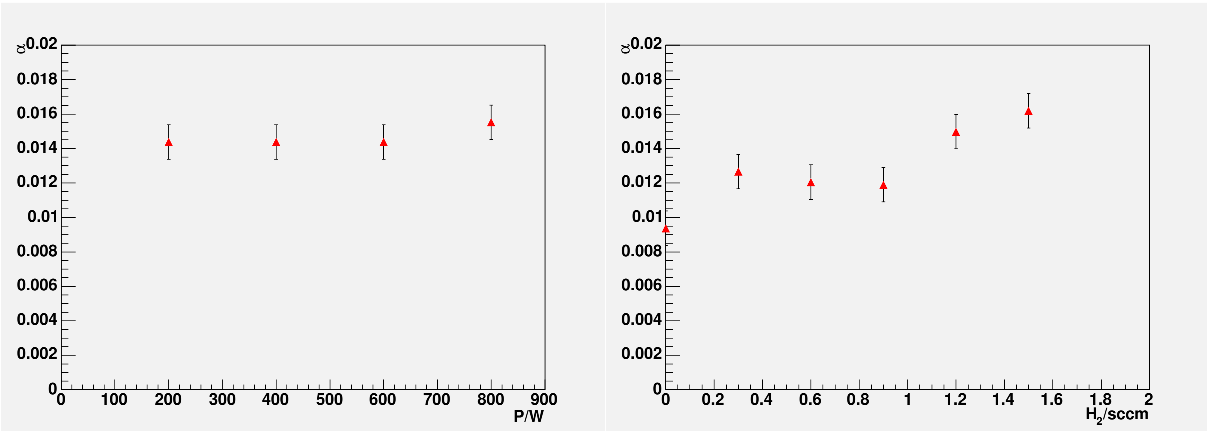

Figure 3.10: The dissociation degree α, as a function of microwave power, and of hydrogen admixture. In both cases, a nitrogen flow of 90 sccm was used. The power for the hydrogen scan was set to 800 W.

3.3 The Storage Cell

The target storage cell [Bau03], internal to the HERA electron ring, consists of a beam tube, 400 mm long, with 75 μm wall thickness and an elliptical cross-section of 21.0 mm x 8.9 mm. An injection tube connects the cell to the polarised source, and a sampling tube leads to the target diagnostic devices. This is shown in figure 3.11.

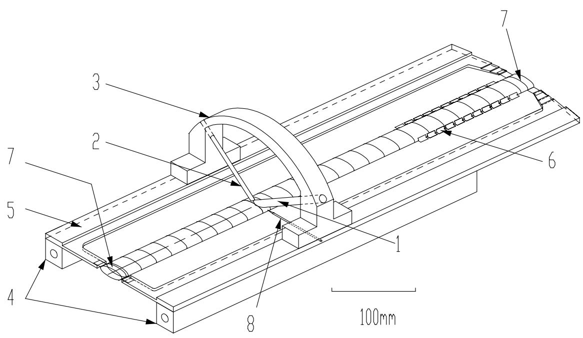

Figure 3.11: The target cell, with 1) injection tube; 2) sample tube; 3) Support Arch; 4) Cryogenic-cooling and support rails; 5) Support plates; 6) Cell extension with pumping apertures; 7) Cell end support collars; 8) Unpolarised gas feed capillary.

Atoms injected by the ABS reside in the target cell for a few ms, making several hundred wall collisions in this time, before exiting the cell through either the open ends of the beam tube, or through the sampling/injection tubes. The required UHV in the chamber surrounding the target cell (the target chamber) is achieved with two 2200 l/s turbo-molecular pump systems.

All inner surfaces of the target cell are coated with Drifilm in order to inhibit depolarisation and recombination on the surface of the cell. In order to increase the target density, and further reduce recombination, the cell is cooled (typically to 100K) by a Helium cooling system, which can cool the cell to temperatures as low as 35K. Experience with the storage cell has shown that an ice layer builds up on the surface of the cell, so that after several weeks of being kept at 100K, the recombination and depolarisation in the cell decreases. This is particularly evident for Drifilm coatings which have been damaged by radiation from the HERA electron beam.

3.4 The Transverse Target Magnet

The target magnet [Mar02] provides a homogeneous field across the whole dimensions of the target cell. The field defines the polarisation axis for target atoms, creates a nuclear polarisation for the mixed states $|2\rangle$ and $|4\rangle$, and reduces depolarising effects in the target cell by decoupling electron and nuclear magnetic moments.

The target magnet, along with all other target components, is designed so that it does not intrude into the acceptance of the HERMES spectrometer.

The working point of the field is 297 mT, which is directly halfway between two nuclear π resonances (see table 2.1)and is directed along the y axis. This field causes the electron beam to be bent in the x direction by the Lorentz force, therefore two additional dipole magnets, one before the target magnet and one after, are needed to keep the beam in a stable orbit. Although a higher target field could give higher polarisation, the chosen working point is a compromise between the benefits of a stronger holding field and the difficulties caused by deflecting the beam, such as synchrotron radiation, geometrical constraints of the target cell and the limited fields of the correction dipoles, especially the one after the target magnet. These problems are discussed in detail in [Reg03].

A further design constraint is that the magnet homogeneity must be sufficient to suppress σ_{24} beam-induced resonances. As shown in section 2.3.1, these resonances occur every 0.37 mT in the high-field limit. An ideal scenario would be that if the field in the centre of the cell is 297 mT, that the variation in field for all coordinates within the cell is less than one resonance spacing.

$$B(x,y,z)_{max} - B(x,y,z)_{min} < 0.37mT \tag{3.4}$$

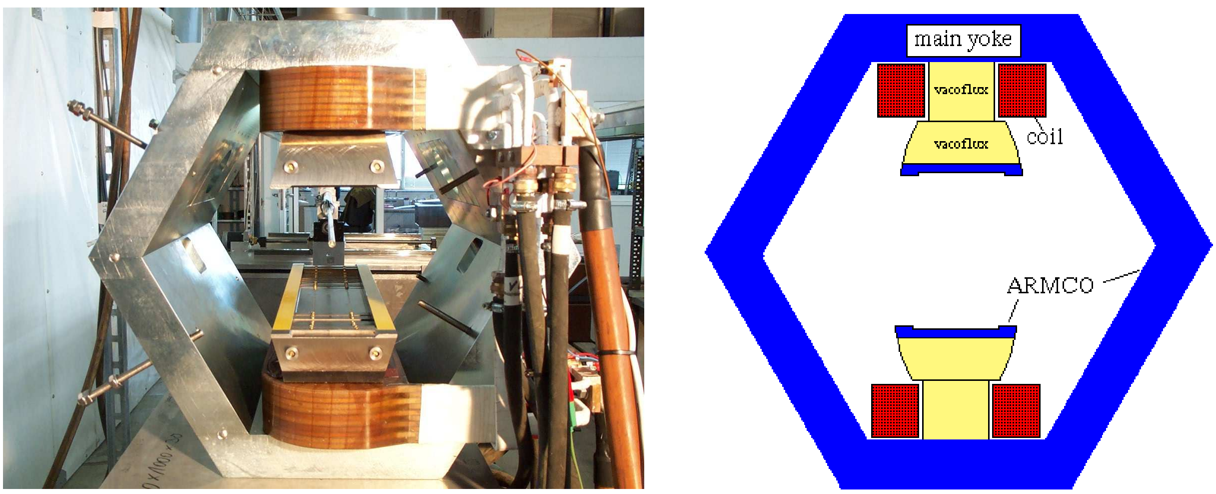

Figure 3.12: A photograph of the transverse target magnet (left) together with a schematic cross- section (right) showing the most important components. The shimming on the bottom pole can be seen in the photograph.

The magnet is a conventional magnet with yoke and pole-tips made of the magnet iron ARMCO, and the poles constructed from VACOFLUX 50[4]. A current of 545 A must be passed through the coils to reach the working field. The field homogeneity was optimised by "shimming"; adding small strips of ARMCO iron to the pole tips.

Due to spacial constraints the very strong condition laid out in equation 3.4 could not be achieved, and the homogeneities at 297 mT are $\Delta B_x = 0.60$ mT, $\Delta B_y = 0.15$ mT and $\Delta B_z = 0.05$ mT.

The holding field was measured [Sig03b] with a Hall probe which could be manipulated in three dimensions over the whole volume of the cell. For this measurement the magnet was run with 545 A, and the target chamber and cell were removed to allow the measurement to be made. The Hall probe is precise to within 1 μT, allowing the field inhomogeneities, which are less than 1 mT, to be accurately measured. A typical scan is made along one of the Cartesian axes, with the other two coordinates held constant. For a complete picture of the cell, many such measurements are then necessary (see appendix B). We can characterise the field from these measurements, however, as varying parabolically in the x and y directions, as shown in figure 3.13. Of particular concern here is the

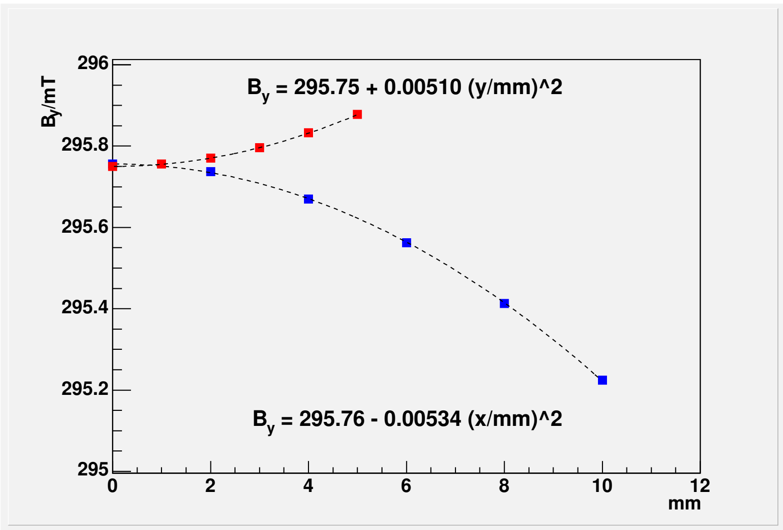

Figure 3.13: The y component of the holding field is shown as a function of position. Values for positive and negative x and y have been averaged.

x homogeneity, which could possibly be improved with an additional coil attached to the cell frame (see section 3.4.1.)

Long-term field measurements showed that after several hours the field dropped by up to 0.4 mT due to heating effects. To correct for this time-dependent behaviour, an additional coil with a maximum field contribution of 0.7 mT was added to the target magnet. The current passed through this additional coil (known as the "Yoke Coil" [Sig03]) is controlled by a feedback loop using a Hall Probe situated inside the target magnet, but outside of the vacuum system.

3.4.1 The Cell Correction Coil

Once it became apparent that the field homogeneity was insufficient to completely preclude σ resonances, a modified target cell was designed which contained an integrated coil which can be used to produce a magnetic field which varies approximately parabolically

[4]Trademark of Vacuumschmelze GmbH

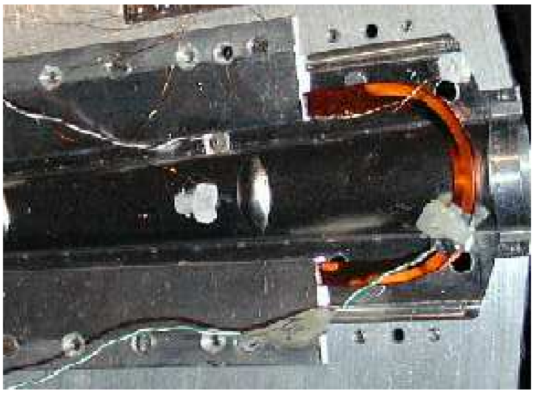

Figure 3.14: A photograph of the cell, complete with correction coil.

in the x direction. The copper coil is rectangular in cross-section, with a width of 6 mm and a height of 1 mm, and is insulated with Tenvex 200.

The cell correction coil (figure 3.14) was designed to provide an optimal correction to the target field throughout the length of the cell without placing additional material in the possible paths of particles passing from the inside of the cell to the HERMES detector. These design constraints result in a maximum current of 60 A which can safely be passed through the coil. In addition to the required x gradient of this field, the coil also has the effect of slightly increasing the total field in the cell. The additional field produced by this coil had been calculated [Sig04] using the MAFIA program, and is shown in figure 3.15, where the field gradient is of particular interest.

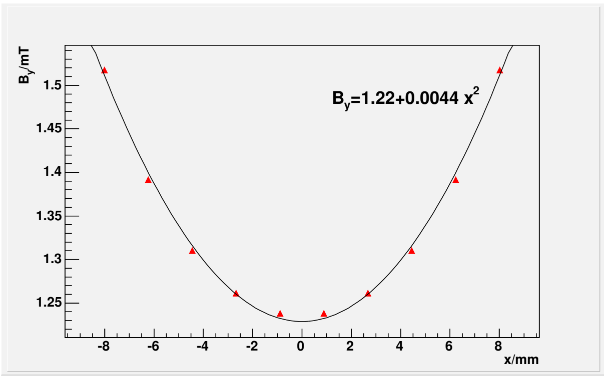

Figure 3.15: The additional field from the cell correction coil. The points are the results from a MAFIA calculation and the parabola is a fit to these points. No actual measurements of this field were made because of the fragile nature of the target cells.

3.5 The Target Gas Analyser (TGA)

Atomic polarisation is measured by the BRP. In order to measure the polarisation of all nucleons in the storage cell, it is necessary to know what proportion of the target gas is monatomic hydrogen. The TGA [Bau03b] consists of a quadrupole mass spectrometer (QMS), capable of measuring masses between 0 and 80 amu, together with a chopper system for background subtraction.

The TGA is tilted by 7° with respect to the sample tube, so that it does not interfere with the acceptance of the BRP. Atoms/molecules are detected, after passing through the quadrupole system, by a Channelling Electron Multiplier (CEM). In order to minimise the background signal, and to optimise the lifetime of the CEM, a pressure in the TGA of less than $5 \cdot 10^{-}9$ mbar is required. This is achieved by two cryo-pumps and a Titanium sublimation pump, with a combined pumping speed of roughly 7700 l/s, and a bake-out system with which the chamber can be heated to 200°C. The chopper system consists of a fork-like chopper which rotates at 5.5 Hz, with two baffles. The first baffle ensures that

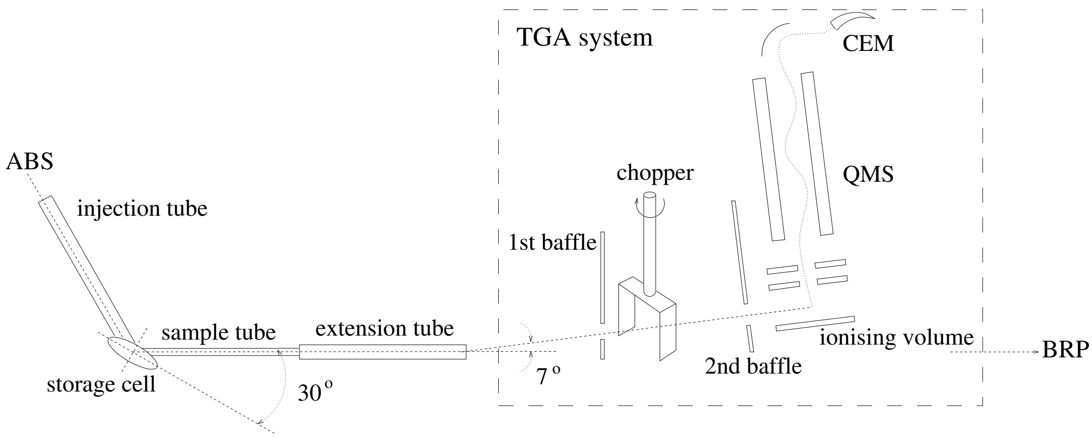

Figure 3.16: Schematic view of the TGA. Gas particles from a beam defined by the two baffles are detected by the quadrupole mass spectrometer.

only atoms originating from the extension tube can pass through the chopper; the second that atoms which have passed through the chopper cannot recombine on the ioniser before being detected. The signal from the sample tube can then be found by subtracting the chopper-closed signal from the chopper-open signal.

The TGA can be used to check that no heavier gases (such as N_2 or O_2) are present in the beam from the cell, but the standard measurement is the ratio of hydrogen atoms to hydrogen molecules. Hydrogen molecules can be injected from the ABS, or be formed from recombination in the cell, or reenter the cell after having recombined in the target chamber. All of these molecules can be detected by the TGA, and the atomic fraction as seen by the TGA is then described as

$$\alpha_{\text{TGA}} = \frac{S_a}{S_a + \sqrt{2}\kappa \cdot S_m} \tag{3.5}$$

where S_a and S_m are the atomic and molecular signals, and the factor $\sqrt{2}$ consists of a factor of 2 nucleons per molecule, and a factor of $1/\sqrt{2}$ because of the relative velocities, and therefore of times spent in the ionising volume. κ then includes all other detection efficiencies, and must be determined experimentally. κ is found to be roughly 0.6, and α_{TGA} is usually above 0.95.

A crucial requirement for the measurement, as described above, is that the detector response is linear to the number of incoming atoms/molecules of the set mass. With correct use of the QMS, this is found to be the case.

3.6 The Breit-Rabi Polarimeter (BRP)

The so-called Breit-Rabi Polarimeter (BRP) [Gau92][Bau02] measures the polarisation of hydrogen atoms originating from the cell. A 0.2 T holding field produced by a Halbach dipole inhibits wall depolarisation in the extension tube. Atoms pass through two hyperfine transition units (HFTs) before entering the sextupole system, which, as in the ABS, removes states with $m_S = -\frac{1}{2}$ from the beam, whilst focusing the remaining states onto the detector. A beam blocker on the beam axis ensures that no atoms with $m_S = -\frac{1}{2}$ can reach the detector. Unlike the ABS, where intensity is crucial, and a small contamination with other states is relatively unimportant, the BRP requires maximal accuracy in order to keep systematic errors low, thus the beam blocker is essential. Through several measurements, each with the HFTs in a different setting, it is possible to calculate the relative populations of the four hyperfine states, and thereby the atomic polarisation.

The BRP detector is a quadrupole mass spectrometer (QMS), identical to that for the TGA. Base pressure in the detector chamber is typically $1 \cdot 10^{-10}$ mbar, ensuring optimal conditions for the QMS and Channeltron. As the BRP measures only atoms, a baffle system such as for the TGA is not necessary. Instead, any fake atomic signal caused by dissociative ionisation of hydrogen or water molecules is found and corrected for using the beam shutter. The components of the BRP are shown in figure 3.17.

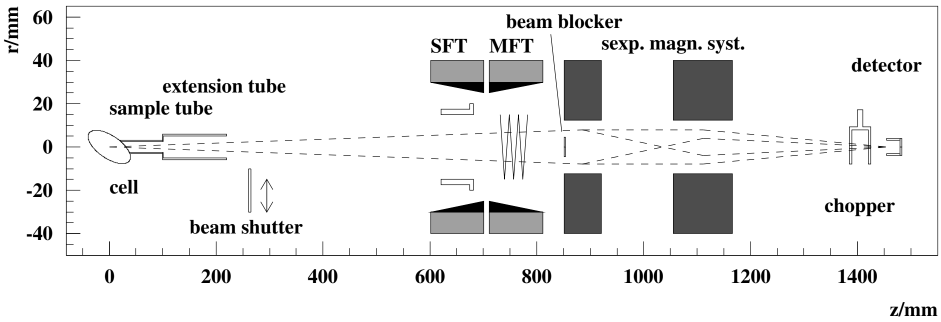

Figure 3.17: A schematic view of the BRP, showing the path of the atomic beam through the components. The strong field (SFT) and medium field (MFT) transition units can exchange hyperfine states before they are filtered by the sextupole magnet system.

3.6.1 The High Frequency Transitions (HFTs)

Although the HFTs in the BRP work on the same principle as those in the ABS (see section 3.1.3), the differences are interesting enough to note. The BRP SFT is capable of performing both π_{14} and σ_{24} transitions. This is achieved through the use of tilted resonator rods, which create, relative to the static field, both a parallel and perpendicular component. The BRP MFT can be operated as a simple transition between states $|1\rangle$ and $|2\rangle$, or $|2\rangle$ and $|3\rangle$, or also as a double transition in which both transitions occur successively. The direction of the gradient field determines whether the $1 \leftrightarrow 2$ or the $2 \leftrightarrow 3$ transition is performed first. In the case that the $1 \leftrightarrow 2$ occurs first (negative gradient), the result is, assuming perfect behaviour, as follows.

$$\begin{pmatrix} n_1 \\ n_2 \\ n_3 \\ n_4 \end{pmatrix} \xrightarrow{1\leftrightarrow 2} \begin{pmatrix} n_2 \\ n_1 \\ n_3 \\ n_4 \end{pmatrix} \xrightarrow{2\leftrightarrow 3} \begin{pmatrix} n_2 \\ n_3 \\ n_1 \\ n_4 \end{pmatrix} \xrightarrow{\text{Sixpole}} \begin{pmatrix} n_2 \\ n_3 \\ 0 \\ 0 \end{pmatrix} \tag{3.6}$$

As the result is that the BRP detects states $|2\rangle$ and $|3\rangle$, this transition is known as the MFT_{13}, even though it does not directly swap states $|1\rangle$ and $|3\rangle$. The MFT is, from a design point of view, identical to the ABS WFT. The only difference is that it is run at a higher frequency.

The BRP is capable of measuring all possible two-state combinations, as shown in table 3.2. These six measurements form an over-determined set of equations with which the relative populations of the four hyperfine states can be calculated.

SFT status	MFT status	Meas. States
Off	Off	$\|1\rangle, \|2\rangle$
SFT 1-4	Off	$\|4\rangle, \|2\rangle$
SFT 2-4	Off	$\|1\rangle, \|4\rangle$
Off	MFT 1-3	$\|2\rangle, \|3\rangle$
Off	MFT 2-3	$\|1\rangle, \|3\rangle$
SFT 1-4	MFT 2-3	$\|4\rangle, \|3\rangle$
SFT 1-4	MFT 1-3	$\|2\rangle, \|3\rangle$
SFT 2-4	MFT 2-3	$\|1\rangle, \|3\rangle$
SFT 2-4	MFT 1-3	$\|4\rangle, \|3\rangle$

Table 3.2: The possible measurement modes of the BRP. Only the first six are used for a standard polarisation measurement, as they cover all possible combinations of measurements.

3.6.2 Calibration of the BRP

Until now we have considered only the ideal case of the BRP. In reality the hyperfine transitions have an efficiency of less than 1. It is necessary, therefore, to assign an exchange probability for each transition, for example ϵ_{14} for the SFT 1-4 transition.

$$\begin{pmatrix} n_1 \\ n_2 \\ n_3 \\ n_4 \end{pmatrix} \xrightarrow{\text{SFT}_{14}} \begin{pmatrix} (1-\epsilon_{14})n_1 + \epsilon_{14}n_4 \\ n_2 \\ n_3 \\ (1-\epsilon_{14})n_4 + \epsilon_{14}n_1 \end{pmatrix} \tag{3.7}$$

A further complication is caused by the feature of the BRP that the holding field of the SFT produces a fringe field which is strong enough to influence the operation of the MFT. This results from the close vicinity of these units to each other. The MFT transitions, which would in any case need two efficiencies; one each for the $1 \leftrightarrow 2$ and $2 \leftrightarrow 3$ sub-transitions, must now be described separately for the two possible SFT positions. In order to avoid the further complication of a third SFT position, the SFT holding field is always set to either the field for the $1 \leftrightarrow 4$ or $2 \leftrightarrow 4$ transitions, even when the SFT (ie its HF field) is turned off.

The sextupole transmissions of states $|1\rangle$ and $|2\rangle$ are not identical, due to the magnetic moment of the nucleus. The beam blocker ensures, however, that states $|3\rangle$ and $|4\rangle$ are completely removed from the beam. Thus the sextupole system can be accurately described by the relative transmission efficiency σ_{21}, which is the ratio of the transmission probabilities of state $|2\rangle$ to $|1\rangle$.

In total 11 efficiencies must be found; 10 for the HFTs and one for the sextupole system. The calibration measurement is performed by sequentially switching through all the nine possible BRP settings as detailed in table 3.2, with the additional two settings that when the MFT is used alone, the SFT holding field can be set to either the SFT 1-4 or SFT 2-4 setting. The calibration evaluation routine uses the requirement that the initial hyperfine state population (ie that before the BRP SFT) is independent of the BRP setting. Roughly five minutes are needed to cycle through the 11 BRP settings, and within this time the ABS can easily be assumed to deliver a constant output, and provided there is no HERA electron beam present, the cell properties will also not change.

In order to create enough linear equations to solve the system, it is necessary to repeat the process for different ABS injections. Optimal results were found by injecting all eight operating modes listed in table 3.1. The different intensities delivered for two-state, one-state and zero-state injection cause no problem. The only requirement from the ABS is that the injected intensity and polarisation is constant during the time needed to measure for all 11 BRP settings. The ABS injections must differ sufficiently to create in each case unique initial hyperfine populations for the BRP. In practice, depolarising effects in the cell will alter the hyperfine populations before the atoms reach the BRP. It would, in theory, be possible to make a BRP calibration by changing the ABS intensity only (spin-exchange effects in the cell would then cause the initial hyperfine population to change) or by changing the cell temperature (to increase wall depolarisation). The ABS transitions, however, provide the fastest and most effective method of creating different hyperfine populations to enter the BRP.

The complete set of equations then consists of 88 (8 ABS times 11 BRP) linear equations, with which to find the 11 missing BRP efficiencies, and the 32 initial hyperfine state populations (8 ABS settings with 4 hyperfine states). The calibration evaluation starts with an estimate of the initial hyperfine populations, and passes them through the BRP transitions (as in equation 3.7), to produce the predicted measured signals for each BRP setting. An iterative optimisation then occurs, in which the initial hyperfine population and BRP efficiencies are adjusted to best reproduce the measured results, which are weighted as to their statistical errors.

The calibration technique is blissfully ignorant of depolarising effects before the BRP SFT, which makes it perfect for use with a storage cell. It is, however, dependent that the BRP works exactly as defined by the calibration efficiencies. Thus a transition which is defined as being a $1 \leftrightarrow 4$ transition is not allowed to perform any $2 \leftrightarrow 4$ effect. Provided that the holding and gradient fields are carefully selected, this is not a problem. Particular care must be taken with the relative orientation of the holding fields of the SFT and MFT, which are both transverse to the path of the BRP beam. If the field of the SFT points down, then the MFT must do the same. If the fields are opposed, then there must be a point in-between at which the fringe fields of the transitions cancel, a so-called zero-field crossing. The total holding field at this point will be very low, and will probably be dominated by the fringe fields of the target or spectrometer magnets. Thus the holding field will change in orientation by 180° within the space of a few cm, in a very low holding field.

In these circumstances, an unwanted transition will take place located between the SFT and MFT. Such an effect is not considered in the BRP calibration evaluation code, and is probably too unstable and unpredictable to ever be included. Provided that the field directions are carefully selected this is no problem.

The result of the BRP calibration is shown in table 3.3. Note that the calibration evaluation routine does not place any physical limits on efficiencies (e.g. that it be between 0 and 1). All transitions which should be are very close to 1, and the $1 \leftrightarrow 2$ part of the MFT 2-3 transition is very close to zero. There is very little (if any) difference between the MFT efficiencies for the 1-4 and 2-4 SFT field settings, presumably because the MFT was optimised for each setting. The physical argument, however, that the efficiencies *could* be different is firm, and the only way to rule out this possibility is with such a calibration.

Compared to the 1997 hydrogen BRP calibration, the statistical error has dropped by a factor of four. This is mainly due to the improved BRP sextupole system, which was modified in 2002 to increase the detection efficiency of the BRP [Bru01]. σ_{21} was also found in the calibration evaluation. In 1997 the final value of σ_{21} was found by averaging the σ_{21}

values from all calibrations during the year (one of the many advantages of permanent sextupole magnets is that their properties do not change over time. Actually, this is the only advantage, but it is an important one, and ought to be counted more than once). Here, σ_{21} can be found to the required precision within one calibration. The aforementioned modification of the sextupole system is presumably the reason that σ_{21} has changed from 1.029 ± 0.0015 to the present value. The development of the calibration

Transition	Sub Transition	SFT **B**	ϵ	Stat. Err
SFT 1-4	-	-	0.9911	0.0021
SFT 2-4	-	-	0.9998	0.0022
MFT 1-3	1-2	1-4	0.9893	0.0038
MFT 1-3	1-2	2-4	0.9842	0.0036
MFT 1-3	2-3	1-4	0.9902	0.0037
MFT 1-3	2-3	2-4	0.9946	0.0035
MFT 2-3	1-2	1-4	0.0070	0.0025
MFT 2-3	1-2	2-4	0.0033	0.0025
MFT 2-3	2-3	1-4	0.9735	0.0032
MFT 2-3	2-3	2-4	0.9628	0.0026
σ_{21}	-	-	0.9902	0.0037

Table 3.3: The Resulting efficiencies from the BRP calibration (run 1693) in 2004. 12 complete ABS cycles were taken for this measurement, for which 5 hours were needed. Checks show that the measurement was stable during this time. The efficiencies were then found from the averaged results.

procedure and details of the algorithm used to find the efficiencies can be found in [Bau02, Bau00]. An alternative algorithm to find the efficiencies was presented in [Hen03].

3.7 Intra-Beam Scattering in the ABS

A result of the BRP calibration is that in addition to the required efficiencies, the initial hyperfine-state population of atoms entering the BRP is found. In other words, the calibrated BRP can be used to measure the target density, albeit with an unknown factor which represents the transmission probability of the sextupole system and the detection efficiency of the QMS. The total BRP signal (the sum of all four hyperfine-state signals) is shown for each of the eight ABS injection modes in 3.4.

The total signals are firstly a good check of the reliability of the calibration results, as we expect that all injection modes which differ only by the state of the appendix transitions should give equal signals. The total signals can also be used to gain information about losses in the second sextupole system of the ABS caused by intra-beam scattering.

Intra-beam scattering occurs in the ABS as a result of transverse motion, or longitudinal motion relative to the average velocity of the beam. Atoms collide with other atoms in the beam, after which one or both of the atoms is lost from the beam. The losses due to intra-beam scattering are then proportional to the square of the beam intensity.

$$\frac{\Delta\Phi}{\Phi} \propto \Phi \tag{3.8}$$

HFT (betw. 6-poles)	HFT (appendix)	Inj. States	Signal/kHz	Stat. Err/kHz
-	-	$\vert 1\rangle$, $\vert 2\rangle$	87.89[a]	0.19
-	WFT 1-3	$\vert 2\rangle$, $\vert 3\rangle$	87.95[a]	0.25
-	SFT 2-4	$\vert 1\rangle$, $\vert 4\rangle$	86.67[a]	0.12
SFT 2-4	-	$\vert 1\rangle$	52.78[b]	0.067
WFT 1-3	-	$\vert 2\rangle$	51.39[c]	0.17
SFT 2-4	WFT 1-3	$\vert 3\rangle$	52.81[b]	0.12
WFT 1-3	SFT 2-4	$\vert 4\rangle$	50.48[c]	0.089
WFT 1-3, SFT 2-4	-	none	12.06	0.028

Table 3.4: The measured total BRP signals for the eight ABS injection modes, for the calibration from table 3.3. The signal should be equal for injection modes with the same setting of HFTs between the sextupoles, as the Appendix HFT position cannot effect the probability of an atom entering the cell. We expect, therefore, that all signals labelled a, b or c should be identical.

It would then be expected that the relative losses would be higher for two-state injection than for one-state by a factor of two. The calculation is complicated by the facts that the ABS transitions do not work with 100% efficiency, and the sextupole magnets do not completely eliminate states $|3\rangle$ and $|4\rangle$. The composition of the beam after the first sextupole magnet is

$$\begin{pmatrix} n_1 \\ n_2 \\ n_3 \\ n_4 \end{pmatrix} \tag{3.9}$$

where n_3 and n_4 are expected to be much smaller than n_1 and n_2. For the case that no HFTs are activated between the sextupole systems, the injected beam, S_{1+2} will be

$$S_{1+2} = (1-x)\begin{pmatrix} \sigma_1 n_1 \\ \sigma_2 n_2 \\ \sigma_3 n_3 \\ \sigma_4 n_4 \end{pmatrix} \tag{3.10}$$

where x refers to the intra-beam losses of a two-state beam, and σ_i to the probability of an atom, which enters the second sextupole system in state i, entering the injection tube. For the case that the WFT 1-3 is activated, the injected beam will be

$$S_2 = \left(1-\frac{x}{2}\right)\begin{pmatrix} \sigma_1(n_1+\epsilon_{13}(n_3-n_1)) \\ \sigma_2 n_2 \\ \sigma_3(n_3+\epsilon_{13}(n_1-n_3)) \\ \sigma_4 n_4 \end{pmatrix} \tag{3.11}$$

with a fractional beam loss due to intra-beam scattering which is, to a first-order approximation, half the value for two-state injection. The equivalent expression if the SFT 2-4 is used instead of the WFT 1-3 is

$$S_1 = \left(1-\frac{x}{2}\right)\begin{pmatrix} \sigma_1 n_1 \\ \sigma_2(n_2+\epsilon_{24}(n_4-n_2)) \\ \sigma_3 n_3 \\ \sigma_4(n_4+\epsilon_{24}(n_2-n_4)) \end{pmatrix} \tag{3.12}$$

and if both the SFT 2-4 and WFT 1-3 are used between the sextupoles, then the resulting beam entering the injection tube is as following.

$$S_0 = \begin{pmatrix} \sigma_1(n_1 + \epsilon_{13}(n_3 - n_1)) \\ \sigma_2(n_2 + \epsilon_{24}(n_4 - n_2)) \\ \sigma_3(n_3 + \epsilon_{13}(n_1 - n_3)) \\ \sigma_4(n_4 + \epsilon_{24}(n_2 - n_4)) \end{pmatrix} \tag{3.13}$$

We can then compare the sum of the cases $S_{1+2} + S_0$ with $S_1 + S_2$. Thus

$$S_{1+2} + S_0 = (1-x)\begin{pmatrix} \sigma_1 n_1 \\ \sigma_2 n_2 \\ \sigma_3 n_3 \\ \sigma_4 n_4 \end{pmatrix} + \begin{pmatrix} \sigma_1(n_1 + \epsilon_{13}(n_3 - n_1)) \\ \sigma_2(n_2 + \epsilon_{24}(n_4 - n_2)) \\ \sigma_3(n_3 + \epsilon_{13}(n_1 - n_3)) \\ \sigma_4(n_4 + \epsilon_{24}(n_2 - n_4)) \end{pmatrix} \tag{3.14}$$

and

$$\begin{aligned} S_1 + S_2 &= (1-\frac{x}{2})\begin{pmatrix} \sigma_1(n_1 + \epsilon_{13}(n_3 - n_1)) \\ \sigma_2 n_2 \\ \sigma_3(n_3 + \epsilon_{13}(n_1 - n_3)) \\ \sigma_4 n_4 \end{pmatrix} + (1-\frac{x}{2})\begin{pmatrix} \sigma_1 n_1 \\ \sigma_2(n_2 + \epsilon_{24}(n_4 - n_2)) \\ \sigma_3 n_3 \\ \sigma_4(n_4 + \epsilon_{24}(n_2 - n_4)) \end{pmatrix} \\ &= (1-\frac{x}{2})\begin{pmatrix} \sigma_1 n_1 \\ \sigma_2 n_2 \\ \sigma_3 n_3 \\ \sigma_4 n_4 \end{pmatrix} + (1-\frac{x}{2})\begin{pmatrix} \sigma_1(n_1 + \epsilon_{13}(n_3 - n_1)) \\ \sigma_2(n_2 + \epsilon_{24}(n_4 - n_2)) \\ \sigma_3(n_3 + \epsilon_{13}(n_1 - n_3)) \\ \sigma_4(n_4 + \epsilon_{24}(n_2 - n_4)) \end{pmatrix} \end{aligned} \tag{3.15}$$

We now make a simplification, and assume that the second term in 3.14 is small, so that we can insert a factor of $1 - x$ in front of it. As this term contains all of the "junk", i.e. the deviations from a perfect ABS, and x is small, this should not be a problem for an ABS which is well built and tuned. The "junk" term itself is too large to disconsider, but the amount of intra-beam scattering caused by this term is a second order effect, and *can* be disregarded, which is what we do here. It then follows that

$$\frac{S_{1+2} + S_0}{S_1 + S_2} = \frac{1-x}{1-\frac{x}{2}} \tag{3.16}$$

and rearranging this gives

$$\frac{x}{2} = \frac{1 - \frac{S_{1+2}+S_0}{S_1+S_2}}{2 - \frac{S_{1+2}+S_0}{S_1+S_2}}. \tag{3.17}$$

The measurements as shown in table 3.4 can then be used to find the coefficient of intra-beam scattering. The measured rate should not depend on the state of the appendix transitions, so the results of the first three rows can be averaged to find the measured signal for S_{1+2}. As for two of the measurements, the measured rates differ by vastly more than the statistical error, the standard deviation of these signals from the calculated mean has been used to estimate the systematic error of a measurement. Applying these signals to equation 3.17 gives $x = 0.077 \pm 0.020$. This value is in agreement with the value of 0.084 ± 0.016 presented in the paper [Ye04], based on an earlier calibration.

Note that such a measurement could be made with any intensity-measuring device in place of the BRP, provided the required precision and accuracy is achieved. In principle, the TGA signal could also be used to make a measurement of Intra-beam scattering, but in practice the relatively poor background conditions of the TGA excluded this possibility. A set-up designed specifically to investigate intra-beam scattering would measure the intensity of the beam at the point of injection, either through a quadrupole mass spectrometer or a calibrated compression tube.

Measurement	Signal/kHz	Syst. Error/kHz	Stat. Error/kHz
S_{1+2}	87.50	0.59	0.11
S_1	52.80	0.0	0.1
S_2	50.94	0.45	0.09
S_0	12.06	0.	0.028

Table 3.5: The averaged measurements, based on table 3.4, used to find the degree of intra-beam scattering.

Chapter 4

Simulations of Beam-Induced Depolarisation with the Transverse Magnet

Wir operieren mit lauter Dingen, die es nicht gibt, mit Linien, Flächen, Körpern, Atomen, teilbaren Zeiten, teilbaren Räumen -, wie soll Erklärung auch nur möglich sein, wenn wir Alles erst zum Bilde machen, zu unserem Bilde!

Friedrich Nietzsche

4.1 Introduction

For the simple case of a hydrogen atom in a holding field B_y, subjected to a sinusoidal high frequency field B_{HF} for a time τ, the probability of a flip to another state can be calculated using the results of time-dependent perturbation theory. (see section 2.2.3). An ensemble of atoms in a storage cell is a much more complex case: The HF and holding fields are dependent upon the position in the cell, and the atoms progress with a random diffusion following each wall bounce in the cell. An important simplification is that each atom can be treated independently, as the depolarising effect occurs between a single atom and the beam-induced field. Although other depolarising effects, such as wall depolarisation and spin-exchange collisions occur in parallel with beam-induced depolarisation, they can (and have) been dealt with separately. So although a complete model of all depolarising processes must consider atom-atom interactions, they can be ignored for the study of beam-induced effects.

It is typically assumed (see for example [Kol98] and [Gil93]) that the high frequency field drops with a $\frac{1}{r}$ dependence outside the electron beam. The holding field, however, can assume almost any form, depending on the construction of the target magnet. It is generally desirable that the field should be as homogeneous as possible in the cell region, but some variation in all three spacial directions is to be expected. Because of the spacial dependence of the holding field, the particular conditions necessary for a resonance to be induced by the beam will only be met at certain points in the cell, namely those where the holding field is such that the energy difference between two states matches exactly the frequency of a harmonic of the beam.

$$\omega_{\mathrm{HF}} = \omega_{ab} = \frac{|E_a(\mathbf{r}) - E_b(\mathbf{r})|}{\hbar} \tag{4.1}$$

As the holding field contains no discontinuities, these points will join up to form a resonant surface, upon which the resonance condition is exactly fulfilled. Imagine, for example, a typical storage cell as shown in figure 4.1. We assume that the holding field only varies along the z axis, so that the resonant surfaces will be flat and in the $x-y$ plane. The

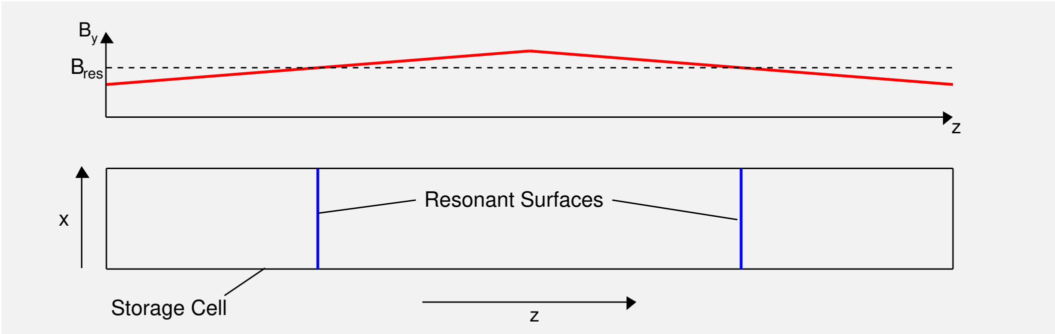

Figure 4.1: A view of a storage cell together with its variation in holding field (top). The positions of the resonances are shown.

picture of resonant surfaces, however, does not give a complete description of depolarising resonances. Because of the time-energy uncertainty principle, the frequency of the time-dependent field must not *exactly* match the energy difference of our start and final states. Thus the holding field must only approximately match the field required for resonance, so the resonant surface will become a three-dimensional region, as shown in figure 4.2. But to within what tolerance must the field match the resonant value, and how far in space will the resonant region therefore extend? This will depend on the time needed to pass through the resonant surface, τ. This leads us to a potentially confusing argument: The further the resonant region extends in z, the longer the time needed to pass it will be. But a longer time means a better defined energy, and therefore a shorter resonant region. This somewhat unfamiliar premise should not prevent us calculating the time needed, τ.

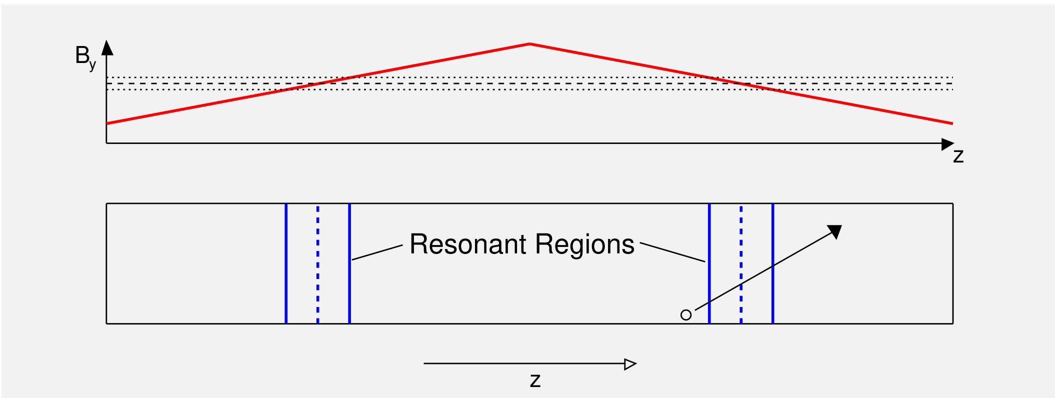

Figure 4.2: The uncertainty in energy corresponds to a width of holding field (top, dotted lines), which in the storage cell results in an extended spacial region where the resonance can occur.

4.1.1 An Expression for τ, the Resonance Crossing Time

A result of time-dependent perturbation theory (see section 2.2.3) is that transitions are possible for an ω_{HF} which does not perfectly match the transition frequency, provided that the inequality

$$|(\omega_{\mathrm{HF}} - \omega_{ab})\,\tau| < 2\pi \tag{4.2}$$

is fulfilled. Writing ω_{ab} as $\omega_0 + d\omega(x, y, z)$ gives

$$|(\omega_{\mathrm{HF}} - \omega_0 - d\omega\,(x, y, z))\,\tau| < 2\pi. \tag{4.3}$$

ω_0 can freely be defined to be equal to ω_{HF}; this simply means that at the considered position in the cell, the resonance condition is met exactly. Moving in x and y away from this position will result in a non-zero value of $d\omega$.

$$d\omega\,(x, y, z) = \frac{\partial\omega}{\partial B_y}\frac{\partial B_y}{\partial x}dx + \frac{\partial\omega}{\partial B_y}\frac{\partial B_y}{\partial y}dy + \frac{\partial\omega}{\partial B_y}\frac{\partial B_y}{\partial z}dz \tag{4.4}$$

and inserting this into inequality 4.3 gives

$$\left|\frac{\partial\omega}{\partial B_y}\left(\frac{\partial B_y}{\partial x}dx + \frac{\partial B_y}{\partial y}dy + \frac{\partial B_y}{\partial z}dz\right)\tau\right| < 2\pi. \tag{4.5}$$

The particle passing through the resonance is travelling with constant velocity, $\mathbf{v}$, so we can write

$$\left|\frac{\partial\omega}{\partial B_y}\left(\frac{\partial B_y}{\partial x}v_x + \frac{\partial B_y}{\partial y}v_y + \frac{\partial B_y}{\partial z}v_z\right)\tau^2\right| < 2\pi \tag{4.6}$$

and as $\frac{\partial\omega}{\partial B_y}$ is in the case of hydrogen always positive, the above inequality becomes

$$\tau^2 = \frac{2\pi}{\frac{\partial\omega}{\partial B_y}\left|\frac{\partial B_y}{\partial x}v_x + \frac{\partial B_y}{\partial y}v_y + \frac{\partial B_y}{\partial z}v_z\right|} \tag{4.7}$$

which can be expressed in the vector form

$$\tau^2 = \frac{2\pi}{\frac{\partial\omega}{\partial B_y}\left|\nabla B_y \cdot \mathbf{v}\right|} \tag{4.8}$$

This is an important equation, and worth some discussion. The time spent in the resonant region varies, not with the inverse of velocity, as for a classical region, but with $1/\sqrt{v}$. This arises because the extent of the resonant region depends on the time spent in it, so the faster a molecule is moving, the larger the resonant region will be in space. The term $\frac{\partial\omega}{\partial B_y}$ means that nuclear π transitions will apply for a longer time than other beam-induced transitions (see figure 2.3).

4.1.2 The Characteristic Length

By multiplying τ by the velocity of the particle, it is possible to find the length of the resonant region. This length is a very important characteristic, as we shall see. It is of great importance whether this length is shorter or longer than various dimension of the cell. To illustrate this we consider the effects of different holding fields (∇B_y) and transitions ($\frac{d\omega}{dB}$), which influence τ and therefore also the characteristic length.

The Longitudinal Magnet

To begin with, we consider the HERMES storage cell with the longitudinal magnet, as used from 1995 until 2001. The holding field was aligned along the z axis, and the field inhomogeneity was most pronounced in the z direction, as shown in figure 4.3. The field gradient depends on z position, but as an example we take a point where the gradient is roughly 0.1 mT/mm. The thermal velocity is given by $v = \sqrt{\frac{3k_B T_{\rm cell}}{m_p}}$, and the temperature of the cell can be taken to be 100K, giving a velocity of $v = 1570$ m/s. To a first approximation, the z component will be $v/\sqrt{3}$. We can then use equation 4.7 to find the time and length of the depolarising effect (see table 4.1). Note that the resonant region

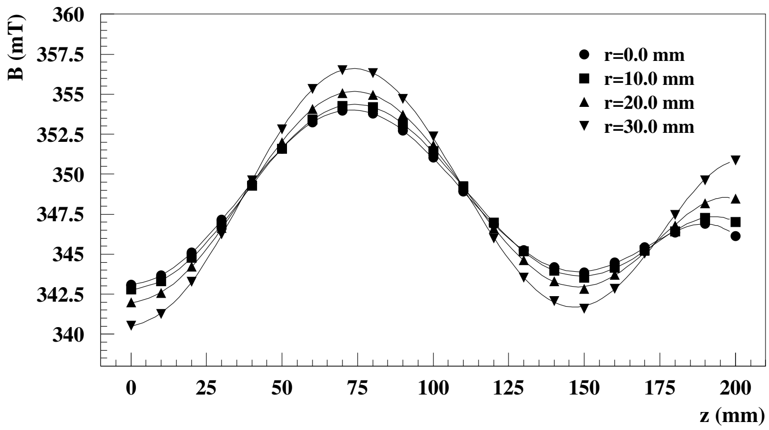

Figure 4.3: The magnetic field of the longitudinal target magnet, shown as a function of z position measured at a radius r from the beam axis.

Transition	$\frac{d\nu}{dB}$	τ/μs	τv/mm
π_{12}, π_{34}	0.56 MHz/mT	4.40	4.02
π_{23}, π_{14}	27.4 MHz/mT	0.63	0.58

Table 4.1: Times and characteristic lengths for resonant depolarisation with the longitudinal magnet. The ratio of holding to critical field, B/B_c is taken to be 7. It is assumed that the particle is moving with a thermal velocity, as described in the text , and the z homogeneity is taken to be 0.1 mT/mm

is so large in the case of the nuclear transitions, that it is comparable to the x and y dimensions of the cell. An atom will typically move by only a few mm in the z direction after wall desorption, so it will effectively spend a whole crossing of the cell within the depolarising region. So this one condition for depolarisation is easily fulfilled, and the more pertinent question is "How close does the atom get to the electron beam?". This question has already been addressed, under the assumption that the resonant frequency condition is fulfilled in certain regions of the cell, by Kolster [Kol98],[Ack99] and Graw [Gra98]. We should note, before moving on, that the depolarising region will be longest when the field homogeneity is at its best. Kolster found that if the field were set so the resonance occurred in the centre of the cell, or at the first maximum of 75 mm, then the depolarisation was at its strongest.

For the electron transitions, on the other hand, the extent of the resonance along z is very small: less than 1 mm. So a particle crossing the cell, should it happen to pass through the z position where the resonant surface is located, will typically only experience the resonance for a short part of its trip. It is then possible to say that the particle crossed

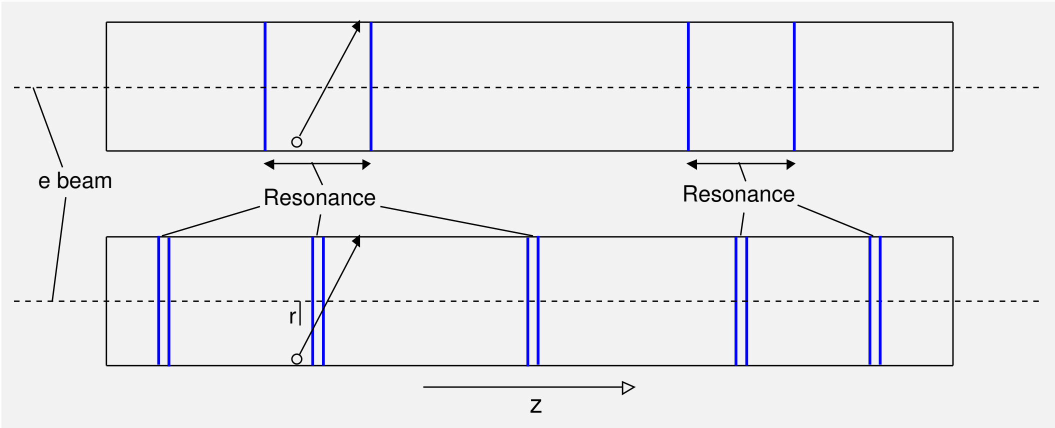

Figure 4.4: The resonant regions for in the longitudinal target magnet. For nuclear π resonances (top) the atom spends the whole time crossing the cell in the resonant region. The crucial factor is how close its path comes to the electron beam (remember that in three dimensions it need not pass through the beam, but must have a point of closest approach). For electron π resonances (bottom) the atom is only in the resonant region for a short time, and experiences the resonance at a distance r from the electron beam, which in general will be further than the point of closest approach.

the resonant region at a distance r from the electron beam, and therefore to calculate the transient beam-induced field at this point. The contrast between the cases of nuclear and electron π resonances in the longitudinal magnet is shown schematically in figure 4.4

The Transverse Magnet

Now suppose that the magnet is built such that the holding field does not depend on z, but only on the x position. This may at first seem an unlikely scenario, as storage cells are generally much longer than they are wide, in order to keep the conductance low. However, for the transverse target magnet, this is roughly the situation. We can make a sketch of the positions of the resonant surfaces, as shown in figure 4.5.

The field homogeneity of the transverse magnet, $\frac{\partial B}{\partial x}$, depends on the x position, but is of the order of 0.025 mT/mm. Thus τ and the characteristic length will be roughly twice as large as for the values for the longitudinal magnet in table 4.1.

If τv is small compared to the x dimension of the cell, as will be the case for σ and electron π transitions, then the resonance condition will only be met in a narrow band around the resonant surface, and if the resonant surface is far from the electron beam then atoms will never experience the resonant condition with strong transient fields. Compare this to the bottom scenario in figure 4.4, where atoms *could* see the resonance condition close to the beam, if they happened to cross the resonant surface in the centre of the cell. Here the possibility no longer exists.

For nuclear π transitions, τv is longer than the x dimension of the cell, so the resonance condition will be fulfilled throughout the whole cell! The critical aspect of each passage is then the point of closest approach. The strength of the resonance will depend then on exactly how well the holding field matches the resonant field value. No diagram is drawn for this scenario, as it would simply be a blue-filled storage tube!

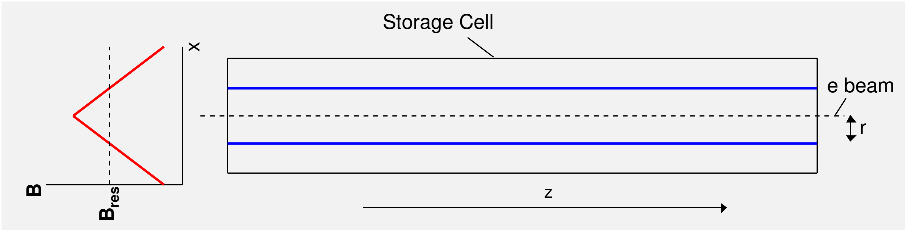

Figure 4.5: If the holding field varies only in x, then the resonant surface (blue line) is at a fixed distance, r, from the electron beam.

4.1.3 Approaches to Modelling the Depolarisation

Transition	Δm_S	Δm_I	Spacing Coefficient	Matrix Element
π_{12}, π_{34}	0	±1	$\frac{1}{\sin^2\theta}$	$\sin^2\theta$
π_{23}, π_{14}	±1	0	$\frac{1}{\cos^2\theta}$	$\cos^2\theta$
σ_{24}	±1	∓1	$\frac{1}{\cos^2 2\theta}$	$\sin^2 2\theta$

Table 4.2: A reminder of the characteristics of all possible resonances, as derived in chapter 2. π_{12} and π_{34} resonances are called nuclear π resonances, as they affect only the nuclear polarisation in the strong field limit. These resonances become weaker and widely spaced for larger holding fields. The electron π resonances (π_{14} and π_{23}) are stronger in a large holding field, and are tightly spaced. The σ resonances affect both electron and nuclear polarisation, are inhibited in a strong field, and for the HERMES target field have a spacing almost identical to the electron π resonances.

Two distinctly different methods have been used to model the depolarisation caused by the pulsed electron beam. The first attempts to track a particle through the cell, finding the holding and HF fields at each step, and thereby calculating a depolarisation probability. After many steps (and many depolarisation calculations), the particle leaves the cell, and the simulation continues with a new particle. Such a simulation was made for HERMES by E. Kinney [Kin91], based on a program written for the VEPP-3 storage ring at Novosibirsk. The advantages of this approach include an adaptability to any field distribution, but its usefulness is limited by long computing times.

An alternative approach was made by H. Kolster [Kol98], who used the well-known triangular form of the density distribution in the cell, together with the measured z-dependence of the holding field to calculate the shape and strength of depolarising resonances for the longitudinal target magnet. Such a model requires the density distribution to be calculated only once, possibly by using a Monte-Carlo simulation. The particle motion can then be treated statistically, and the shape and strength of resonances can quickly be found. The disadvantage with this approach is that certain assumptions and simplifications need to be made. For example, Kolster assumed that resonances only occurred within a given radius from the beam axis, and that within this radius the depolarisation probability was fixed. Whilst this may be reasonable for the longitudinal magnet, this assumption would not apply for certain resonances in the transverse magnet, as will be seen. Graw [Gra98] further developed numerical approximations for beam-induced depolarisation, dealing with the dependence on the radial position, and the point of closest approach in a more realistic manner.

In order to investigate the effect of σ transitions in the transverse target magnet, we must find a model which can make allowance that the resonant region will be at a certain distance from the beam. It must take account of the field inhomogeneity in the x and y directions, and even deal with multiple resonances being present in the cell. Because of this additional complexity, the present simulations were made using a tracking Monte-Carlo program, based on B. Braun's "Monte Carlo Gas Dynamics (McGadyn)" code, which has already been used to model processes in the HERMES target cell. [Bra95]. This program, as we shall see, has a major advantage in speed compared to the program used by Kinney.

4.2 A Model of the Holding Field.

Detailed and precise measurements of the magnetic field have been made using a computer-controlled Hall probe, as described in section 3.4. A simple approximation of these measurements is that B_y is independent of z, and varies parabolically in x and y. A parabolic fit to the measured data was shown in figure 3.13. It is assumed that the components of the holding field B_x and B_z are negligible compared to B_y.

Using this fit, we can then write the holding field *without* the correction coil as

$$B_y = B_0 + k_x x^2 + k_y y^2 \tag{4.9}$$

with $k_x = -0.00534\,\mathrm{mT/mm}^2$ and $k_y = 0.0051\,\mathrm{mT/mm}^2$. As the difference between these two parameters (ignoring the signs) is zero within experimental error, for all further calculations an average value of ± 0.0052 has been taken.

We know that σ_{24} resonances are spaced by 0.37 mT at the working point of the transverse target. This spacing is too small to positively identify which particular harmonic we are dealing with, and the value of B_0 is known also roughly to this level. It is sufficient, however, to know that the resonances are separated by this spacing, and that if there is a resonance at B_y, then there is also a resonance at $B_y + 0.37\,\mathrm{mT}$.

With this knowledge we can plot the positions of a resonance in the storage cell. The shape of a resonance contour is hyperbolic, as shown in figure 4.6. If B_0, the field at the centre of the cell, is increased, for example by increasing the magnet current, then the resonances will move, and eventually further resonances, not shown in figure 4.6, will enter the cell.

4.3 The Monte-Carlo Simulation Program, McGadyn

The program used tracks single particles through a defined structure (such as an elliptical storage cell). After each wall collision, the particle is desorbed with a cosine distribution, and the next collision point is calculated, assuming that the particle moves in a straight line between collisions. As no steps need be calculated between two wall collisions, this program is much faster than the kind used by Kinney, which needed hundreds of intermediate calculations: the computing equivalent of somebody asking "Are we nearly there yet?" every half mile. McGadyn puts the traveller to sleep, and wakes him upon arrival.

The program was modified to include depolarising surfaces, such as those in figure 4.6. Whenever a particle passes through such a surface, the position is noted. To continue the travelling analogy, this is roughly the equivalent of a tannoy announcement "and to your

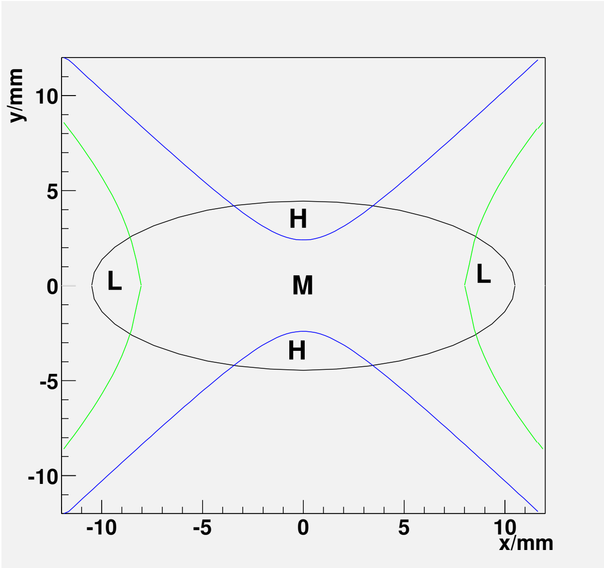

Figure 4.6: The positions of two resonances, separated by 0.37mT, are shown. Inside the cell, the field can either be described as (H)igh if above the upper (blue) resonance, (L)ow if below the green resonance, and (M)edium if in between the two resonances. If a particle passes from one region to another, then it must pass through the resonant surface, and could experience a spin flip. Resonances which do not enter the cell are not shown.

left you can see the Eiffel tower", upon which our traveller wakes, notes the occurrence, and promptly falls back to sleep. A particle is tracked until it leaves the cell, either through an end of the cell, or through a side tube.

The result of a simulation of a single particle, shown only in the x-y plane, can be seen in figure 4.7. Of course the particle is also moving along the z direction during the time shown. The simulation shown is only valid for a particular value of B_0, in this case such that one resonance is 0.04mT above the on-axis value, and the other resonance 0.34mT below.

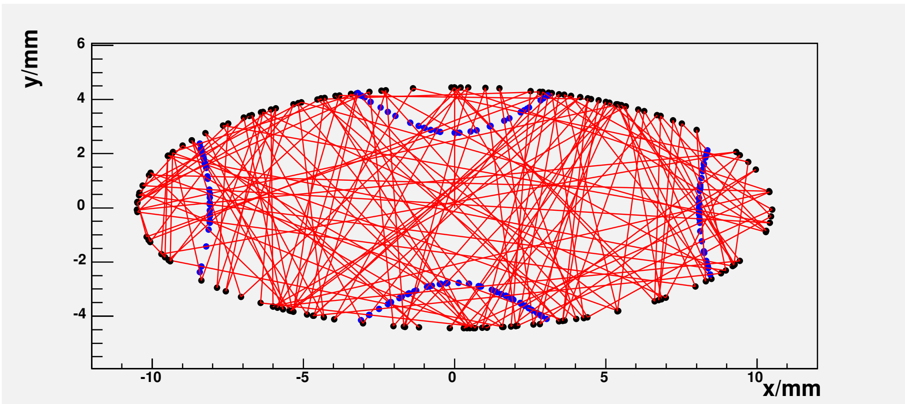

Figure 4.7: Results for one particle in the x-y plane. The elliptical form of the wall collisions (black) contrasts to the depolarising passes (blue). The red lines show the path of the particle between collisions.

4.3.1 The HF Field Components

For the purposes of calculating the HF field, the electron beam is assumed to be circular in cross-section, with a radius of 0.15mm.

Thus the field rises linearly inside the beam, and diminishes with $\frac{1}{r}$ outside the beam. A more realistic field map, taking into account the elliptical shape of the beam can be found in [Reg99](p.55). Depending on whether the spin-flip is caused by a π or σ resonance, the relevant HF field component to be considered is either perpendicular (π) or parallel (σ) to the external holding field. This is shown in figure 4.8. Thus

$$\begin{aligned} B_{\perp} &= |\mathbf{B}_{\mathrm{HF}}| \sin \boldsymbol{\Theta} \\ B_{\|} &= |\mathbf{B}_{\mathrm{HF}}| \cos \boldsymbol{\Theta} \end{aligned} \tag{4.10}$$

where Θ is the angle defined in figure 4.8. When a particle hits a depolarising surface, the relevant field component is calculated using equation 4.10

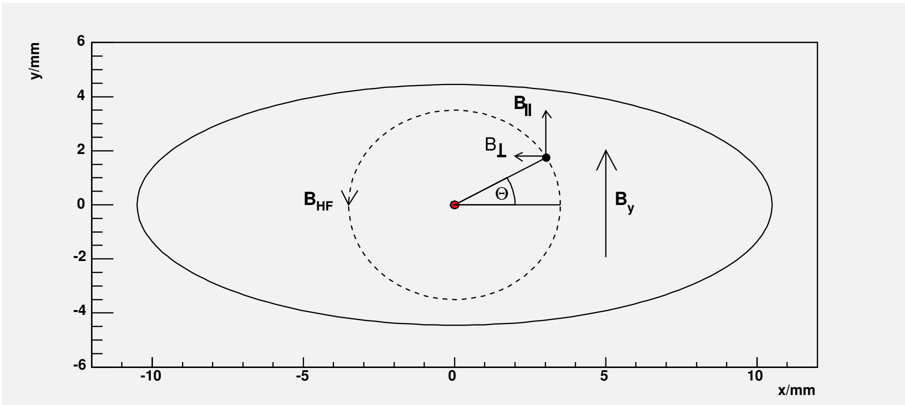

Figure 4.8: Cross section of the cell showing the external field, B_y, and the field induced by the electron beam, B_{HF}. The depolarisation probability is then proportional to the square of either the parallel or perpendicular component of this field.

4.3.2 Calculation of Depolarising Probability

For each particle, at each passage, n, of a depolarising surface, the probability of a spin-flip is calculated using the matrix 2.52. This gives the equations

$$P_n^{\sigma} = \sin^2(2\theta)\left(\frac{\mu_B}{2\hbar}\right)^2 B_{\|}^2 \tau^2 \tag{4.11}$$

for a σ_{24} resonance and

$$P_n^{\pi} = \cos^2(\theta)\left(\frac{\mu_B}{2\hbar}\right)^2 B_{\perp}^2 \tau^2 \tag{4.12}$$

for an electron π resonance, where θ is the mixing angle, given by $\tan(2\theta) = B_c/B_y$, and where the HF field component $B_{\|,\perp}$ refers to the strength of the relevant Fourier harmonic.

τ is given by the equation

$$\tau^2 = \frac{\pi}{\frac{\partial \omega}{\partial B_y}\left(\frac{\partial B_y}{\partial x} v_x + \frac{\partial B_y}{\partial y} v_y + \frac{\partial B_y}{\partial z} v_z\right)} \tag{4.13}$$

and not by equation 4.7 for reasons explained in Appendix A. The two equations differ by a factor of two, which is not important in understanding the principle of depolarising resonances, but is needed for an accurate quantatitive description.

If a particle happens to coincide with a depolarising surface exactly tangentially, then the interaction time, as calculated by equation 4.13 will approach infinity. This is not a real effect, and occurs because this equation ignores the curvature of the depolarising surface, and does not even consider the limited dimensions of the storage cell. To prevent a very small number of unrealistically large interaction times influencing the simulation, the program limits any times calculated to be above 2.5 μs to this time.

For the case of the σ_{24} transition, the depolarisation is small enough that the individual probabilities can simply be summed to give the total depolarisation probability for one particle. By then averaging over all particles, the result is obtained. Because of the dependence on θ, the electron π resonances are roughly 30 times more likely than the σ resonance, and can reach values where saturation effects become important. Thus the probability for a single particle is defined as

$$P = 1 - \exp\left(-\sum_n P_n\right) \tag{4.14}$$

and for the final result an average is made over all particles.

4.4 Results of the Simulation

The Monte-Carlo simulation can only be used for electron π resonances and σ resonances as they occur every 0.37 mT (see table 4.2). Nuclear π resonances will be dealt with in section 4.5

4.4.1 Results for the Hyperbolic Field Model

For a complete picture of the effects of the depolarising resonances, it is necessary to look at a complete cycle, achieved by varying B_0 over a range of 0.37mT. Typically 100-200 atoms are taken for each value of B_0, and B_0 is increased in steps of 0.005mT. Such a simulation takes around 10 minutes on a 1.8 GHz computer. For each value of B_0 an average depolarisation probability for all atoms is calculated. Additionally, the number of passes through depolarising surfaces and the number of wall collisions are recorded. It is possible to differentiate between atoms which have exited through the open ends of the cell, and those which have exited through the sampling tube in the centre of the cell.

Figure 4.9 shows the calculated depolarisation probability for the cases of a π and a σ resonance. The respective tails in the two plots can be seen as the approach of a resonance from the top/bottom of the cell (in the top plot) and the disappearance of the resonance to the sides of the cell (longer tail in the bottom plot). This is confirmed by figure 4.8, which shows that the π resonance is favoured for $y > x$, and that the σ resonance is favoured for $x > y$. The longer tail of the σ resonance can be explained by the elliptical shape of the target cell. At no point is the cell completely free of resonances, at most two resonances contribute to the depolarisation. The plot for the π resonance shows strong signs of saturation.

4.4.2 Introducing a z Field Dependence

Until now, it has been assumed that the magnetic holding field is independent of the z coordinate. This is not strictly true, and a more accurate model of the Through an exhaustive iterative shimming process, the z homogeneity has been optimised, as shown in figure 4.10. As there is no obvious form to the deviation from perfect homogeneity, a useful approximation is to assume that the field varies linearly over the length of the cell in z. Thus the holding field can be described as (compare with equation 4.9)

$$B_y = B_0 + k_x x^2 + k_y y^2 + k_z z \tag{4.15}$$

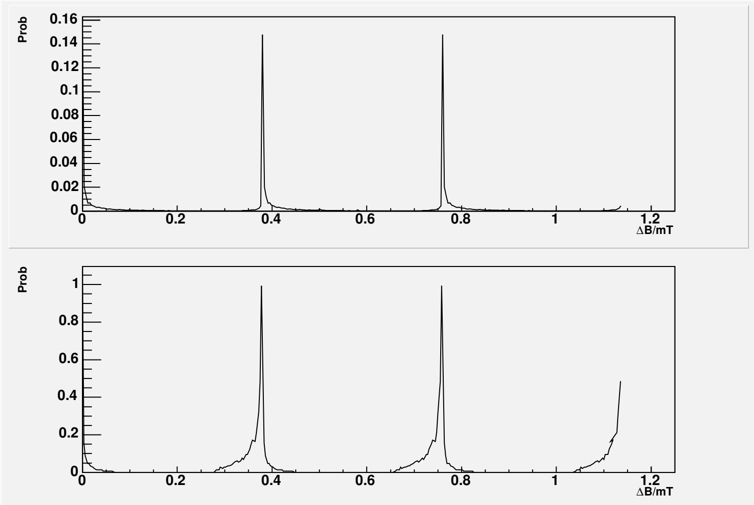

Figure 4.9: The depolarisation probability is shown as the magnetic field is increased. The probability is the average of all particles. Top: probability of a σ resonance, bottom: of an electron π resonance. Only a range of 0.37mT was simulated, this period has simply been repeated to widen the plot.

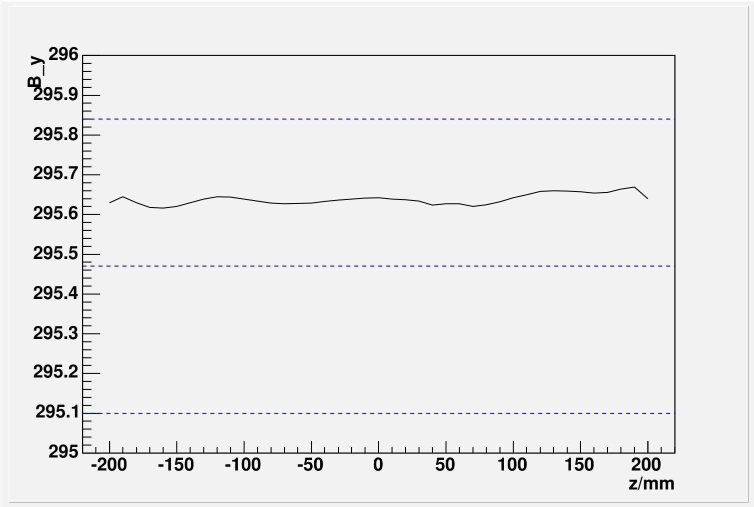

Figure 4.10: The measured field along the z axis. The dashed lines show the separation of σ resonances.

with k_x and k_y as before, and $k_z = 0.0002\,\mathrm{mT/mm}$. This gives a maximal contribution of $\pm 0.04\,\mathrm{mT}$ to the field. Although in reality the measured field varies in a roughly "Zig-Zag" fashion along the z axis, the linear approximation was found to give almost identical results to a zig-zag modulated z dependence. The effect of this additional z dependence is to smear the positions at which the resonance occurs. This is shown in figure 4.11, which is to be compared to 4.7. This smearing is also apparent in the simulation results, shown in figure 4.12. The previously narrow peaks from figure 4.9 have now been broadened, the resonances move towards a Gaussian shape, and it becomes noticeable for the σ resonances that there is a non-zero depolarisation probability even for the best setting of the holding field.

4.4.3 The Case of an Off-Centre Beam

The target cell is designed to allow a certain tolerance regarding the position of the electron beam. As the density of the target is not dependent on the x or y position, the only real consideration is that the beam does not interfere unduly with the cell walls, or any of the collimators in place to protect the cell. Thus deviations of a couple of millimetres are commonplace. Indeed, when the transverse magnet, together with its correction magnets, is turned on, the electron beam is shifted by roughly 2 mm in the x-direction. The complete path of the electrons in this case is shown in figure 4.13. Indeed, the x position of the beam inside the target cell can be seen to vary as the beam is bent by the target

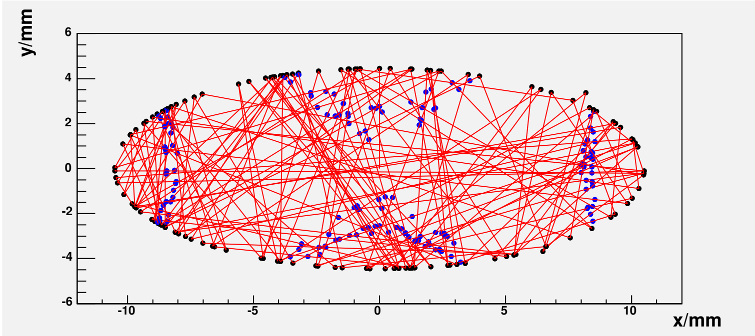

Figure 4.11: After introduction of a linear z dependence, the hyperbola in the $x - y$ plane are no longer so clearly defined.

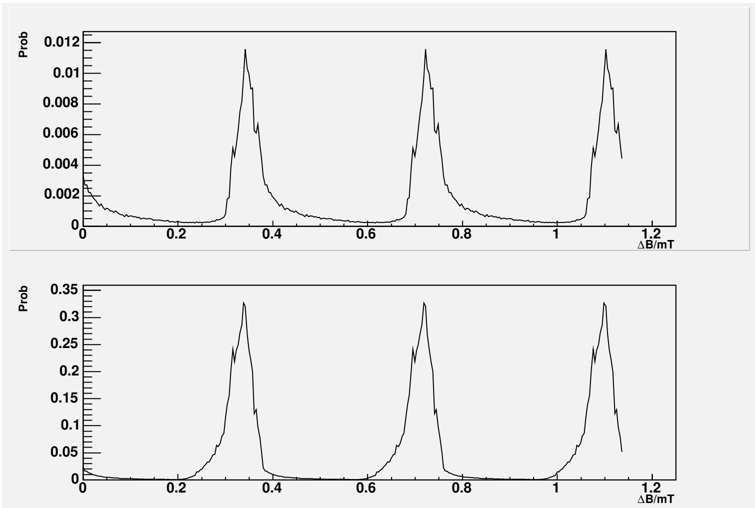

Figure 4.12: The depolarisation probability is shown as a function of the holding field, taking into account also a z field dependence. Compare to figure 4.9, but note the change in y-scale. The pi resonance is no longer completely saturated.

magnet. This very slight effect can, however, be neglected, as it is unimportant compared to the inhomogeneities in the holding field considered so far. Shifting the electron beam by 2 mm, however, produces an interesting effect in the simulation, as shown in figure 4.14. There is no density dependence of the x-y position, which leaves two counteracting effects of moving the beam axis. Both result from the fact that the field gradient is at a minimum in the centre of the cell.

Firstly, because of the low field gradient, τ (equation 4.7) is at a maximum in the centre of the cell. Moving the beam axis, and thereby the location where depolarising effects are strongest away from the centre of the cell will result in τ being shorter close to the beam, and a lower probability of a spin-flip.

The second effect, which increases the spin-flip probability, is that the field gradient is higher away from the centre of the cell. Thus if a depolarising surface crosses the x axis at $x = 0$ for an initial field $\Delta B = 0$, the field must be increased by 0.021 mT to move the resonance so that it crosses the x axis at $x = 2$ mm, a further 0.062 mT to increase the x position to 4 mm, and then by a further 0.125 mT so that the resonance reaches 6 mm on the x axis. Thus if the beam is at the centre of the cell, only resonant surfaces corresponding to a field very closely matching the holding field at the centre of the cell

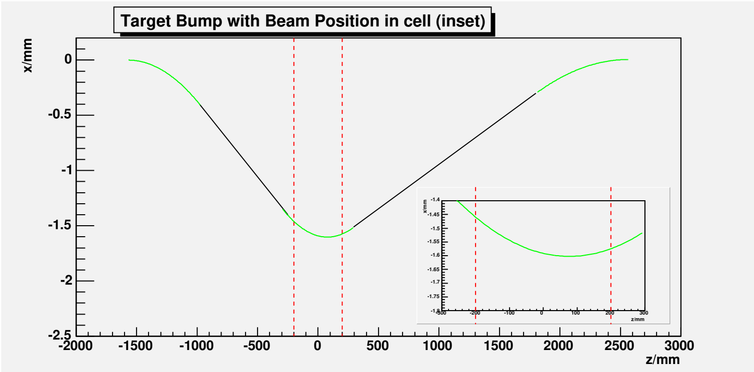

Figure 4.13: The path of the electron beam in the target region of the HERMES experiment with the transverse target magnet. The cell position is shown by dashed lines at ± 200 mm. The beam is deflected by the target magnet (centre) and two correction dipole magnets (left and right).

will experience the strong HF field which exists within 2 mm of the beam. If, however, the beam is off-centre, then resonant surfaces at a field which deviates more from the field at the beam position will still be spatially close to the beam, and will still experience the strong HF field which exists there. A similar effect can be seen for y movement of the beam.

For a beam displacement of 2 mm, the overall effect is a broadening of the peak, and a slight increase in depolarisation probability. The symmetry of the peak also increases.

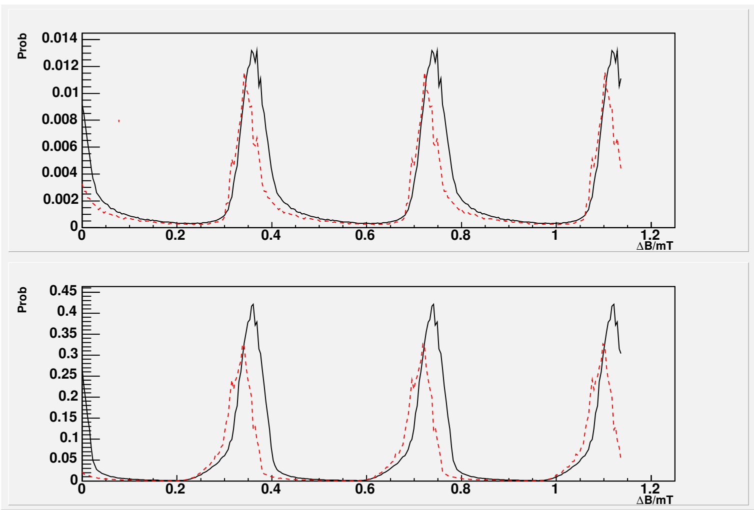

Figure 4.14: Simulations for electron beam off-centre by 2 mm (solid line) and for on-centre (dashed line). Compare with figure 4.12.

4.4.4 Sampling Corrections

Atoms can exit the target cell through either the open ends of the cell, or through the ABS injection tube or BRP sampling tube. Thus the polarisation as measured by the BRP does not necessarily reflect the average polarisation in the cell, which is one of the vital quantities needed to calculate spin-dependent asymmetries at HERMES. A comparison between sampled and average beam-induced depolarisation can be found using the Monte-Carlo program, and the polarisation of the sample measured by the BRP can then be converted to an average polarisation as seen by the beam. [Bau02b, Hen98, Bau00]

Figure 4.15 shows the relation between the depolarisation probability for sampled particles, together with the total probability for all particles. The beam-induced depolar-

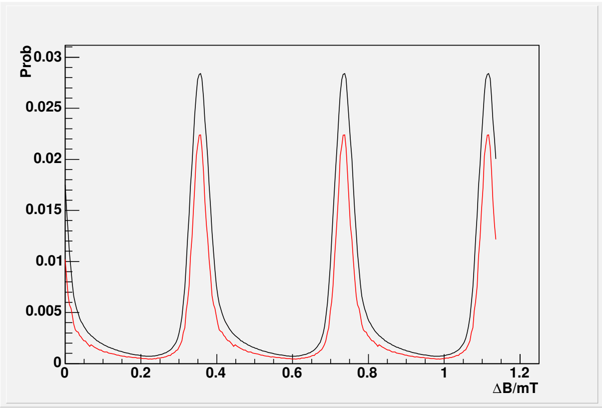

Figure 4.15: The red line (sampled particles) is lower than the average for all particles. This is an effect of the average time spent in the storage cell. An x offset of 2 mm, and y offset of 1 mm was used here to simulate the σ_{24} resonance.

isation occurs only in the beam tube (and not in the sample or extension tubes), and is only very slightly dependent on the z position. The homogeneous beam tube scenario, as detailed in [Bau00] is then the correct description to connect the polarisation measured by the BRP to the average polarisation in the target cell as seen by the HERA beam.

4.4.5 Effect of the Cell Correction coil

In order to improve the homogeneity of B_y in the x direction, an additional coil was added to the target cell, as described in section 3.4.1.

As the additional field can be approximated by a constant field plus a field with x^2 dependence, the total field can be written still as in equation 4.15, but with a modified k_x resulting in the addition of the cell-coil parabola to the original parabola from figure 3.13, so that k_x becomes 0.0008 mT/mm^2. Performing the simulation again, with this much improved x homogeneity, gives the results shown in figure 4.16.

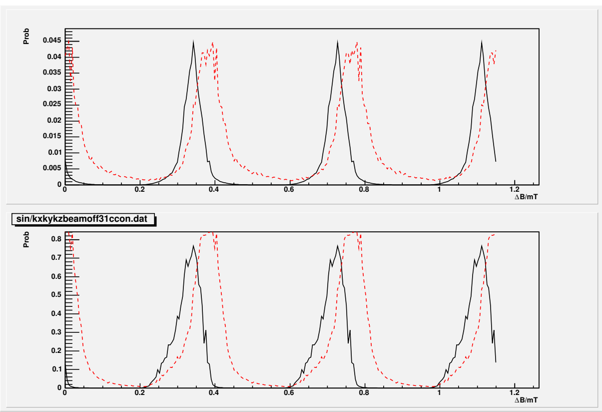

Figure 4.16: The depolarisation probability is compared for cell coil turned on (solid line) to turned off (dashed line). It can be seen that the depolarisation probability for a field setting directly halfway between two resonances has dropped to zero, and that the resonance peaks have become narrower.

4.4.6 Limiting Case of Very Inhomogeneous Fields

The target at HERMES is a very mature apparatus, and is run by some very careful and conscientious scientists, some of whom cared to take time in designing a magnet which is homogeneous to one part in 1000 over a considerable spacial region. The running times of the experiment (which now spans two millennia) also allow such painstaking work to be made, and these efforts have helped to maximise the figure of merit, and to minimise the systematic errors arising from the effects of depolarising resonances.

It is perceivable that circumstances (temporal, spacial or financial) could dictate that in other experiments it would not be possible to design and build such a homogeneous magnet. At this point an optimist would grasp equations 4.11 and 4.13, and conclude that if there are many resonances in the cell, then this will not be any worse than if there is just one, for the number of resonances present in the cell are obviously proportional to the field gradient (one resonance for every 0.37mT), and the transition probability for a single resonance given by these two equations is proportional to the inverse of the field gradient.

We can test this scenario by running the simulation with larger values of k_x, k_y and k_z to simulate a field which varies much more strongly. There will then be more resonant surfaces inside the cell, so the simulation takes somewhat longer. An example of this is shown in figure 4.17, in which $k_x = -0.025\,\mathrm{mT/mm}^2$ and $k_y = 0.025\,\mathrm{mT/mm}^2$. Results

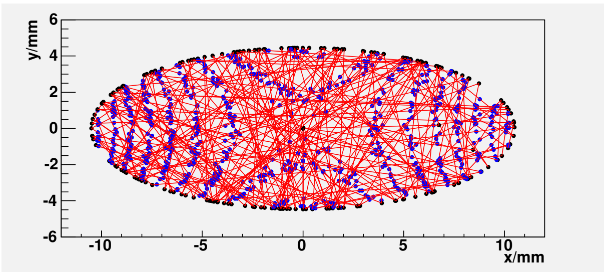

Figure 4.17: The field homogeneity in this hypothetical scenario is so poor that many resonances exist inside the cell. An atom crossing the cell will pass through multiple resonances.

from the simulation for very inhomogeneous fields reveal that the depolarisation is not greatly more than for the case that one or two resonances are present. There is a slight increase, as for many resonances there is always one close to the beam, which experiences very strong transient fields. A short summary of this section would be: the best case is a

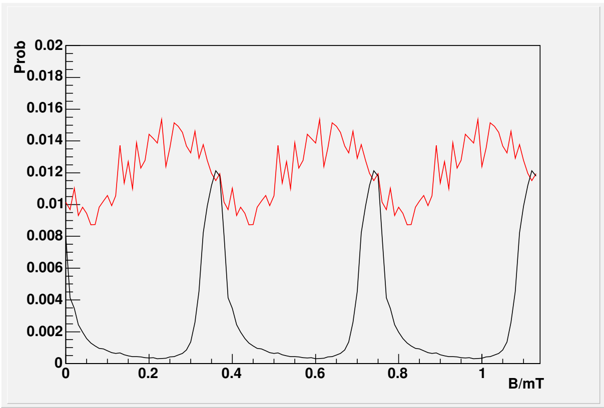

Figure 4.18: The transition probability plotted against holding field for the highly inhomogeneous field described in figure 4.17 (red line) is higher than for the simulation for the present HERMES field distribution(black line), and there is no "safe position" between resonances.

flat magnetic field with no resonances at all, the worst case is a flat magnetic field with one resonance just next to the beam, and having n resonances in the cell is by no means n times worse than having just the one.

4.5 The Nuclear π Resonances

It was shown in section 4.1.2 that for the nuclear π resonances the resonance condition was fulfilled over a large spacial region, so that an atom crossing the cell would experience the resonance for the whole duration. The crucial factor is then how close the atom approaches the beam. To begin with we consider the case of an atom in the longitudinal magnet where the RF field is always perpendicular to the holding field. For simplicity, we assume also that the cell is circular. These two conditions create circular symmetry for the cell crossing, so that all desorptions can be treated identically. Instead of using the HERMES coordinates system, $[x, y, z]$, it is helpful to define a new system $[x', y', z']$, with the y' axis defined to be along the path of the atom. The z' axis is identical to the z axis, which is aligned along the axis of the electron beam. At the point $-y'_0$ the atom is known

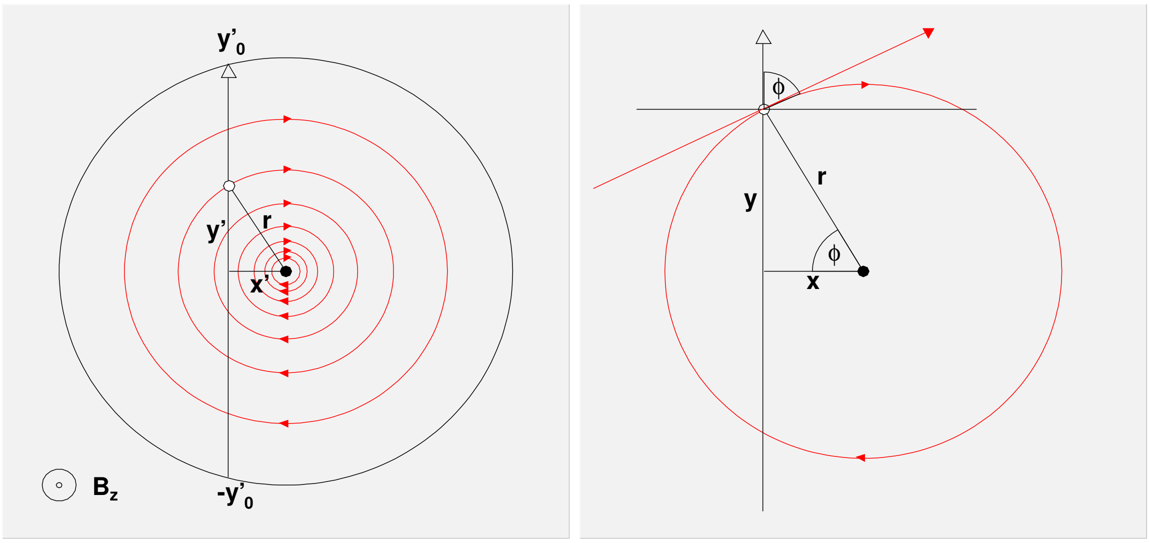

Figure 4.19: Left: The cross-section of a circular cell, showing the RF field lines (red) and the coordinates to be used. x' is the minimum distance of the atom from the beam. Right: The definition of the angle ϕ

to be in the state a. The frequency of the RF field, ω is chosen so that it approximately matches the resonance frequency between state a and state b, ω_{ab}. In section 2.2.3 we used first-order time-dependent perturbation theory to find the transition probability for a sinusoidal field. We made an important assumption, namely that the field could be described as

$$B_x = B_0 \cos(\omega t) \tag{4.16}$$

where B_0 is a constant. We see from figure 4.19 that this is no longer the case. The RF field changes not just sinusoidally with time, but with position in the cell. In other words, B_0 is a function of time, too! This means that when we calculate the integral to find the transition probability we must also include B_0 in the integral.

A π transition can be caused by the perturbing Hamiltonian $H_{ab}(t)$, so the integral which must be found is

$$c(y'_0) = \frac{1}{i\hbar} \int_{t|y'=-y'_0}^{t|y'=y'_0} \exp\left(i\omega_{ab}t\right) H_{ab}(t)\, dt \tag{4.17}$$

and taking the disturbing Hamiltonian from equation 2.41 and considering both the x' and y' components of the RF field we find

$$c(y'_0) = \frac{g_s \mu_B \sin\theta}{2i\hbar} \int_{t|y'=-y'_0}^{t|y'=y'_0} \exp\left(i\omega_{ab}t\right) \left(B'_x + iB'_y\right) \cos\omega t\, dt. \tag{4.18}$$

where $\sin\theta$ is the correct matrix element for nuclear π transitions. We have already established that B'_x and B'_y depend on the position in the cell, and therefore on t. If we express them in terms of the angle ϕ, as defined in figure 4.19 then we have

$$B'_x = \tfrac{\mu_0 I}{2\pi r}\sin\phi \qquad B'_y = \tfrac{\mu_0 I}{2\pi r}\cos\phi \tag{4.19}$$

and the angle ϕ is connected to the x' and y' coordinates by

$$\sin\phi = \tfrac{y'}{r} \qquad \cos\phi = \tfrac{x'}{r}. \tag{4.20}$$

We can then write the total perturbing field as

$$B'_x + iB'_y = \frac{\mu_0 I}{2\pi r^2}(y' + ix') \tag{4.21}$$

Using the Pythagorean relation $r^2 = x'^2 + y'^2$ and introducing the substitution $u = \frac{y'}{x'}$ we find that

$$B'_x + iB'_y = \frac{\mu_0 I}{2\pi}\frac{1}{x'}\frac{u+i}{1+u^2} \tag{4.22}$$

This can be substituted into the integral from equation 4.18, which then becomes

$$c(y'_0) = \frac{g_s\mu_B\sin\theta}{i\hbar}\frac{\mu_0 I}{4\pi}\int_{t|y'=-y'_0}^{t|y'=y'_0}\exp\left(i\omega_{ab}t\right)\left(\frac{1}{x'}\frac{u+i}{1+u^2}\right)\cos\omega t\,dt. \tag{4.23}$$

At this point we make another substitution, namely that $t = \frac{y'}{v_{y'}}$ where $v_{y'}$ is the velocity of the atom. Remembering that $u = \frac{y'}{x'}$ we find

$$dt = \frac{1}{v_{y'}}dy' = \frac{x'}{v_{y'}}du. \tag{4.24}$$

We can now change to an integral over the dimensionless quantity u:

$$c(y'_0) = \frac{g_s\mu_B\sin\theta}{i\hbar}\frac{\mu_0 I}{4\pi v_{y'}}\int_{-y'_0/x'}^{y'_0/x'}\exp\left(i\omega_{ab}\frac{x'}{v_{y'}}u\right)\left(\frac{u+i}{1+u^2}\right)\cos\left(\omega\frac{x'}{v_{y'}}u\right)\,du. \tag{4.25}$$

We can then follow the standard approach of splitting the cos term into two exponential terms, one of which is responsible for spontaneous emission, and the other for absorption of a photon. As we are only interested in the latter we get

$$c(y'_0) = \frac{g_s\mu_B\sin\theta}{i\hbar}\frac{\mu_0 I}{8\pi v_{y'}}\int_{-y'_0/x'}^{y'_0/x'}\exp\left(i(\omega_{ab}-\omega)\frac{x'}{v_{y'}}u\right)\left(\frac{u+i}{1+u^2}\right)\,du. \tag{4.26}$$

Squaring this expression then gives the transition probability for a single crossing with a distance of closest approach x'.

4.5.1 Case of Perfect Resonance

If ω_{ab} is exactly equal to ω then the exponential term in equation 4.26 will be 1, and the integral simplifies to

$$c(y'_0) = \frac{g_s\mu_B\sin\theta}{i\hbar}\frac{\mu_0 I}{8\pi v_{y'}}\int_{-y'_0/x'}^{y'_0/x'}\left(\frac{u}{1+u^2}+\frac{i}{1+u^2}\right)\,du. \tag{4.27}$$

The especially interesting result here is that the first term of the integrand is odd with respect to u. This means that the integral of this term must be zero! If we follow the derivation back to find the meaning of the two terms of the integrand, we find that the first term refers to the x' component of the field, and the second to the y' component. This means that we have shown that for perfect resonance, the x' component of the field cannot cause a transition![1] If we look at the field lines from figure 4.19 we can immediately see the antisymmetry of the x' field with respect to u. For negative y' it points in one direction, and for positive y' in the other. The integral over the x' field is zero, and only the y' component of the RF field can cause a transition, which can be integrated to find:

$$c(_0') = \frac{g_s \mu_B \sin\theta}{i\hbar} \frac{\mu_0 I}{8\pi v_{y'}} \left[2 \arctan\left(\frac{y_0'}{x'} \right) \right] \tag{4.28}$$

The result of this integral depends on x', and it is therefore desirable to integrate over all x' values. If we wish to do this, then it is useful to introduce a new angle ξ, which is the angle from the normal vector to the surface of the cell. We can then average over the well known cosine desorption angle, ξ, instead of the minimum distance, x'. In fact, this change of coordinates is not strictly necessary, and we could integrate over x', for the probability of a distant of closest approach in the range $x' + dx'$ is independent of x' (see Appendix C). However, the change to ξ does simplify the following mathematics.

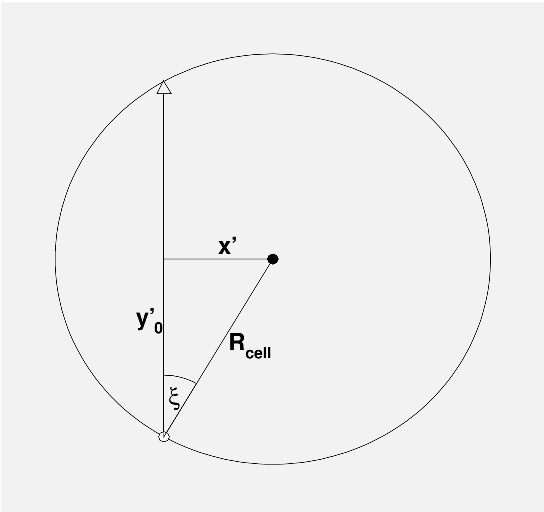

Figure 4.20: The desorption angle, ξ, is shown, together with the corresponding minimum distance to the beam, x'.

ξ and x' are related by the equation

$$\tan(\xi) = \frac{x'}{y_0'} \tag{4.29}$$

and we can insert this into equation 4.28, and use the identity $\arctan(\frac{1}{\tan\xi}) = \frac{\pi}{2} - \xi$ to find that

$$c(\xi) = \frac{g_s \mu_B \sin\theta}{i\hbar} \frac{\mu_0 I}{8\pi v_{y'}} [\pi - 2|\xi|] \tag{4.30}$$

The average transition probability can then be found by squaring this expression, and modulating with the cosine desorption distribution, which is normalised if we used the limits from zero to $\pi/2$.

$$P_{\text{ave}} = \int_0^{\frac{\pi}{2}} \left| c(\xi)^2 \right| \cos(\xi)\, d\xi \tag{4.31}$$

[1] This is not true for the specific case $x' = 0$, where the limits of the integral go to infinity, leading to what Graw [Gra98] showed to be a finite integral. For all non-zero x' values, however, the statement holds.

Integrating by parts, we find

$$P_{\text{ave}} = \frac{g_s^2 \mu_B^2 \sin^2\theta}{\hbar^2} \frac{\mu_0^2 I^2}{64\pi^2 v_{y'}^2} [4\pi - 8] \tag{4.32}$$

This average transition probability for one crossing of the cell can then be multiplied by the number of cell crossings in the resonant region to find a total probability. If the resonant region extends along the whole length of the cell then this calculation will be easy. If the resonant region is restricted to a short length, as for the longitudinal magnet then it is necessary to know the density at that z position and the length of the resonant region.

4.5.2 Transverse Holding Field

Until now we have assumed that the holding field is directed along the length of the cell (along z), so that the RF field was always transverse to the holding field. If the holding field is transverse to the cell axis, then the RF field will have components parallel and perpendicular to the holding field, and only the latter can cause a π transition.

In general, the trajectory of the atom (the y' axis) will be rotated by an angle ψ from the axis of the holding field, which is along y. The field component in direction y' can only cause a transition through its perpendicular part, $y' \sin\psi$, and the field component in the direction x' through its perpendicular component, $B_{x'} \cos\psi$. Through averaging the transition probability around all possible trajectories, we will then average over either $\cos^2\psi$ or $\sin^2\psi$ around the cell, which will result in a factor 2 lower probability than for the longitudinal case.

We can then use equation 4.32 to find the total transition probability for an atom in the cell with the transverse magnet, assuming that the probability does not depend on the z coordinate.

$$\begin{aligned} P_{\text{tot}} &= N_{\text{coll}} \cdot P_{\text{ave}} \\ &= \frac{1}{2} N_{\text{coll}} \cdot \frac{g_s^2 \mu_B^2 \sin^2\theta}{\hbar^2} \frac{\mu_0^2 I^2}{64\pi^2 v_{y'}^2} [4\pi - 8] \end{aligned} \tag{4.33}$$

The velocity in the y' direction $v_{y'}$ is given by the sum of the x and y velocities:

$$v_{y'} = \sqrt{\frac{2k_B T}{m_p}} \tag{4.34}$$

which for a cell temperature of 100 K gives a velocity of 1290 m/s. The square of the matrix element $\sin^2\theta$ is equal to 0.0071 for a holding field of 297 mT, and the transition probability is then given by

$$P_{\text{tot}} = 1 - \exp\left(-N_{\text{coll}} \cdot 0.0027\right) \tag{4.35}$$

which for 300 wall collisions gives a transition probability of 55%.

4.5.3 Off-Resonance Depolarisation

A complete description of nuclear π resonances must also consider the case that the resonant frequency, ω_{ab}, does not exactly match the frequency of the RF field, ω. It is no longer sufficient, as was the case for the σ resonances, that the resonance will be exactly fulfilled somewhere in the cell. Now the whole cell experiences the same difference between applied and required frequencies $\Delta\omega$, and we must find the strength of the resonance as a function of $\Delta\omega$.

In this case we must return to equation 4.26 and allow the exponential term to take values other than 1, which was the result for perfect resonance. By writing the exponential term in trigonometrical functions we get

$$c(y_0') = \frac{g_s \mu_B \sin\theta}{i\hbar} \frac{\mu_0 I}{8\pi v_{y'}} \int_{-y_0'/x'}^{y_0'/x'} \left(\cos\left(\Delta\omega \frac{x'}{v_{y'}} u\right) + i \sin\left(\Delta\omega \frac{x'}{v_{y'}} u\right) \right) \left(\frac{u+i}{1+u^2} \right) du. \quad (4.36)$$

Taking only the terms which are even in u, we find

$$c(y_0') = \frac{g_s \mu_B \sin\theta}{\hbar} \frac{\mu_0 I}{8\pi v_{y'}} \int_{-y_0'/x'}^{y_0'/x'} \frac{1}{1+u^2} \cos\left(\Delta\omega \frac{x'}{v_{y'}} u\right) + \frac{u}{1+u^2} \sin\left(\Delta\omega \frac{x'}{v_{y'}} u\right) du. \quad (4.37)$$

The second (sin) term is odd with respect to x', whilst the first term is even. Thus when squaring this expression to find the transition probability, the interference terms will cancel if we average over all x'.

The averaged transition probability over all x' values is then given by

$$P_{\text{ave}}(\Delta\omega) = \frac{g_s^2 \mu_B^2 \sin^2\theta}{\hbar^2} \frac{\mu_0^2 I^2}{64\pi^2 {v_{y'}}^2 R_{\text{cell}}^2} \int_{-R_{\text{cell}}}^{R_{\text{cell}}} dx' \left(\left| \int_{-y_0'/x'}^{y_0'/x'} \frac{1}{1+u^2} \cos\left(\Delta\omega \frac{x'}{v_{y'}} u\right) du \right|^2 + \left| \int_{-y_0'/x'}^{y_0'/x'} \frac{u}{1+u^2} \sin\left(\Delta\omega \frac{x'}{v_{y'}} u\right) du \right|^2 \right) \quad (4.38)$$

Having written this fine equation, we should take a few seconds to consider what it means: The inner integral over u is an integral along the path of atom as it crosses the cell. The outer integral over x' is to consider all possible trajectories. The cos and sin terms arise from the component of the RF field in the x' and y' directions. It is also important to keep note of the various factors of 2 which have accumulated. We have a factor of 1/2 for the spin, a factor of 1/2 from $B = \frac{\mu_0 I}{2\pi r}$ and a factor of 1/2 from splitting the $\cos \omega t$ field dependence into two exponential terms, one of which was discarded. When squared this gives the 64 in the denominator.

The integrals can be solved numerically, and it is interesting to see the results of this integral for different values of $\Delta\omega$. In order to see the effects of the two integrals over u, it is helpful to see these integrals plotted as a function of x', too. It is then possible to integrate over all x' values to find an average transition probability for a certain value of $\Delta\omega$. We would expect this transition probability to be equal to the value calculated in section 4.5.1 for $\Delta\omega = 0$, and to decrease as the resonant condition is not perfectly fulfilled. An alternative to referring to $\Delta\omega$ is to use the corresponding deviation in holding field, ΔB. The relation between these two quantities can be found in equation 2.64. Note that the width of the resonance in figure 4.22 is considerably larger than the homogeneity of the target holding field, so we should be able to measure such a resonance shape by slowly varying the target field whilst observing the hyperfine state populations of the target gas. Such measurements will be made in chapter 6 and compared with the predicted results here.

It is possible to use figure 4.22 to find the width of the resonance.

$$\text{HWHM} = 0.89\,\text{Mrad/s} \quad (4.39)$$

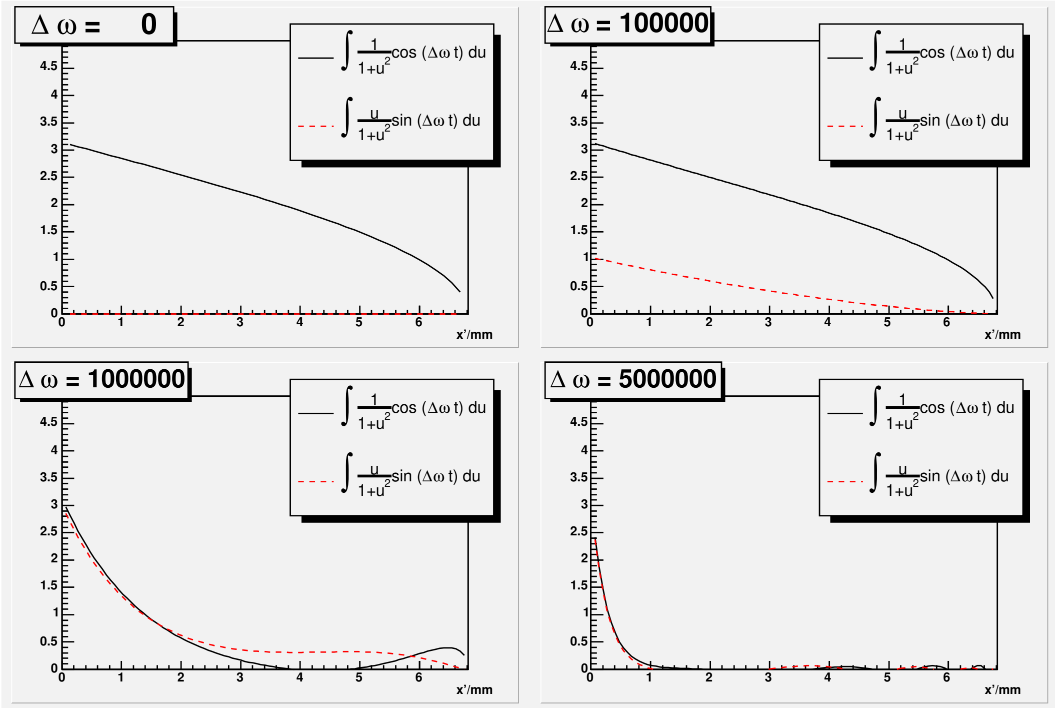

Figure 4.21: The results of the inner integrals from equation 4.38 are shown as a function of x'. For perfect resonance (top left), only the cosine integral is present, the sine integral is zero. As $\Delta\omega$ increases (top right) the sine integral also becomes important, but the cosine integral is soon suppressed (bottom left). For large values of $\Delta\omega$ (bottom right) both integrals are suppressed, particularly for larger x values. $\Delta\omega$ is given in rad/s.

This is comparable with the frequency corresponding to the uncertainty principle resulting from a typical flight time across the cell:

$$\Delta\omega = \frac{2\pi v_y}{R_{\text{cell}}}. \tag{4.40}$$

Taking the radius of the cell to be given by $R_{\text{cell}} = \sqrt{10.45 \cdot 4.45} = 6.82$ mm, and v_y to be as found in section 4.5.1 we find that $\Delta\omega = 1.19$ Mrad/s. This figure can be compared with the frequency separation of harmonics from the HERA ring, which occur every $f_B = 10.4097$ MHz, and it clear that the natural width of the nuclear π resonances will not present a problem, as

$$\begin{aligned} \frac{\Delta\omega}{2\pi f_B} &\simeq \frac{1.19}{2\pi \cdot 10.4097} \\ &\simeq \frac{1}{55} \end{aligned} \tag{4.41}$$

and even allowing for the long tails of the resonance, these resonances can be avoided at HERMES. This calculation can be used to find a condition for resonances which occupy the entire width of the cell being distinguishable:

$$\frac{f_B R_{\text{cell}}}{v_y} > 1 \tag{4.42}$$

although a ratio of 10 or above would be much more satisfactory than the limiting case of 1, where resonances would be distinguishable, but considerable depolarisation could still occur.

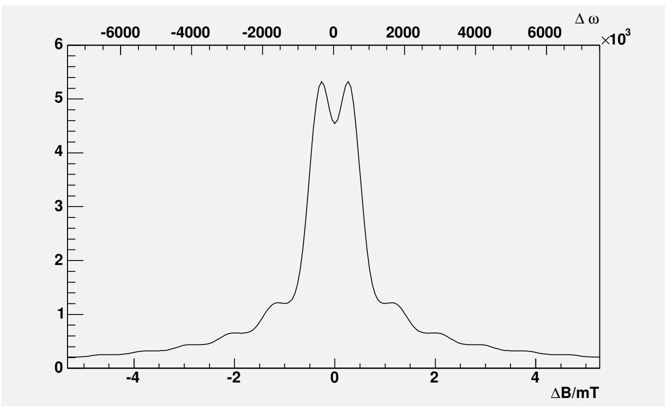

Figure 4.22: The results of the double integrals over u and x, calculated numerically, are shown as a function of $\Delta\omega$ and ΔB. The transition probability can be found by multiplying the result of this integral by the constants in equation 4.38. Note that the value for $\Delta\omega = 0$ is in agreement with equation 4.32. The holding field width ΔB is calculated for a field of 282 mT.

Chapter 5

Effect of the Hera Beam Structure on Depolarising Resonances.

We could run a damned good railway if it wasn't for the bloody passengers.

A British Rail employee[1]

Introduction

A commonly used approximation to calculate the effect of beam-induced depolarisation at HERA is to assume that all 220 buckets of the electron ring are equally filled. The description in 2.3 follows this simplification, which results in a series of harmonics (which will in this chapter be known as *bunch* harmonics) every $f_{\text{bunch}} = 10.4097\,\text{MHz}$, contained within a Gaussian envelope.

The HERA electron beam structure changes from fill to fill, but generally consists of three blocks of buckets which are filled, separated by three gaps, as shown in [Reg03]. The question then arises: Is it really reasonable to ignore the missing bunches, and to approximate that all have the same height?

Measurements showing depolarisation of the HERMES target have been presented in [Ack99]. This paper described the shape of the resonances for Hydrogen in a longitudinal target, and contains the assertion that "The line shape [of a depolarising resonance] depends on the distribution of the bunch intensities in the stored beam". The reference [Kol97] contains a plot, showing the bunch harmonics every f_{bunch} caused by the HERA beam. These harmonics are broadened somewhat at their base. Private correspondence with H. Kolster confirmed that "there is a clear difference between the depolarization resulting from an ideal spectrum of a uniformally filled ring and the actual spectrum."[Kol03].

Unfortunately, no measurements were made to show the difference resonance shape for different fill structures with the longitudinal target, and it is difficult to extract the effect of the non-ideal bunch structure from the final measured and simulated resonance shape. The effect seems to have been minor compared to the density profile inside the cell and the field gradient, which seem to have dominated the resonance shape for the longitudinal target magnet.

This chapter considers the general case of a storage ring with m bunches, each with a current which is Gaussian in shape and has a peak current of I_m. The Fourier transform

[1]As quoted by Murray Walker "*Unless I'm very much mistaken.*"

is calculated for a simple hypothetical ring with eight bunches, and then for the HERA electron ring.

5.1 Fourier Transform for a Sequence of Bunches

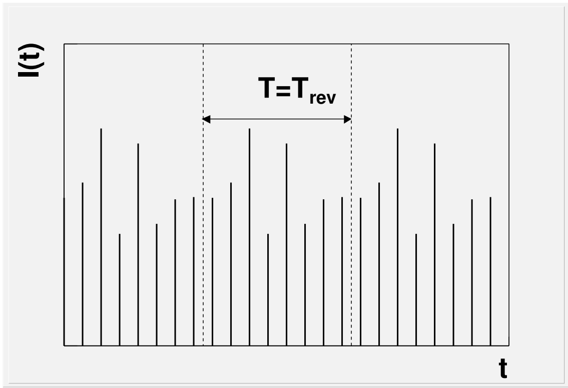

Figure 5.1: A current structure which repeats after eight bunches. T_{rev} is the time needed for a bunch to make one lap of the ring. The Gaussian bunch shape is not shown here.

The case for a storage ring containing m bunches, all with equal current and separated by time T was presented in section 2.3. A more realistic model of any storage ring with m_{bunch} bunches must allow the current to vary from bunch to bunch. This implies that the beam structure repeats itself only after the time, T_{rev} when a single bunch has passed once around the ring, which is m_{bunch} times longer than the average time between two successive bunches. The fundamental frequency for this model is then m_{bunch} times smaller. This principle is illustrated for a storage ring with eight bunches in figure 5.1.

To calculate the amplitudes of the Fourier harmonics for this expanded model, we proceed in the same manner as for one bunch, but with a new fundamental frequency corresponding to $\frac{1}{T_{\text{rev}}}$. If each bunch can be transformed from a central Gaussian as defined in equation 2.57, by a factor I_m/I_0, and a time delay $t+t_m$, then the current can be expressed as

$$I(t) = \sum_{m=1}^{m_{\text{bunch}}} I_m \exp\left(-\alpha\left(t+t_m\right)^2\right). \tag{5.1}$$

where $\alpha = \frac{1}{2\sigma_t^2}$ refers to the length of the bunch. Inserting this current into equation 2.56, and substituting for $t+t_m$ with v we get

$$a_n + ib_n = \frac{2}{T}\int_{-\frac{T}{2}+t_m}^{\frac{T}{2}+t_m} \sum_{m=1}^{m_{\text{bunch}}} I_m \exp\left(-\alpha v^2\right)\exp\left(\frac{2\pi i n(v-t_m)}{T}\right)\,dv \tag{5.2}$$

which can be separated into an integral over v and a sum over each bunch.

$$a_n + ib_n = \frac{2}{T}\sum_{m=1}^{m_{\text{bunch}}} I_m \exp\left(\frac{-2\pi i n t_m}{T}\right)\cdot\int_{-\frac{T}{2}+t_m}^{\frac{T}{2}+t_m} \exp\left(-\alpha v^2\right)\exp\left(\frac{2\pi i n v}{T}\right)\,dv \tag{5.3}$$

For any realistic Gaussian bunch structure, the limits of the integral can again be replaced by $-\infty$ and ∞, which reduces the integral to that in equation 2.58, giving

$$a_n + ib_n = \frac{2}{T}\sqrt{\frac{\pi}{\alpha}} \exp\left(\frac{-\pi^2 n^2}{T^2\alpha}\right) \sum_{m=1}^{m_{\text{bunch}}} I_m \exp\left(\frac{-2\pi i n t_m}{T}\right) \tag{5.4}$$

This solution may be better understood if we assume that all bunches are equally spaced in the storage ring. This means that for a full m_{bunch} bunches, t_m will take the values $-T/2 + T/2m$, $-T/2 + 3T/2m$, $-T/2 + 5T/2m \ldots$, so that

$$t_m = \frac{T}{2}\left(-1 + \frac{2m-1}{m_{\text{bunch}}}\right) \tag{5.5}$$

with m from 1 to m_{bunch}. The last term in equation 5.4 can then be written as

$$\sum_{m=1}^{m_{\text{bunch}}} I_m \exp\left(i\pi n\left(1 - \frac{2m-1}{m_{\text{bunch}}}\right)\right). \tag{5.6}$$

and we can see that we are summing over a phase shift for each bunch. Generally each

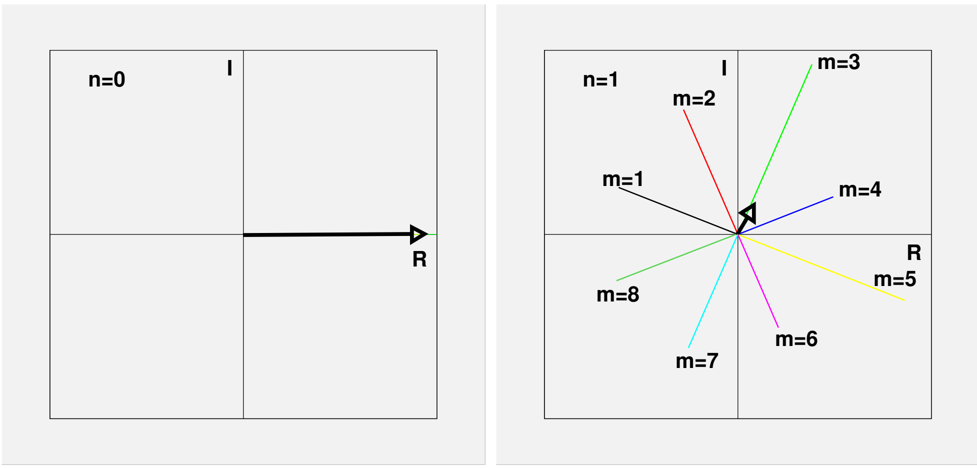

Figure 5.2: Phase diagrams for the harmonics $n = 0$ (left) and $n = 1$ (right) for the eight bunches shown in figure 5.1. The length of each arrow is proportional to the bunch current. For $n = 0$ all bunches are in phase, and the resulting coefficient (large black arrow) is the sum of all bunch currents. For $n = 1$ the bunches are separated by a phase factor of $\pi/4$ and the resulting coefficient is small.

bunch will have a different phase shift, which depends on n (the harmonic number) and m (the bunch number). Summing over all m for a particular n gives the strength of the n_{th} harmonic. Of particular interest are the harmonics where $n = k \cdot m_{bunch}$, where k is an integer. The sum over all bunches will then be

$$\sum_{m=1}^{m_{\text{bunch}}} I_m \exp\left(i\pi k\left(m_{\text{bunch}} - 2m - 1\right)\right). \tag{5.7}$$

for which the exponential term is real and equal (either ± 1) for each and every m, so that all bunches are in phase and the sum is just the total current. Such a case is shown in the left diagram of figure 5.2.

All other harmonics where n is not a multiple of m_{bunch} will be suppressed, as the phase factors will cancel each other out, and in the case that all bunches carry the same current these harmonics will be exactly zero. This is no surprise, as the structure has been reduced to the simple model of one repeated bunch, and we have merely found the harmonics corresponding to the bunch frequency. We shall therefore make the following distinction:

- **Bunch harmonics**: special case that $n = k \cdot m_{\mathrm{bunch}}$, with spacing f_B.
- **Ring harmonics**: the total pattern of harmonics, index n, with spacing f_B/m_{bunch}.

The index for the bunch harmonics, k, is then compatible with the index used in section 2.3. The ring harmonics arise then from differing bunch currents, as shown in the right diagram of figure 5.2 and the further the bunch structure deviates from the ideal picture, the stronger these harmonics between the bunch harmonics will become. The term in

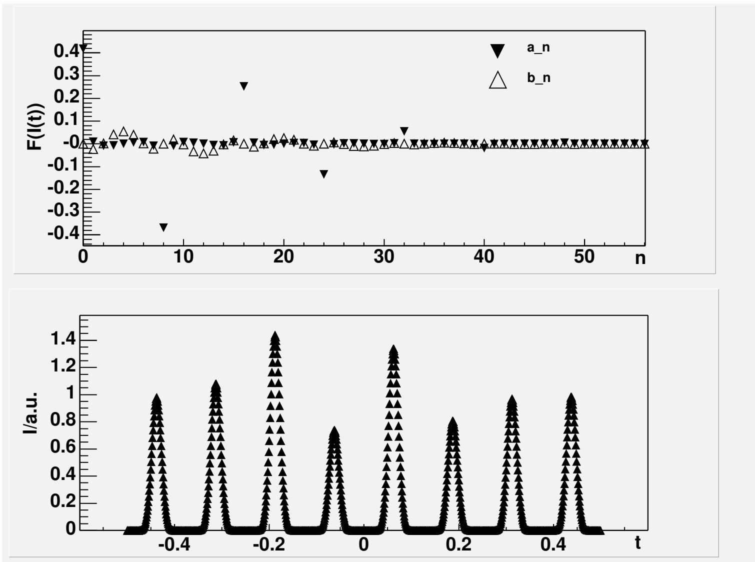

Figure 5.3: The Fourier harmonics (top) for the structure shown in figure 5.1, with Gaussian bunch shapes and $m_{\mathrm{bunch}} = 8$. The reconstructed beam, found by inserting a_n and b_n into equation 2.54 and summing over the first 1000 ring harmonics is also shown (bottom).

equation 5.4 containing $\exp(-n^2)$ produces the familiar envelope for the harmonics. Figure 5.3 shows the ring harmonics for a Gaussian bunch pattern as shown in figure 5.1. In this case the structure repeats after eight bunches, so that the ring harmonics which are multiples of eight ("bunch harmonics") are particularly strong. The Gaussian envelope can also be seen, but due to the long bunches (ie small α), the sequence quickly converges and only the first 50 ring harmonics are of importance.

5.2 Fourier Analysis of the Hera Beam

Using equation 5.4 it is possible to calculate the Fourier harmonics of the stored HERA electron beam. The bunch frequency of the beam , f_{bunch} is roughly 10.4097 MHz, which is 220 times the revolution frequency, f_{rev} of 0.047 MHz. As stated in section 2.3, the width of the Gaussian envelope is around 5 GHz, making a plot of the whole range of $\approx 10^4$ ring harmonics impossible. Fortunately the ring harmonics, as described in equation 5.4, are governed by a cyclical term with a period of 440 ring harmonics. Using evident symmetries, the whole series of harmonics can be described given the width of the

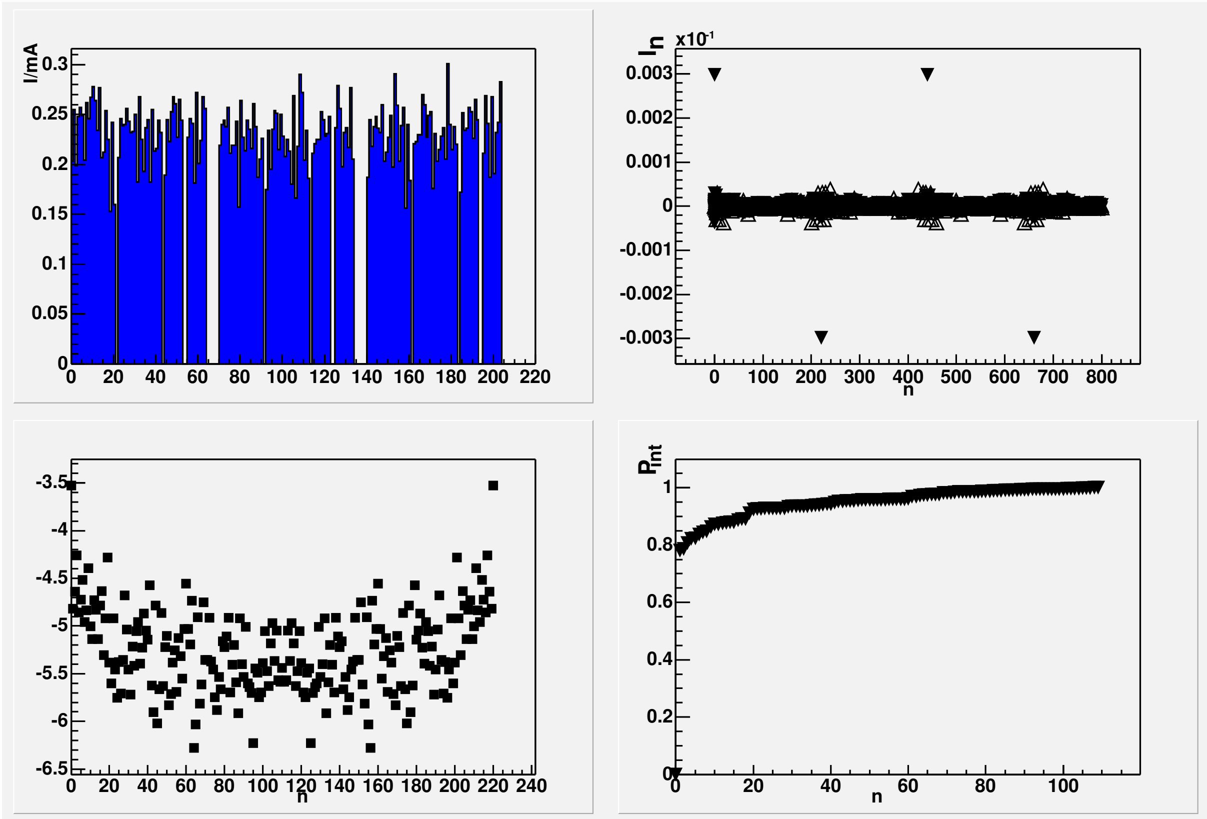

Figure 5.4: Top left: a typical HERA beam structure for a *good fill*, showing the current contained in each bunch. Top right: the amplitudes of the first 880 ring harmonics for this structure, (harmonics 0 and 220 are the first 2 bunch harmonics, and are separated by f_{bunch}). Bottom left: the amplitudes of the first 221 ring harmonics plotted on a logarithmic scale. Bottom right: the normalised integrated power of the harmonics, described in the text.

Gaussian envelope, and the amplitudes of the first 110 ring harmonics. The individual bunch currents of the HERA electron beam are continuously monitored, and the Fourier analysis of a typical bunch structure is shown in figure 5.4. Especially of interest is the last plot, showing the integrated squared sum of the harmonics, which is proportional to the depolarising power of the harmonics. This is defined as

$$P_{int} = \frac{\sum_{i=0}^{n} a_i^2 + b_i^2}{\sum_{i=0}^{110} a_i^2 + b_i^2} \tag{5.8}$$

In this instance, the bunch harmonic (zero in the plot) accounts for 80% of the depolarising power. If the 20 ring harmonics above and below the bunch harmonic are also included, then 95% of the power is accounted for. In contrast, the ring harmonics close to the midpoint between two bunch harmonics are of much reduced importance. This effect can be understood by looking at a phase diagram, such as in figure 5.2. For the harmonic $n = 1$ all bunches are separated from their neighbour in the phase diagram by $2\pi/m_{\mathrm{bunch}}$. Thus neighbouring bunches here will “pull” in almost the same direction. The characteristic of a HERA fill is that it consists of blocks of filled and empty bunches: if a bunch is filled then it is likely that its neighbour is also filled, and if it is empty then its neighbours are also likely to be empty. In figure 5.4 there is an empty block from bunches 205 to 220. For $n = 1$ all 16 empty bunches will act (or more importantly *not* act) in the roughly the same direction. As n is increased, the phase difference between *neighbouring* bunches will increase according to

$$\Delta\phi = 2\pi n / m_{\text{bunch}} \tag{5.9}$$

so that when n rises to 110 (for $m_{\text{bunch}} = 220$) neighbouring bunches will be π out of phase. If we consider a block of 16 bunches, then already after $n = 14$ the phase vectors of the block will be distributed over 2π. The effect of blocks of empty bunches is illustrated in figure 5.5.

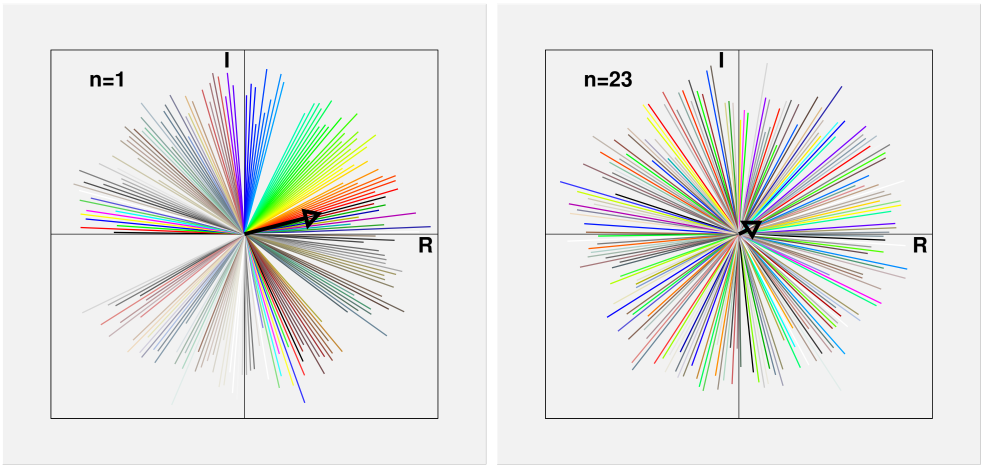

Figure 5.5: The phase diagram for $n = 1$ (left) for a *good fill* at HERA. The 220 bunches are in sequence, starting from $\phi = \pi$ and proceeding clockwise. The large gap from bunches 205 to 220 is largely responsible for the resulting coefficient (large black arrow). For $n = 23$ (right) the order has disappeared, and the resulting coefficient is small.

Of course the particular bunch structure varies from fill to fill, and for some fills the difference is dramatic, as displayed by figure 5.6.

5.3 Predicted Effect on the Nuclear π Resonances

In section 4.5 we predicted a shape for the nuclear π resonances assuming that the target holding field was homogenous throughout the whole cell. The result was a resonance with a width of several mT (for a holding field close to the working point of the target) resulting from the time-energy uncertainty relationship. These predictions were based on the model of a single repeated bunch, as detailed in section 2.3, which led to resonant harmonics spaced by f_{bunch}.

The results of section 4.5 can be transferred directly to the ring harmonics found in section 5.1, but of course the transition probability will be scaled by the strength of the particular harmonic, and each ring harmonic will make only a small contribution. In order to find the total effect of all harmonics it is necessary to convolute the result for a single harmonic (as shown in figure 4.22) with the calculated 220 harmonics (shown, for example, in figure 5.4. The effect of this convolution on the resonance shape is shown in figure 5.7. Note that the resonances produced by the ring harmonics cannot be individually observed according to equation 4.42, even though their magnetic field spacing (0.2mT for the $61_{st}\pi_{12}$ resonance) would allow the target magnet to distinguish between these ring harmonics.

The principle of convolution follows from treating all 220 ring harmonics (including the bunch harmonic) identically, except for a factor proportional to the square of the harmonic. If the bunch harmonic corresponds to an angular frequency $\omega_b = 2\pi k \cdot f_B$, where

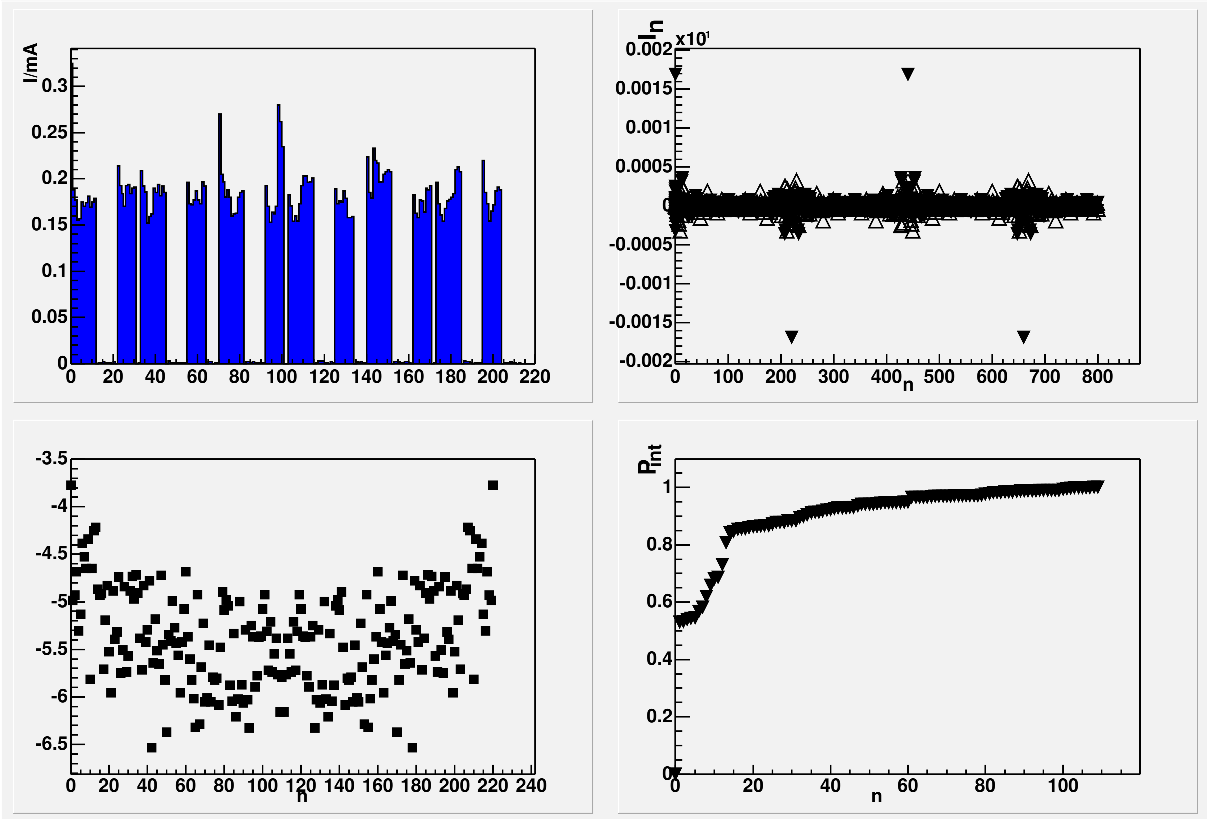

Figure 5.6: Compare with figure 5.4. For this *bad fill* the bunch harmonic no longer dominates the picture (contributing just above 50%), and of special interest are the ring harmonics in the region 1-15 from the bunch harmonic. Together they contribute around 30% of the depolarising power.

k is an integer, then the first ring harmonics after the bunch harmonic will correspond to a frequency of $\omega_b + 2\pi \cdot \frac{1}{220} f_B$, which will produced a resonance with the same shape as the bunch harmonic, but with a much reduced height. All other ring harmonics can be treated in the same way.

5.4 Effect on the σ Resonances

For the transverse target σ_{24} resonances are present, and in the working region of the target occur with bunch resonances every 0.37mT. The bunch structure will lead to exactly the same consequences as for nuclear π resonances, namely un-resolvable ring resonances between the bunch resonances. Whilst the width of the nuclear π resonances is dominated by the time-energy uncertainty relation, for the σ resonances and electron π resonances the field homogeneity determines the resonance shape. As the field homogeneity is only on the limit of being able to resolve between bunch harmonics (which typically contain 80% of the potential depolarising power), the effect of the ring resonances is of secondary importance. Nevertheless, they make the task of completely eliminating σ resonances even more difficult.

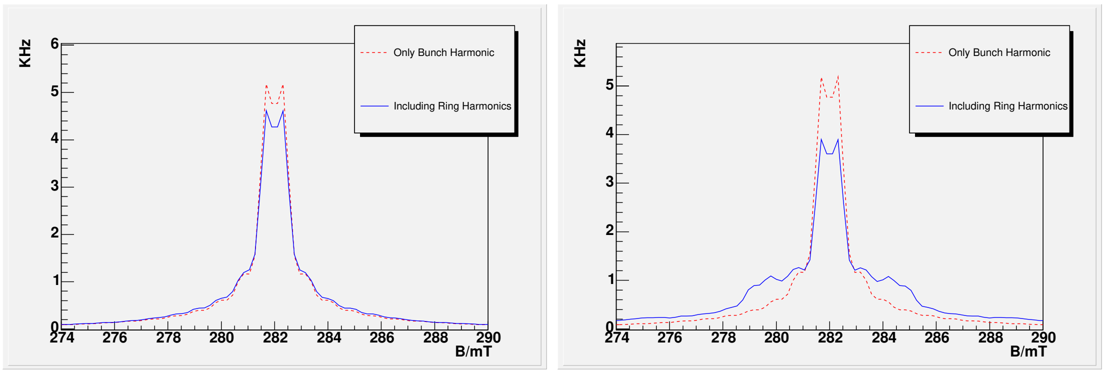

Figure 5.7: Predicted shapes of the π resonances for the *good fill* shown in 5.4 (left) and the *bad fill* from 5.6 (right). For the former, the shape is not affected by the ring harmonics, but for the latter the resonance is considerably widened.

5.5 Conclusions

The particular structure of the HERA beam leads to a "widening" of the bunch resonances. Although ring harmonics exist for all possible holding field values, they are very weak at a point halfway between two bunch harmonics, and will not cause any measurable depolarisation at the working point of the target.

The particular shape of the Fourier transform depends of course on the beam structure, and it is easy to imagine possible fills which could lead to great difficulties for the target polarisation. Figure 5.8 shows the strength of the Fourier harmonics for a fill composed of random currents. There is no longer a "widening" of the bunch harmonic, as for the real HERA fills used so far, but a constant stream of ring resonances. For such a scenario there is no safe field setting in-between bunch harmonics, and the result would be additional depolarisation in the target. Equally disturbing would be irregular fills where particular ring harmonics away from the bunch harmonics are unusually strong. It is therefore important to consider the manner of the filling of a storage ring during the design stage of any experiment using a polarised gas target.

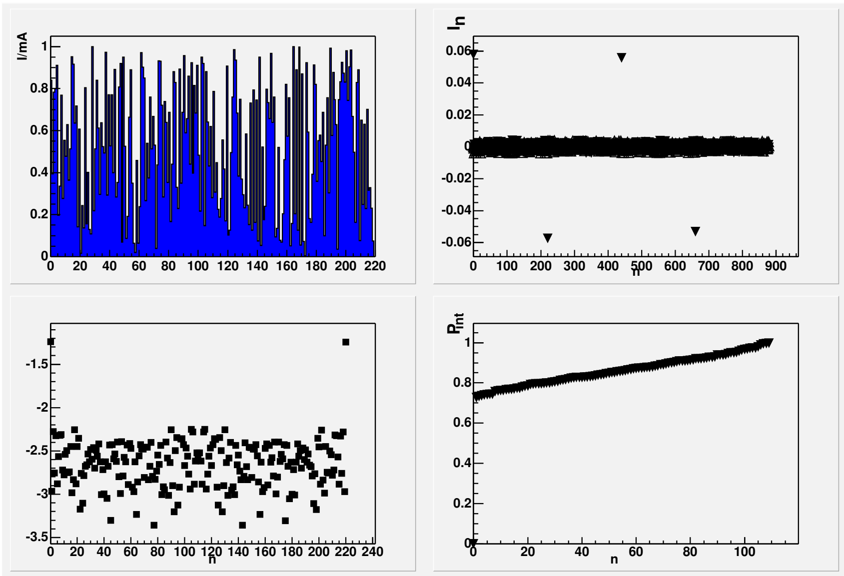

Figure 5.8: The Fourier transform for a ficticious fill, composed of bunches containing random currents. Compare with figure 5.4

Chapter 6

Measurements of the Nuclear π Transitions

Any subject can be made repulsive by presenting it bristling with difficulties

Silvanus P. Thompson

By slowly scanning the holding field of the target, whilst observing the target polarisation with the BRP, it is possible to measure a beam-induced resonance. The important choices to be made are

- Which hyperfine states to inject from the ABS?
- Which hyperfine states should the BRP measure?

Whilst observing a resonance between states $|\,a\,\rangle$ and $|\,b\,\rangle$ it is helpful to inject only one of these two states from the ABS, and observe only one of these states with the BRP. If, for example, we inject state $|\,a\,\rangle$ from the ABS, but only observe state $|\,b\,\rangle$ with the BRP, then the resonance will be visible as an increase in BRP rates. If the BRP only measures state $|\,a\,\rangle$, then the same resonance will cause a drop in BRP rates. Such a measurement is known as a "flip-in" measurement if the resonance is seen as a peak, or "flip-out" if it is seen as a dip. An alternative is to use the BRP in its polarisation measuring mode, in which six pairs of states are measured cyclically.

6.1 Wide Range Flip-In Measurements

A particularly practical method of measuring nuclear π resonances was presented in [Ack99]. States $|\,1\,\rangle$ and $|\,4\,\rangle$ are injected by the ABS, whilst the BRP measures states $|\,2\,\rangle$ and $|\,3\,\rangle$. Either a π_{12} or a π_{34} transition will produce an increase in the measured rates. Of course it is then impossible to tell which resonance is a π_{12} and which a π_{34}, but they can be identified from the resonant holding fields predicted in table 2.1. A measurement as described here is shown in figure 6.1. The peaks can be attributed to the nuclear π resonances, whilst the slow drop in BRP rates with increasing field is caused by the inhibition of spin-exchange collisions at higher holding fields.

It is interesting to see whether the shape of the resonance can be described by the calculations made in section 4.5. The resonances become increasingly wider for higher fields, a direct result of the derivative $\frac{d\omega}{dB}$ (see equation 2.64, which becomes very small for large holding fields. So although all resonances have the same width in $\Delta\omega$, the width ΔB

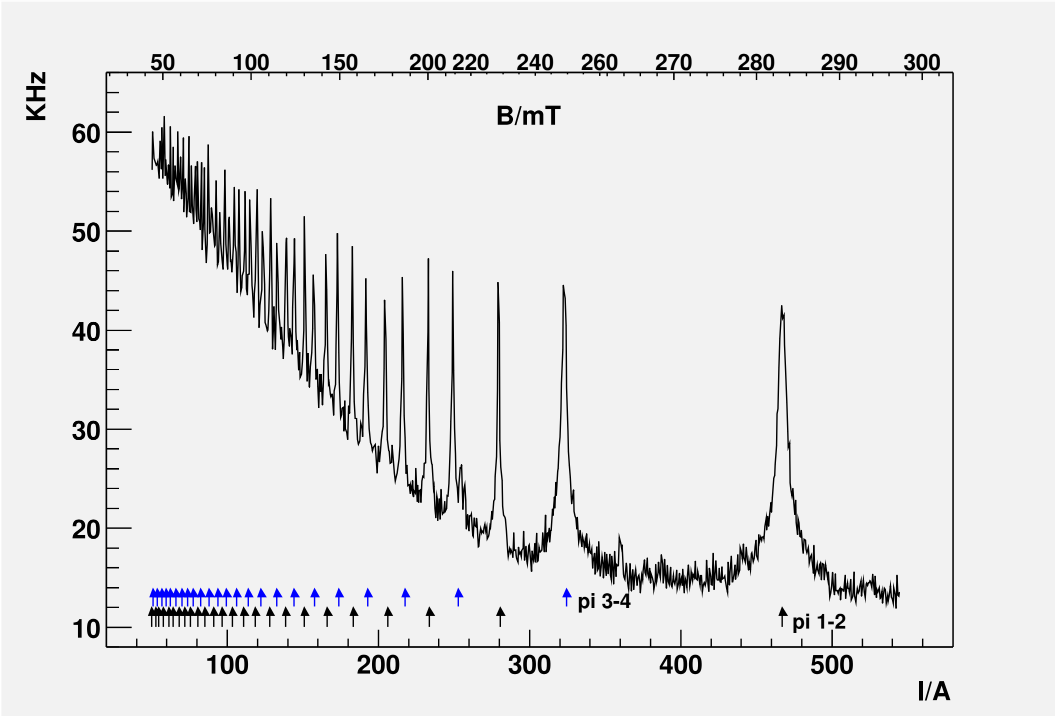

Figure 6.1: The measured BRP rates are shown as a function of target current/field. The peaks can be attributed to π_{12} and π_{34} resonances. The arrows show the predicted occurrences of these resonances, using the bunch frequency model described in section 2.3.

depends on the holding field. The best measurement is therefore of the 61_{st} π_{12} transition which occurs for a holding field of 282 mT.

Figure 6.2 shows this resonance together with a calculated resonance shape. The baseline and the height of the fitted line have been chosen to best fit the measured data, but the resonance shape and width are from equation 4.38. It is not possible to use this equation to calculate a peak height, as the initial hyperfine state populations are not known. In order to find the degree of depolarisation it is not enough to measure just one pair of states with the BRP, and the best method is to make a standard polarisation measurement, as listed in table 3.2.

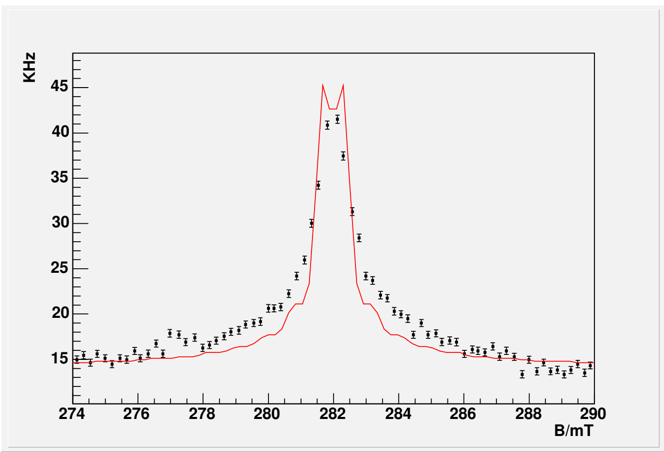

Figure 6.2: The measured BRP rates (black squares) are plotted, together with the transition probability as calculated from equation 4.38 but with an arbitrary scaling factor. (red line).

6.1.1 Shapes of the Nuclear π Resonances for Different Fills

In chapter 5 it was shown that the structure of the HERA fill could affect the resonance shape. Figure 5.7 showed the widening of the resonance for a HERA beam which was very far from the ideal case of 220 equally filled bunches. Flip-in measurements can be used to test the predictions from chapter 5.

The measurement as described in the previous section has been made for two different fills, one (run 2163) corresponding to the beam structure as shown in figure 5.4, the other (run 1478) to the beam structure as in figure 5.6. As these measurements were separated by several months, the rates differ greatly, due to improved tuning of the BRP detector. This is of no consequence to this measurement, except regarding the statistical error for each point. An immediate glance at figure 6.3 suggests that the peaks are wider for the

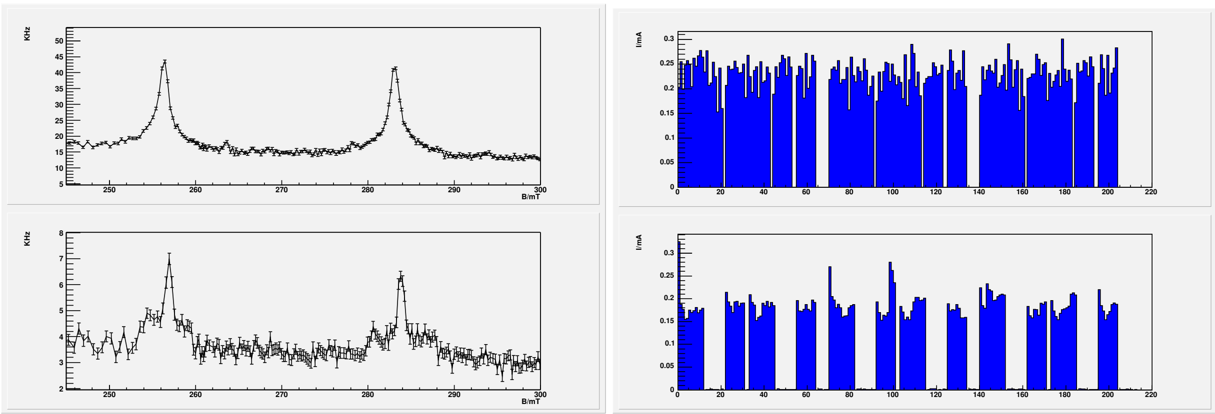

Figure 6.3: Left: BRP rates versus holding field (showing the 76_{th} π_{34} resonance and the 61_{st} π_{12} resonance) for two different HERA fills. Top: the *good fill* introduced in section 5.2, bottom for the *bad fill* described in the same section. Note the wider flanks for the fill shown at the bottom. This can be attributed to the differing fill structures shown on the right.

bottom plot. This suspicion is confirmed if we make a fit to the measured data using the resonance shapes calculated and shown in figure 5.7. The model does not exactly fit the measured data, especially for the very low statistical error in the left-hand plot.

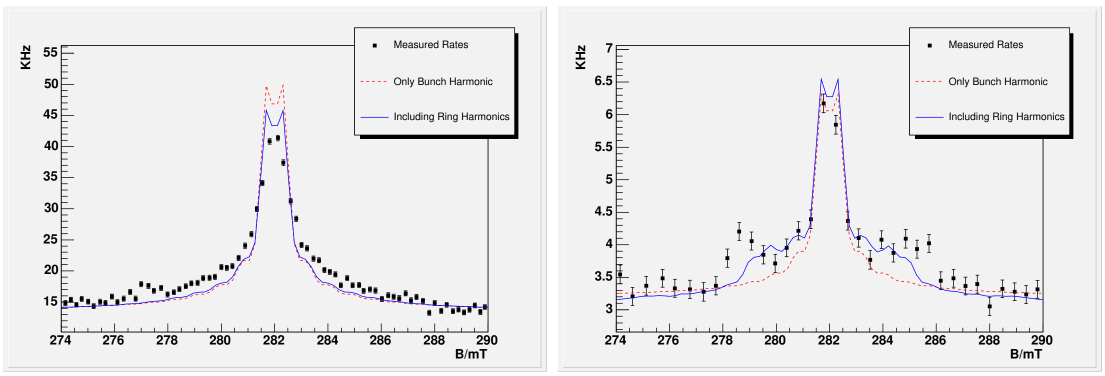

Figure 6.4: The measured resonance shape of the 61_{st} π resonance is shown, together with the shape as calculated in section 4.5, convoluted with the ring harmonics as calculated from the appropriate beam structure. For the *good fill* (left) the ring harmonics are not important, but for the *bad fill* (right) the ring harmonics play an important role in widening the resonance.

6.2 Polarisation Measurements

The disadvantage a polarisation measurement is that it takes roughly 6 times longer than a flip-in measurement. This means that it is not practical to scan the whole range shown in figure 6.2, but that it can be used to measure a single resonance. The advantage is that it is then possible to see how each of the four hyperfine states is affected by the resonance.

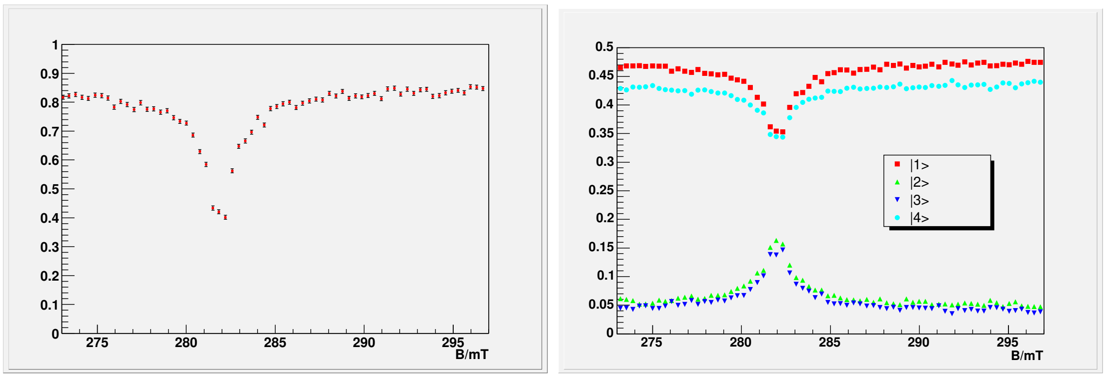

Figure 6.5: Whilst injecting states 1 and 4 from the ABS, the BRP continuously monitored the nuclear polarisation (left) as a function of holding field. The polarisation is calculated from the hyperfine state populations, shown right. Note that the π_{12} resonance depopulates both states $|\,1\,\rangle$ and $|\,4\,\rangle$. The chosen target field is at 297 mT, far away from the resonance.

6.2.1 Effect of Electron Polarisation on Nuclear π Resonances

Figure 6.5 shows how the four hyperfine state populations are affected by the π_{12} resonance. We can immediately see that an effect takes place which was not considered in section 4.5, namely that the populations of the hyperfine states $|\,3\,\rangle$ and $|\,4\,\rangle$, which are not *directly* affected by the π_{12} resonance, are nevertheless *indirectly* affected. This arises because of the low degree of electron polarisation in the target cell, which is typically less than 40% with no beam, and reduced to as little as 10% when the electron beam is present. Thus if state $|\,1\,\rangle$ is depopulated then state $|\,4\,\rangle$ will also be depopulated through either wall, spin-exchange or beam-induced electron depolarisation. Generally this coupling of all four states to one another is rather complicated, as it would be necessary to consider the probability of all six possible transitions between two states, and then solve the resulting differential equation. In general, starting with a population of n_1, n_2, n_3, n_4, after the first crossing of the cell and desorption from the cell wall the states will have changed slightly, so that:

$$\begin{pmatrix} n_1 \\ n_2 \\ n_3 \\ n_4 \end{pmatrix} \xrightarrow{\text{Desorption}} \begin{pmatrix} n_1 + P_{12}\Delta n_{21} + P_{13}\Delta n_{31} + P_{14}\Delta n_{41} \\ n_2 + P_{12}\Delta n_{12} + P_{23}\Delta n_{32} + P_{24}\Delta n_{42} \\ n_3 + P_{13}\Delta n_{13} + P_{23}\Delta n_{23} + P_{34}\Delta n_{43} \\ n_4 + P_{14}\Delta n_{14} + P_{24}\Delta n_{24} + P_{34}\Delta n_{34} \end{pmatrix} \tag{6.1}$$

where $\Delta n_{ab} = -\Delta n_{ba}$ means $n_a - n_b$, and P_{ab} is the probability of a transition between states a and b for one cell crossing, including desorption.

The system becomes easy to solve if we can rule out several transitions. The simplest model which could describe nuclear π transitions would be to say that only the considered

π transition can occur, so that, for example, only P_{12} is non-zero. In this case, the differential equation reduces to

$$\begin{pmatrix} n_1 \\ n_2 \\ n_3 \\ n_4 \end{pmatrix} \xrightarrow{\text{Desorption}} \begin{pmatrix} n_1 + P_{12}\Delta n_{21} \\ n_2 + P_{12}\Delta n_{12} \\ n_3 \\ n_4 \end{pmatrix} \tag{6.2}$$

which has the solution for N wall collisions:

$$\begin{aligned} n_1(N) &= \frac{1}{2}\Delta n_{12}(0)\cdot\exp(-2P_{12}N) + \frac{1}{2}(n_1(0)+n_2(0)) \\ n_2(N) &= \frac{1}{2}\Delta n_{21}(0)\cdot\exp(-2P_{12}N) + \frac{1}{2}(n_1(0)+n_2(0)) \\ n_3(N) &= n_3(0) \\ n_4(N) &= n_4(0) \\ &. \end{aligned} \tag{6.3}$$

In the high field limit ($\cos 2\theta \to 1$), equation 2.20 becomes

$$P_z = (n_1 + n_4) - (n_2 + n_3) \tag{6.4}$$

which for the above scenario becomes

$$P_z = \Delta n_{43}(0) + \Delta n_{12}(0)\cdot\exp(-2P_{12}N) \tag{6.5}$$

But of course this only applies in the absence of electron depolarisation, which is a very poor approximation for the HERMES target. A much better approximation is to assume complete electron depolarisation, so that states $|\,1\,\rangle$ and $|\,4\,\rangle$ are always equally occupied, as are states $|\,2\,\rangle$ and $|\,3\,\rangle$. In this case we can reduce the vectors in the calculation to just two components.

$$\begin{pmatrix} n_{1+4} \\ n_{2+3} \end{pmatrix} \xrightarrow{\text{Desorption}} \begin{pmatrix} n_{1+4} + \frac{1}{2}P_{12}(n_{2+3} - n_{1+4}) \\ n_{2+3} + \frac{1}{2}P_{12}(n_{1+4} - n_{2+3}) \end{pmatrix} \tag{6.6}$$

The factor of $\frac{1}{2}$ arises because states $|\,3\,\rangle$ and $|\,4\,\rangle$ do not experience the π_{12} resonance. The solution to this differential equation is

$$\begin{aligned} n_{1+4}(N) &= \frac{1}{2}(n_{1+4}(0) - n_{2+3}(0))\cdot\exp(-P_{12}N) + \frac{1}{2}(n_{1+4}(0)+n_{2+3}(0)) \\ n_{2+3}(N) &= \frac{1}{2}(n_{2+3}(0) - n_{1+4}(0))\cdot\exp(-P_{12}N) + \frac{1}{2}(n_{1+4}(0)+n_{2+3}(0)) \end{aligned} \tag{6.7}$$

which gives a nuclear polarisation of

$$P_z(N) = (\Delta n_{43}(0) + \Delta n_{12}(0))\cdot\exp(-P_{12}N). \tag{6.8}$$

which can be written as

$$P_z(N) = P_z(0)\exp(-P_{12}N) \tag{6.9}$$

Note that introducing electron depolarisation has caused the constant of exponential decay to be decreased by a factor of two, as state $|\,1\,\rangle$ is replenished by state $|\,4\,\rangle$, but allows the nuclear polarisation to sink to zero for the same reason. This model of complete electron depolarisation will be used to model the nuclear π resonances, as figure 6.5 suggests that the hyperfine populations of states $|\,1\,\rangle$ and $|\,4\,\rangle$ are strongly coupled, in agreement with this model.

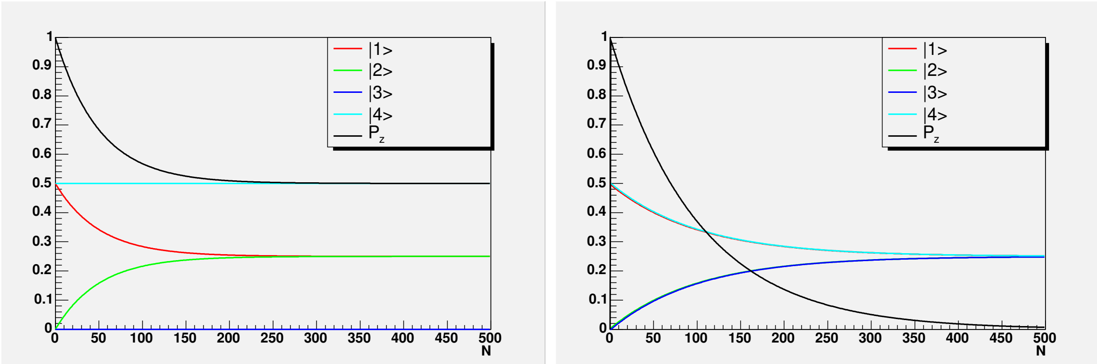

Figure 6.6: The relative populations of the four hyperfine states are plotted as a function of N, the number of wall collisions. Left: Assuming no electron depolarisation, from equation 6.3. Right: Assuming complete electron depolarisation, from equation 6.7, lines for states $|1\rangle$ and $|4\rangle$ lie on top of each other, as do the lines for states $|2\rangle$ and $|3\rangle$. In each case the initial conditions are that states $|1\rangle$ and $|4\rangle$ are equally populated and states $|2\rangle$ and $|3\rangle$ un-populated, and the probability of a π_{12} resonance per wall collision is 0.01. The nuclear polarisation in the strong field limit is also plotted.

6.2.2 Complete Simulations of the Nuclear π Resonances

At this point we have all the components needed to make a fit to the measured depolarisation from a nuclear π resonance. The probability for a single crossing of the cell is given by equation 4.38, whose integrals can be calculated numerically, as shown in section 4.5.

$$P_{\text{ave}}(\Delta\omega) = \frac{1}{2}\frac{g_s^2\mu_B^2\sin^2\theta}{\hbar^2}\frac{\mu_0^2 I^2}{64\pi^2{v_{y'}}^2}\int_{-R_{\text{cell}}}^{R_{\text{cell}}} dx' \left(\left|\int_{-y_0'/x'}^{y_0'/x'} \frac{1}{1+u^2}\cos\left(\Delta\omega\frac{x'}{v_{y'}}u\right)\,du\right|^2 + \left|\int_{-y_0'/x'}^{y_0'/x'} \frac{u}{1+u^2}\sin\left(\Delta\omega\frac{x'}{v_{y'}}u\right)\,du\right|^2\right) \quad (6.10)$$

This equation gives the depolarisation for a single crossing of the cell for the transverse field (hence the factor $\frac{1}{2}$ compared to equation 4.38). The number of collisions of particles *detected by the BRP* in the beam-tube of the cell can be found from the monte-Carlo simulation described in section 4.1, and for the present HERMES cell is found to be approximately 300. Equation 6.9 can then be used with the probability for one passage calculated from equation 6.10 and 300 passages to find the total degree of depolarisation. Although the beam-induced depolarising effects occur in parallel to the wall and spin-exchange effects, it is possible to use the measured hyperfine state populations away from resonance for the initial polarisation.

Figure 6.7 shows the measured polarisation together with the calculated value from equation 4.38, for a beam current of 48mA. The calculated resonance shape fits the measured data well (although not exactly), as already seen from figure 6.2, but it is now clear that the strength of the resonance is also well-reproduced. Remember that the assumptions for this calculation included a homogeneous field throughout the cell, so that the width of the resonance arises solely from the time-energy uncertainty relation. Other assumptions were that the cell is circular in cross section and that the electron beam produces a **B** field whose magnitude depends *solely* on $\frac{1}{r}$, where r is the distance from the cell axis. Under these circumstances the agreement between calculated and measured polarisation is as good as could be hoped for.

It is worth noting that the depth of the resonance is much larger that the values pre-

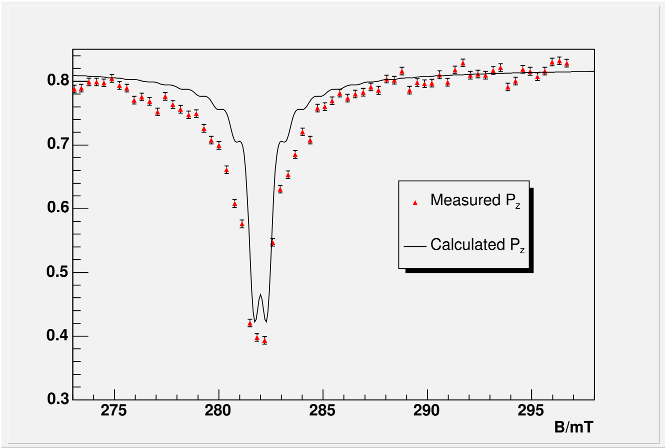

Figure 6.7: The measured polarisation is compared to the calculated polarisation, assuming an initial polarisation of 82%. The electron beam current was 48 mA. 20 seconds were needed to measure each polarisation value, during which time the holding field was continually increased.

sented in [Ack99], where the polarisation drops from 90% to 75%. This can be attributed to the better field homogeneity in the z direction, so that the resonance is present along the whole length of the target cell, and not just at a couple of localised points. This is despite the fact that for the longitudinal magnet the holding field is *always* transverse to the RF field, which leads to a stronger resonance. The resonance has now become symmetric and is narrower than for the longitudinal magnet, again because the field homogeneity is much improved.

Chapter 7

Depolarisation from the σ_{24} Resonance

Subject of chapter scores an Enigma Variation. (5,9)

7.1 Introduction

The σ_{24} resonance has the potential to be particularly troublesome for the HERMES experiment. It was shown in chapter 2 that this resonance causes a flip of both electron and nuclear polarisation in the strong-field limit, and is narrowly spaced (every 0.37 mT). Unlike the narrowly spaced electron resonances, whose matrix element increases with holding field, the matrix element for the σ_{24} resonance drops for higher fields (equation 2.52). Nevertheless, it is important to ensure that the effect of this resonance on the nuclear polarisation at HERMES is kept to an absolute minimum.

The field measurements of the target magnet (section 3.4) showed that the homogeneity of the target was not quite sufficient to eliminate the tightly spaced σ resonances, but that it should allow direct measurements of individual resonances.

This was not possible for the longitudinal magnet, where a total of eight electron resonances [Kol98] were in the cell at any one time. Of course σ resonances were forbidden by the selection rules developed in chapter 2.2.1 from occurring in the longitudinal magnet, but the σ and electron π transitions are both characterised by the narrow spacing of 0.37 mT in the high-field limit, as shown in section 2.3.1. This means that the electron π transitions can be used to test the homogeneity of the target magnet, which is especially useful as these resonances are not suppressed by the holding field, as shown in figure 2.5.

We would expect, therefore, that by slowly varying the target field, we would induce these resonances, and that we can observe them using the BRP.

7.2 Measuring the σ Resonances

Due to the narrow spacing of these resonances, they can be most easily identified in the low field region, where $\frac{d(\Delta E)}{dB}$ in the Breit-Rabi diagram is at its lowest, as shown in figure 2.2. The σ resonances are also strongest in this region, as their matrix element (figure 2.5) is unitary for very low fields. The quickest measurement is the “flip-in” measurement, where a beam resonance produces an increased signal in the BRP. The limitation of this technique is its inability to distinguish between possible resonances which could have produced the peak. This is illustrated in figure 7.1, which shows the BRP rates as a function of target field in the low-field region. Only by virtue of their increased spacing at lower fields is it possible to recognise the σ_{24} resonances. The advantage of the flip-in measurement is its speed; the data for this plot was taken in around 20 minutes, with a beam current of around 20mA. Thus any systematic time effects are kept to a minimum, and the resolution of the resonances are optimised. The short duration of this measurement also means that it could be performed during the final stages of beam optimisation ("Luminosity tuning") during which the HERMES detector is still in standby mode, so that no beam-time for HERMES is lost. If more information about

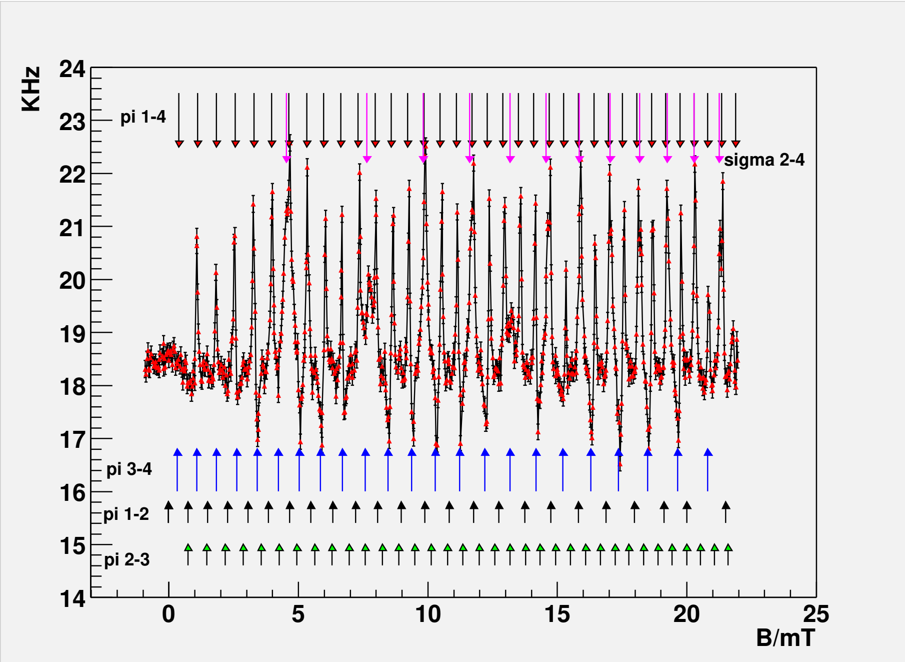

Figure 7.1: Transitions in the low field region. State $|4\rangle$ was injected by the ABS, whilst the BRP rates for measuring states $|1\rangle$ and $|2\rangle$ are shown. The peaks can be attributed to the π_{14} and σ_{24} transitions which both cause the initial state to be flipped into one of the states to which the BRP is sensitive. The dips are caused by the π_{34}, which moves atoms from the initial state $|4\rangle$ to the pure state $|3\rangle$. Wall and volume depolarisation are then inhibited, as atoms in state 3 are less likely than those in state 4 to depolarise in a weak field.[Bau00]

the resonance is needed, then it is preferable to use the BRP in its usual polarisation measuring mode, where a different pair of states is measured every few seconds. By measuring the polarisation it is possible to know exactly the extent of depolarisation caused by a resonance, and also between which two states a resonance occurred.

7.3 Testing the Homogeneity of the Target Magnet

Although figure 7.1 is of general interest, and shows the high homogeneity of the target magnet at least for low fields, of more importance to the HERMES experiment are measurements at the working point of the HERMES target. Here the σ resonances are separated by 0.37mT, and can be found together with the electron π resonances, which are without consequence for the nuclear target polarisation. If the effect of the sigma resonances is to be minimised, then two requirements must be met; firstly that the homogeneity of the field throughout the target cell is sufficient that a point can be chosen between two resonances, and secondly that the average target field is chosen exactly such that it is halfway between two resonances.

The first requirement is equivalent to saying that it must be possible to resolve the σ resonances, as shown in the low field region in figure 7.1. The most effective method to test this requirement is using the flip-in technique. As the sigma resonances are suppressed for high holding fields, it is preferable to perform this "resolution" check using an electron π transition. These transitions have the same spacing (0.37 mT) as the σ_{24} transition, as $\frac{d(\Delta E)}{dB}$ is the same, but a greater probability of occurring. The ratio of π_{14} to σ_{24} probability at a field of 297 mT is given by

$$P_{14}/P_{24} = \frac{\cos^2\theta}{\sin^2 2\theta} \tag{7.1}$$

with $\tan 2\theta = B_c/B$. For the field of 297 mT we then find that the probability of an electron π resonance is 35 times more likely than that for a σ resonance.

Figure 7.2 shows a flip-in measurement made in the high field region with the same conditions as for figure 7.1, namely injecting state $|\,4\,\rangle$ from the ABS with the BRP sensitive to states $|\,1\,\rangle$ and $|\,2\,\rangle$, whilst the magnetic field of the target is slowly increased (such a measurement takes around 20 minutes).

Thus the peaks can be attributed to the π_{14} resonance.[1] Although the individual

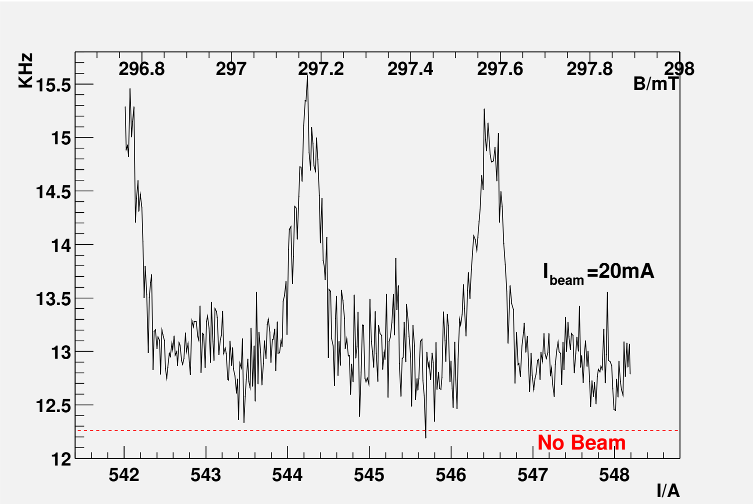

Figure 7.2: BRP rates as a function of holding field for states 1 and 2 whilst injecting state 4 from the ABS. Here the cell coil was not in use. The peaks can be interpreted as π_{14} transitions.

resonances are clearly resolved, at no point do the BRP rates sink to the level seen for no beam. A possible reason for this is that the magnet homogeneity is insufficient. Simulations of the target magnet and later field maps both suggested that the homogeneity of the target magnet in the x direction was to 0.6 mT (or 0.2%), which is insufficient to eliminate σ resonances. This measurement of the electron resonances confirms that some effect is present for all values of the target magnet field. As a result, an additional coil was built into the cell to improve the homogeneity in the x direction.

[1] This measurement does not exclude the σ_{24} as a possible cause, but further measurements confirmed that the π_{14} resonance is indeed shown here.

7.4 Effect of the Cell Correction Coil

The cell correction coil, described in section 3.4.1 was designed to improve the x homogeneity of the target field by producing an additional field which, when superimposed on the field from the main magnet coil, produces a more homogeneous field.

7.4.1 Tests using the Electron Transitions

The improvement in the field homogeneity caused by the cell coil can be tested using the measurements as described in section 7.3. In figure 7.3 it can clearly be seen that

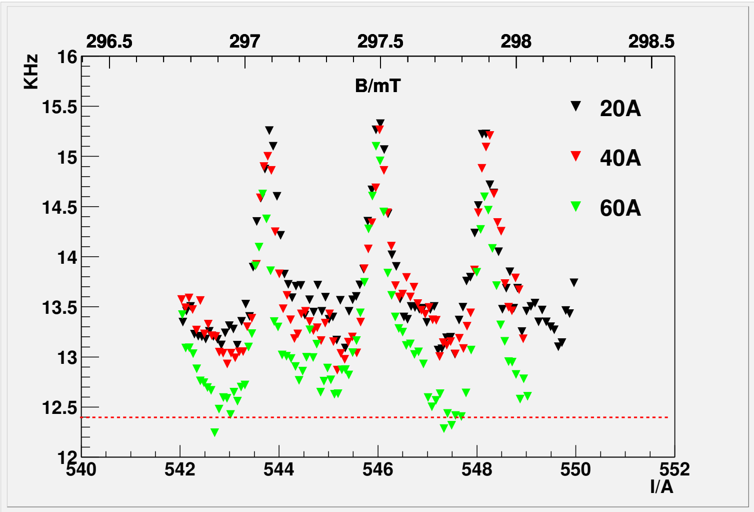

Figure 7.3: Taken at the start of a fill with 33mA electron current; the changing shapes of the π_{14} resonances can be seen as the cell correction coil is turned on. The dashed line shows the rates for no beam.

as the current of the cell coil is increased, the rates at a field setting in between two resonances sink. This suggests that the homogeneity of the magnet is being significantly increased. For the case that the resonances were completely eliminated, we would expect that the rates between two resonances would be equal to the rates measured with no HERA electron beam. There can be many possible explanations for the residual spin-flip probability at fields in between the π_{14} resonances. It is possible that other weaker resonances (such as the σ_{24}) exert an influence, or that the cell coil does not completely solve the x homogeneity problem. For such complicated discussions the flip-in method again reveals its limits. The necessity, and at least partial success of the cell correction coil have however been tested with these measurements.

7.4.2 Tests with the σ_{24} Transitions

The crucial test of the cell correction coil is how effective it is in keeping the nuclear polarisation as high as possible. Polarisation measurements of the σ resonances take too long to be performed during Luminosity Tuning, but can be made concurrently with standard polarised running of the HERMES experiment. The small short-term loss in polarisation during the scan is unimportant, and such measurements are unavoidable if the optimal point for the target field is to be found. A typical polarisation measurement takes roughly two minutes, so the range of a complete resonance (0.37mT) takes 1-2 hours.

Such a measurement is shown in figure 7.4, and can be used to select a magnetic field in-between two sigma resonances. It is also interesting to look at the relative hyperfine-state populations during such a scan. The resonance reduces the polarisation for both Pz+ and Pz- injections, and because of low electron polarisation (around 0.2), the σ_{24} resonance also affects the number of atoms in states $|\,1\,\rangle$ and $|\,3\,\rangle$. The drop in nuclear polarisation tells us that the resonance must be a nuclear resonance, ruling out, for example the π_{14} resonance as a candidate, and from the spacing between resonances we can deduce that the cause must be the series of σ_{24} resonances. This additional information about the nature of the transition in the cell (not possible with the flip-in measurement) has been gained at the cost of knowledge of the exact shape of the resonance. Nevertheless, it is interesting to compare the results of such a polarisation measurement with and without the cell coil.

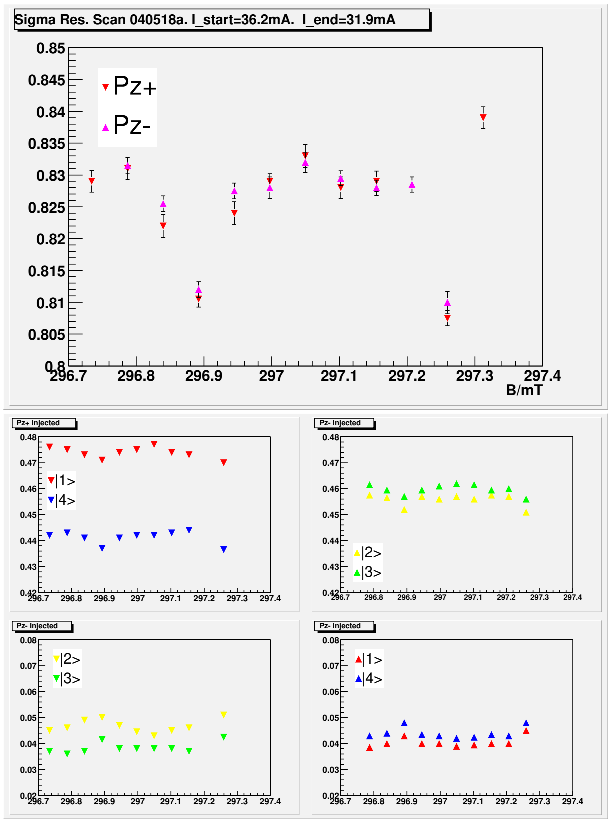

Figure 7.4: (Top) Polarisation is shown for Pz+ and Pz- injected as a function of magnetic field. The relative hyperfine-state populations (lower plots) are used to find the polarisation, and also here the σ_{24} resonances can be seen at 296.9 mT and 297.25 mT.

Figure 7.5 shows the polarisation for a scan without the cell coil. Here the result of the flip-in measurements is confirmed, as the resonance has increased in width. It is not possible to make a direct comparison between the polarisation values with and without cell coil, as the cell coating improved between the two measurements. The final determination of the necessity of the cell coil requires two measurements made in the same electron fill.

7.5 Final Result of Cell Coil.

It has been shown that an optimal set point for the magnetic field can be found, with or without the cell coil. In each case, with feedback from the Hall probe, it is possible to

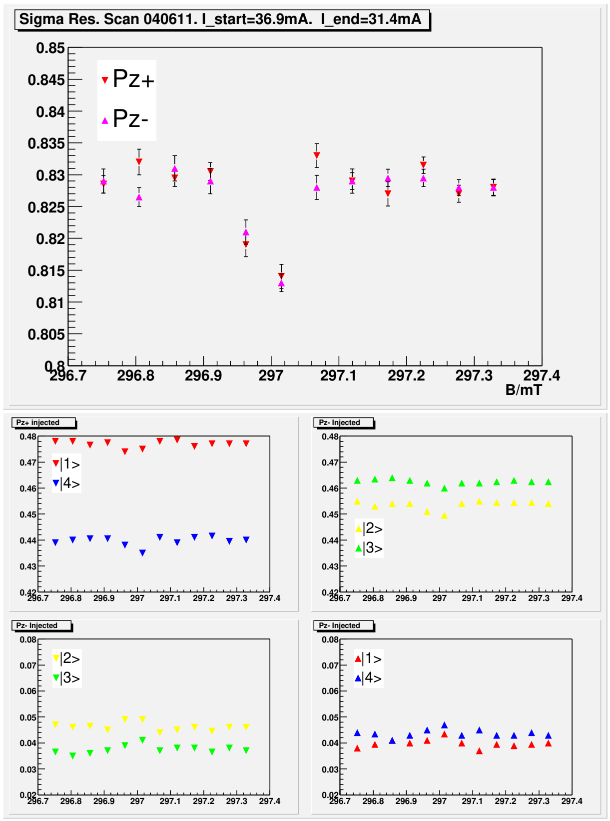

Figure 7.5: As for figure 7.4, but with the cell coil turned off.

Cell Coil/A	HERA Current/mA	Pz+	Pz-
0	36	0.824±0.001	0.818±0.001
60	35	0.830±0.001	0.825±0.001
60	20	0.843±0.001	0.837±0.001

Table 7.1: Measured polarisation values during a single fill. For both cell-coil settings, the magnetic field had been chosen for optimal polarisation. The errors shown are the statistical errors.

operate the target over an electron fill, without running into a σ resonance. The flip-in measurements suggest that the optimal setting for the cell coil, within the constraints set by the cooling capacity of the target cell, is with a current of 60 A, but that some depolarisation remains unavoidable. In June 2004, HERA repeatedly reached beam currents of around 40mA at the start of a fill. The final requirement, therefore, is an equivalent measurement of polarisation for the three cases of no beam, 40mA beam without cell coil, and 40mA beam with cell coil. On June 1. 2004, such a measurement was made, with the results as in table 7.1. The polarisation is markedly improved for the case that the cell coil is turned on (with 60 A), but does not reach the value with no beam (here approximated by the value for a much lower beam current of 20 mA).

For the measurement shown in table 7.1, it was not possible to measure the polarisation with zero current, as the target magnet was turned off before the end of the HERA fill. A more accurate comparison of the final degree of depolarisation from the HERA beam can be found from a beam dump, where all electrons were kicked out of the ring shortly after the start of a luminosity run, as shown in table 7.2. This measurement shows that a

Cell Coil/A	HERA Current/mA	Pz+	Pz-
60	45.4	0.824±0.001	0.817±0.001
60	0	0.841±0.001	0.836±0.001

Table 7.2: The measured polarisation before and after a 45mA beam dump on June 2. The target magnetic field had been chosen for optimal polarisation.

polarisation loss of almost 0.02 occurs for a beam current of 45.4 mA even when the cell coil is used. A further check can be made by measuring the polarisation over an entire fill, as shown in figure 7.6.

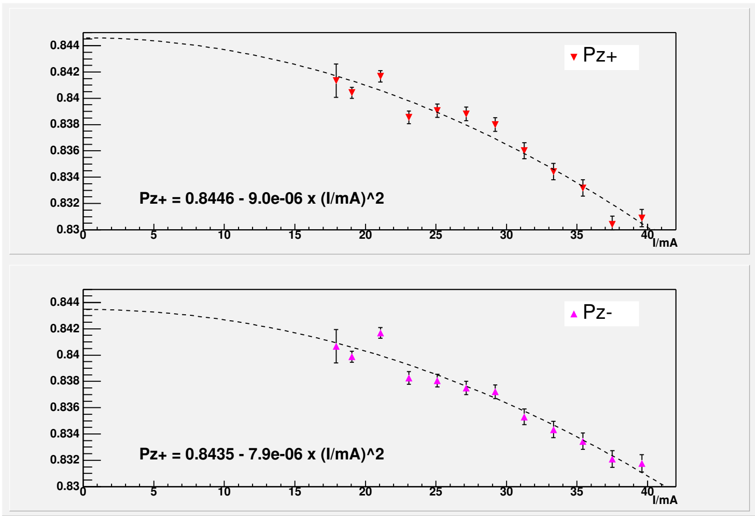

Figure 7.6: . Averaged polarisation as a function of current during an electron fill (on 12. June 2004). The cell coil was set to 60A, as usual, and the target magnetic field held constant throughout. A fit is shown, assuming that the depolarisation varies only with the square of the current.

7.6 Conclusions

The cell coil has been proved to improve the homogeneity of the **B** field in the target cell, thereby reducing depolarisation from the HERA electron beam. The reduction of depolarisation is roughly $\frac{1}{3}$ of the total effect. Thus, even with the cell coil in place and a careful selection of the magnetic field, it is not possible to completely eliminate beam depolarisation, and for a 40 mA beam current the polarisation is reduced by 0.015 compared to the value for no beam.

Magnetic field calculations suggest that a higher contribution from the cell coil would further improve the field homogeneity, and this is supported by the measurement shown in figure 7.3, where no saturation in the effect of the cell coil for higher field contributions can be seen. Any further possible improvements of the target field would, however, have to be balanced against other considerations for the HERMES experiment. The cell coil was designed to avoid presenting any matter in the acceptance angle of the HERMES detector, and a maximum absolute depolarisation of 0.015, with an average effect much lower, would probably not justify any action with any negative side-effects.

The highly homogenous target field with further improvement from the cell correction coil, the long-term stability and reproducibility of the target field and careful selection of the **B** field ensure that beam depolarisation has a minimal influence on the final target polarisation.

Chapter 8

Discussion and Outlook

The basic phenomenology of beam-induced resonances, resulting from the Fourier analysis of the electron beam, the energy difference between states and the selection rules, has been long known, and was described correctly in the HERMES technical design report. This knowledge was the basis for the design constraints of the longitudinal magnet, with which first measurements of the nuclear π resonances could be made.

These measurements could showed rather odd peak shapes, which could be explained by the z modulation of the holding field, together with a natural width resulting from the time-energy uncertainty relation. Electron resonances could not be isolated, as many of these resonances were in the cell at any one time.

The transverse target magnet was designed to suppress the σ resonances, which arose from the new orientation of the holding field. Although imperfect in this respect, the effect of the σ resonances is kept to a very low level by the good homogeneity of the target magnet, and even more so when the cell-coil is used. For a beam current of 40 mA, the additional absolute loss of measured polarisation was found to be 0.015.

A tracking Monte-Carlo simulation proved to be a useful tool to explain the shape and strength of the σ and electron π resonances, which are localised to a region in the cell corresponding to the resonant field line. Detailed measurements of these resonances were made, and could be used to select the optimal working point of the HERMES target.

The nuclear π resonances are widely spaced for fields far above the critical field, and are much easier to avoid than the narrowly spaced σ resonances. The highly homogeneous transverse target magnet proves to be an excellent instrument to measure these resonances, and a satisfactory explanation of the measured resonance shape can be found using a simplified model of the cell, assuming a circular cross-section, an electron beam with an infinitely small radius, and a holding field which is perfectly flat across the whole region of the cell.

It would be possible to further develop this model to describe the nuclear π resonances to take account of the elliptical cell shape, using numerical solutions to the integrals needed to solve the time-dependent Schrödinger equation. The loss of symmetry, however, leads to the calculations being much more complicated, and for this reason, and because of the relative success of the simple model presented here, no such calculations are included in this thesis.

A constant background to the work here are the effects of spin-exchange depolarisation and depolarisation on the walls of the target cell. These effects amount to a loss of around 15% in measured polarisation, which is much larger than the possible effects of the σ resonance. These effects have been studied in detail at HERMES, but the phenomenon of wall depolarisation, especially in a radiation-prone environment, is certainly far from being completely understood.

At HERMES it is unimportant how strong the electron polarisation of the target is, therefore no attempts were made to minimise the electron π resonances. The matrix element of these resonances increases with holding field, so they are particularly strong around the working point of the target. If an experiment required high electron polarisation, then these tightly spaced resonances must be carefully considered. In any case, the models presented here should allow the effects from beam-induced depolarisation to be quantitatively predicted during the design stage of an experiment.

Producing targets of higher density whilst keeping the nuclear and also possibly electron polarisation high will be a major challenge for future polarised gas targets.

Appendix A

A Thorough Calculation of τ

In section 4.1.1 we somewhat arbitrarily placed the limit for $\omega_{HF} - \omega_{ab}$ at $2\pi/t$. This follows the convention of defining the resonance width using the first zero point in the sinc^2 distribution, as detailed for example in [Coh99].

For our particular problem, we must consider exactly what happens when a particle crosses a resonant surface. We have already defined that for the region considered, $\Delta\omega$ is directly proportional to the distance separating the particle from the resonant surface. Thus we can imagine the particle moving across the sinc^2 distribution, experiencing the peaks and troughs, and in total experiencing a depolarising probability caused by integration over the whole range of $\Delta\omega$. But for what time does the resonance condition then apply? The problem is that no abrupt start or end of the resonance is evident, just as it is impossible to look at the interference pattern from Fraunhofer diffraction, and state at which point the fringes end.

One way round this problem is to represent the sinc^2 distribution with a rectangular distribution, which has the same central value (t^2), and an equal integral over all $\Delta\omega$, as shown in figure A.1. This can only be achieved by giving the rectangle a full width of $2\pi/t$. Note that this is not exactly the equivalent of a full width at half maximum, for $\Delta\omega = \pi/t$ this value the sinc^2 function has dropped to a value of 0.405 times its peak value. This may seem to be a quick fix, which indeed it is. Apart from its aesthetic value, there seems no physical reason to demand that the two integrals be equal, or even that it is reasonable to make the rectangular approximation.

A more thorough approach is to take several steps back, and re-examine the solution of the time-dependent Schrödinger equation. The coefficient which gives arise to transitions between states, was shown to be (equation 2.45)

$$c(\tau) = \frac{W_{ab}}{i\hbar} \int_0^\tau \exp\left(i\omega_{ab}t\right) \sin(\omega t) dt. \tag{A.1}$$

Previously we proceeded by integrating directly, and so were able to calculate the sinc^2 distribution. The important change that we make is to declare ω_{ab} to be time dependent. The frequency of the radiation, ω, on the other hand, certainly stays constant for any particular harmonic.

As the particle passes through the cell it will start at a region where ω_{ab} is lower than ω, reach the resonant condition, and continue to a region where the reverse applies. We can approximate this time dependence of ω_{ab} as

$$\omega_{ab} = \omega_0 + \lambda t. \tag{A.2}$$

Inserting this time-dependent expression for ω_{ab} into the equation for $c(\tau)$, and expressing

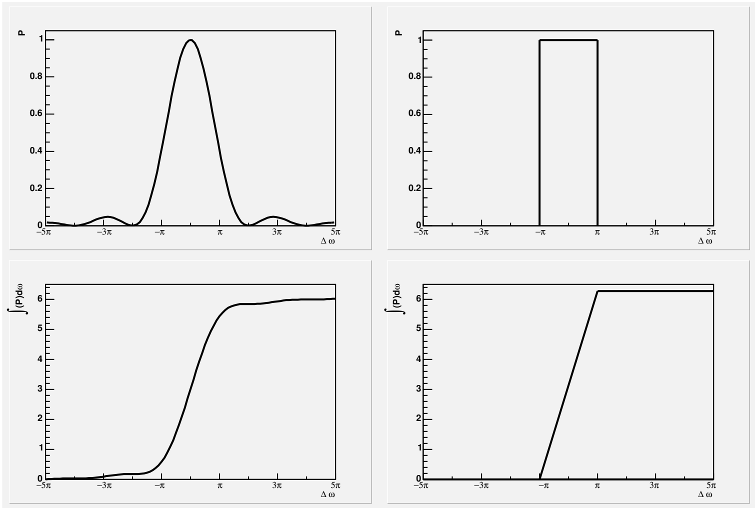

Figure A.1: The sinc^2 distribution and its integral are shown for the case that $t = 1$ s (left). $\Delta\omega$ is then given in rad/s. A rectangular approximation to this distribution is shown also (right)

the sine term in its exponential form gives

$$c(\tau) = -\frac{W_{ab}}{2\hbar}\int_0^\tau \left[\exp\left(i(\omega_0 + \lambda t + \omega)t\right) - \exp\left(i(\omega_0 + \lambda t - \omega)t\right)\right] dt. \tag{A.3}$$

We may immediately recognise that the first term in the integrand is responsible for emission, and the second for absorption. We proceed with only the second term by letting $\omega_0 = \omega$, which just means that at some point the resonance is exactly fulfilled. This point then defines where $t = 0$. Because of the time dependence of ω_{ab} it is no longer necessary to define exactly when the perturbation begins and ends. The perturbation is effectively present for all time, but is only likely to cause a transition when ω_{ab} approaches ω. Thus we can change the lower and upper limits to $-\infty$ and ∞.

$$c(\lambda) = \frac{W_{ab}}{2\hbar}\int_{-\infty}^{\infty} \exp\left(i\lambda t^2\right) dt. \tag{A.4}$$

In order to solve this integral it is helpful to express the exponential function again in the trigonometric form, so

$$c(\lambda) = \frac{W_{ab}}{2\hbar}\left[\int_{-\infty}^{\infty} \cos\left(\lambda t^2\right) dt + i\int_{-\infty}^{\infty} \sin\left(\lambda t^2\right) dt\right]. \tag{A.5}$$

The form of the functions and their integrals are shown in figure A.2. The solution to these integrals can be found in [Korn]:

$$\int_{-\infty}^{\infty} \cos\left(\lambda t^2\right) dt = \int_{-\infty}^{\infty} \sin\left(\lambda t^2\right) dt = \sqrt{\frac{\pi}{2\lambda}} \tag{A.6}$$

Squaring the equation for $c(\lambda)$ gives the transition probability,

$$P_{ab} = \frac{W_{ab}^2}{4\hbar^2}\frac{\pi}{\lambda} \tag{A.7}$$

λ was defined as being the amount by which ω_{ab} changes in a given time, and using the chain rule

$$\lambda = \frac{d\omega}{dt} = \frac{\partial\omega}{\partial B_y}\frac{\partial B_y}{\partial x}v_x + \frac{\partial\omega}{\partial B_y}\frac{\partial B_y}{\partial y}v_y + \frac{\partial\omega}{\partial B_y}\frac{\partial B_y}{\partial z}v_z. \tag{A.8}$$

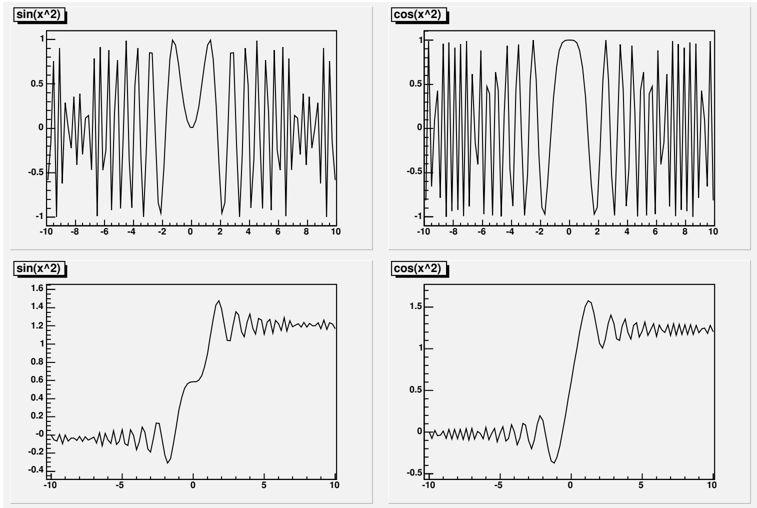

Figure A.2: Top: the functions $\sin(ax^2)$ and $\cos(ax^2)$ for the case that $a = 1$. Bottom: the corresponding integral functions. Increasing a has the effect of compressing the function in the x direction, and thereby decreasing the size of the integral. a and x are dimensionless here.

Substituting this expression for λ, the transition probability becomes

$$P_{ab} = \frac{W_{ab}^2}{4\hbar^2} \frac{\pi}{\frac{\partial \omega}{\partial B_y}\left(\frac{\partial B_y}{\partial x} v_x + \frac{\partial B_y}{\partial y} v_y + \frac{\partial B_z}{\partial y} v_z\right)} \tag{A.9}$$

Comparison with equation 2.49 then gives an effective interaction time,

$$\tau_{\text{eff}}^2 = \frac{\pi}{\lambda} = \frac{\pi}{\frac{\partial \omega}{\partial B_y}\left(\frac{\partial B_y}{\partial x} v_x + \frac{\partial B_y}{\partial y} v_y + \frac{\partial B_y}{\partial z} v_z\right)} \tag{A.10}$$

which can be expressed in the more compact vector form:

$$\tau_{\text{eff}}^2 = \frac{\pi}{\frac{\partial \omega}{\partial B_y} |\nabla B_y \cdot \mathbf{v}|} \tag{A.11}$$

Note that τ_{eff} is a factor of two smaller than τ as estimated from the rectangular approximation. In any case, all calculations in the Monte Carlo are made with equations A.10 and 2.49. This equation for τ is identical to that given on p.21 in [Gra98], who argued that this is the time needed for the atom to "run out of phase".

Appendix B

Field Measurements

The results of the field mapping of the target magnet with a Hall probe which could be moved in 3-dimensions. In all cases, the current passed through the magnet was 545A.

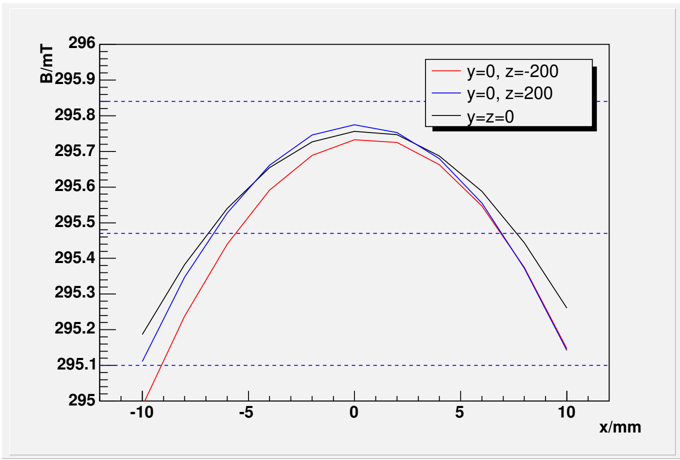

Figure B.1: x homogeneity of transverse magnet, at both ends of the cell and in the centre. The horizontal lines show the spacing of σ resonances.

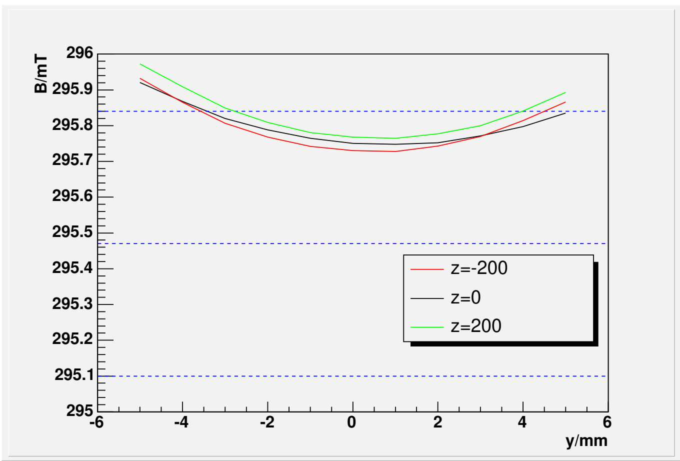

Figure B.2: y homogeneity of transverse magnet, at both ends of the cell and in the centre. The horizontal lines show the spacing of σ resonances.

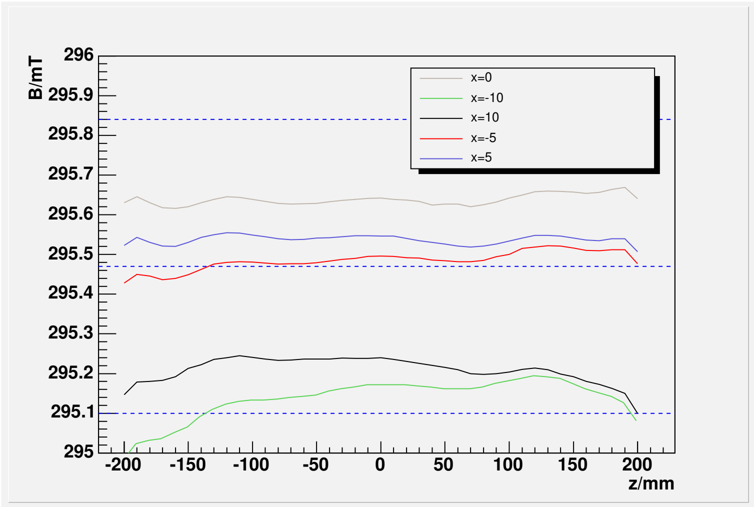

Figure B.3: z homogeneity of transverse magnet, shown for different x positions. The horizontal lines show the spacing of σ resonances.

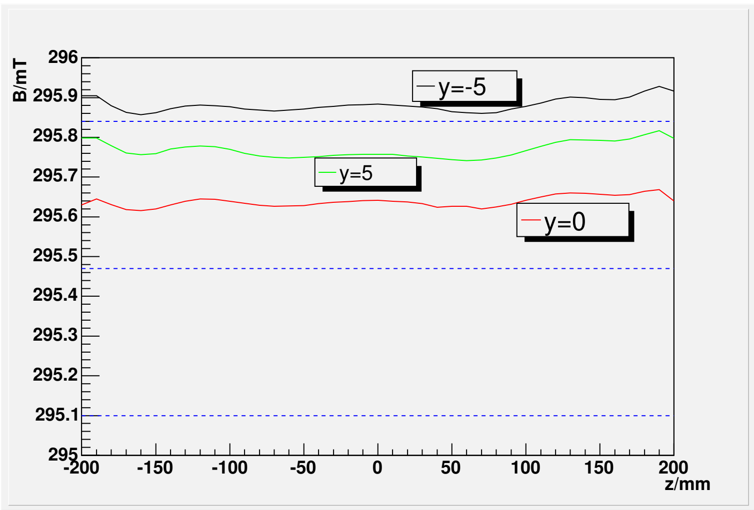

Figure B.4: z homogeneity of transverse magnet, shown for different y positions. The horizontal lines show the spacing of σ resonances.

Appendix C

Proof that the Statistical Weight is Independent on x'

In section 4.5 we used both the point of closest approach, x', and the desorption angle ξ to describe the trajectory of a particle across the plane section of a cylindrical cell. As

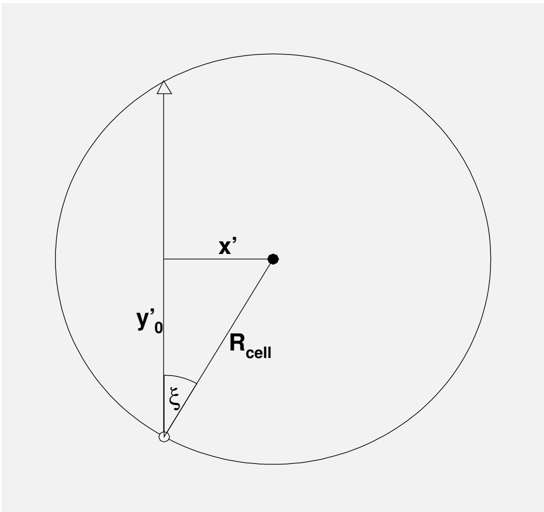

Figure C.1: The desorption angle, ξ, is shown, together with the corresponding minimum distance to the beam, x'.

shown in figure C.1, the desorption angle and minimum distance to the beam are linked by the equation

$$x' = R_{\text{cell}} \sin \xi \tag{C.1}$$

which can be differentiated to give

$$\frac{dx'}{d\xi} = R_{\text{cell}} \cos \xi \tag{C.2}$$

The probability of a particle being desorbed with angle ξ is

$$P(\xi) d\xi = \cos \xi d\xi \tag{C.3}$$

Inserting equation C.2 into C.3 gives

$$P(x') dx' = \frac{1}{R_{\text{cell}}} dx' \tag{C.4}$$

so all values of x' are equally likely.

Bibliography

[Ack98] K. Ackerstaff *et al.* [HERMES Collaboration], "HERMES spectrometer," Nucl. Instrum. Meth. A **417** (1998) 230

[Ack99] K. Ackerstaff *et al.* [The HERMES Collaboration], "Beam-induced nuclear depolarization in a gaseous polarised hydrogen target," Phys. Rev. Lett. **82** (1999) 1164

[Air04] A. Airapetian *et al.* [HERMES Collaboration], "Quark helicity distributions in the nucleon for up, down, and strange quarks from semi-inclusive deep-inelastic scattering," Phys. Rev. D **71** (2005) 012003

[Ama02] M. Amarian. Private Communication.

[Bar93] D. P. Barber *et al.*, "The HERA polarimeter and the first observation of electron spin polarization at HERA," Nucl. Instrum. Meth. A **329**, 79 (1993).

[Bar01] V. Barone, A. Drago and P. G. Ratcliffe, "Transverse polarisation of quarks in hadrons," Phys. Rept. **359** (2002) 1

[Bau00] C. Baumgarten. "Studies of Spin Relaxation and Recombination at the HERMES Hydrogen/Deuterium Gas Target". PhD Thesis, Ludwig-Maximilians Universität Muenchen, 1995.

[Bau02] C. Baumgarten *et al.*, "An atomic beam polarimeter to measure the nuclear polarization in the HERMES gaseous polarized hydrogen and deuterium target," Nucl. Instrum. Meth. A **482** (2002) 606.

[Bau02b] C. Baumgarten *et al.*, "Molecular flow and wall collision age distributions," Eur. Phys. J. D **18** (2002) 37.

[Bau03] C. Baumgarten *et al.*, "The storage cell of the polarized H/D internal gas target of the HERMES experiment at HERA," Nucl. Instrum. Meth. A **496** (2003) 277.

[Bau03b] C. Baumgarten *et al.*, "A gas analyzer for the internal polarized target of the HERMES experiment," Nucl. Instrum. Meth. A **508** (2003) 268.

[Bec02] M. Beckmann *et al.*, "The longitudinal polarimeter at HERA," Nucl. Instrum. Meth. A **479** (2002) 334

[Bra95] B. Braun; "Spin Relaxation of Hydrogen and Deuterium in Storage Cells", Ph.D. Thesis, Ludwig-Maximilians Universität Muenchen, 1995.

[Bru01] I. Brunn; Diploma Thesis, Friedrich-Alexander-Universität Erlangen-Nürnberg, March 1999.

[Boe97] G. Boero, W. Kubischta and P. Leprince, “A high-flow hydrogen dissociator based on a surface-wave discharge,” Nucl. Instrum. Meth. A **398** (1997) 157.

[Coh99] C. Cohen-Tannoudji, B. Diu, F. Laloe; Quantenmechanik, 2. Auflage, Walter de Gruyter, 1999.

[Die04] M. Diefenthaler, ”Tiefinelastische Elektronenstreuung an einem transversal polarisierten Wasserstoff-Target”, Diploma Thesis, Friedrich-Alexander-Universität Erlangen-Nürnberg, 2004.

[Dun82] J .S. Dunham *et al*; Polarized gas jet targets. *Proc. 5th Int. Symp. on Polarization Phenomena in Nuclear Physics*, (Santa Fe, 1980)

[E143] K. Abe *et al.* [E143 Collaboration], “Precision measurement of the proton spin structure function g1(p),” Phys. Rev. Lett. **74** (1995) 346.

[E155] P. L. Anthony *et al.* [E155 Collaboration], “Precision measurement of the proton and deuteron spin structure functions g2 and asymmetries A(2),” Phys. Lett. B **553** (2003) 18

[Fer97] M. Ferro-Luzzi *et al*; Zeeman Transitions in Deuterium Atoms Induced by Ultra-relativistic Electrons. *Hyperfine Interactions* 110 (1997) 239-257.

[Gau92] H-G. Gaul and E. Steffens; Nucl. Instr. Meth. A 316 (1992), 297-305.

[Gil93] R. Gilman *et al.*, “A Polarized gas internal target using a storage cell in an electron storage ring,” Nucl. Instrum. Meth. A **327** (1993) 277.

[GPV01] K. Goeke, M. V. Polyakov and M. Vanderhaeghen, “Hard exclusive reactions and the structure of hadrons,” Prog. Part. Nucl. Phys. **47**, 401 (2001)

[Gra98] G. Graw; “Beam Induced Proton and Electron Depolarisation in Longitudinal and Transverse Magnetic Holding Fields along the Hermes Target Cell”, Hermes Target Internal Report, (1998).

[Hae67] W. Haeberli; *Ann. Rev. Nucl. Sci.*, **17 (1967)**, 373.

[Hen98] M. Henoch; “Interpretation der Polarisationsmessungen am polarisierten Wasserstofftarget des Hermes-Experiments”, Diplomarbeit, Westfälische Wilhelms Universität Münster.

[Hen03] M. Henoch; “Absolute Calibration of a Polarized Deuterium Gas Target”, PhD Thesis, Friedrich-Alexander-Universität Erlangen-Nürnberg, 2002.

[Her93] The Hermes Collaboration; Hermes Technical Design Report, July 1993.

[Her04] A. Airapetian *et al.* [Hermes Collaboration], “Single-spin asymmetries in semi-inclusive deep-inelastic scattering on a transversely polarized hydrogen target,” Phys. Rev. Lett. **94** (2005) 012002 [arXiv:hep-ex/0408013].

[Her05] “The Hermes Polarized Hydrogen and Deuterium Gas Target in the Hera Electron Storage Ring”, A. Airapetian et al, Nucl. Instr. Meth. A **540** (2005) 68

[HER03] DESY; “Super Microscope Hera, Gazing into the Heart of Matter”, DESY information material (2003)

[Kim91] Y. C. Kim, M. Boudart, Langmuir **7**, 2999 (1991).

[Kin91] E. R. Kinney; "Simulations of the Atomic Polarization and Density in the HERMES Polarized Internal Target", HERMES Internal Report 3/90, (1991).

[Koc99] N. Koch; Ph.D. Thesis, Friedrich-Alexander-Universität Erlangen-Nürnberg, March 1999.

[Koc99b] N. Koch and E. Steffens; "High intensity source for cold atomic hydrogen and deuterium beams", Rev. Sci. Inst. Vol. 70, No. 3, pp. 1631-1639

[Kol98] H. Kolster; Ph.D. Thesis, Ludwig-Maximilians Universität München, February 1998.

[Kol97] H. Kolster; Proceedings 7th International Workshop on Polarized Gas Targets and Polarized Beams, Urbana-Champaign.

[Kol03] H. Kolster; Private Correspondence.

[Korn] Korn & Korn; "Mathematical Handbook for Scientists and Engineers", 2nd Edition, *McGraw-Hill*.

[Mar02] M. Marx; "Report on the Transverse Target Magnet", HERMES Target Internal Report.

[Nas01] A. Nass; "Niederdruck Überscallexpansionen", Ph.D. Thesis, Friedrich-Alexander-Universität Erlangen-Nürnberg, (2001).

[Nas02] A. Nass *et al.*, "The HERMES polarized atomic beam source," Nucl. Instrum. Meth. A **505** (2003) 633.

[Pol02] M. V. Polyakov, "Generalized parton distributions and strong forces inside nucleons and nuclei," Phys. Lett. B **555** (2003) 57

[Reg99] D. Reggiani; "Studio ed applicazione di un Bersaglio transversalmente polarizzato per l'esperimento HERMES a HERA", Diploma Thesis, Università degli Studi di Ferrara, December 1999.

[Reg03] D. Reggiani; "Precision Polarisation Measurement of the HERMES H/D Gas Target", Ph.D. Thesis, Università degli Studi di Ferrara, 2003.

[Rit02] K. Rith, "Spin asymmetries in deep-inelastic electron nucleon scattering: Selected HERMES results," Prog. Part. Nucl. Phys. **49**, 245 (2002).

[Sch84] P. Schmuser, "The Electron Proton Colliding Beam Facility HERA," Nucl. Instrum. Meth. A **235**, 201 (1985).

[Sei04] R. Seidl, "Single spin asymmetries in semi-inclusive electroproduction of pions and kaons on a transversely polarized hydrogen target at HERMES", PhD Thesis, Friedrich-Alexander-Universität Erlangen-Nürnberg, 2004.

[Sig03] S. Wang "Active Stabilization of the Transverse Holding Field of the HERMES Polarized Gas Target" HERMES Internal Note 03-033

[Sig03b] S. Wang "Magnetic Flux Density Measurement", HERMES Target Internal Report, 2003.

[Sig04] S. Wang "Improvements of the HERMES Transverse Polarized Hydrogen Target and Calculations of the Sextupole Magnet", PhD Thesis, China Institute of Atomic Energy, 2004.

[Sou98] A. R. de Souza *et al*; Dissociation of N_2 in flowing glow discharge: Influence of H_2. *Eur. Phys. J. AP* **5, 185-189**.

[SH03] E. Steffens, W. Haeberli, "Polarized Gas Targets", 2003 Rep. Prog. Phys. 66 1887-1935

[SMC97] B. Adeva *et al.* [Spin Muon Collaboration (SMC)], "The spin-dependent structure function g1(x) of the proton from polarized deep-inelastic muon scattering," Phys. Lett. B **412** (1997) 414.

[Ye04] Z. Ye *et al.*; Direct measurement of Intra-Beam Scattering in Atomic Beam Sources, to appear in *Nucl. Instrum. and Meth. A*

Acknowledgements

I would firstly like to thank my supervisor Prof. Dr. E. Steffens for his support, advice and patience during my PhD studies. I would also like to thank Prof. Dr. K. Rith for his help and support.

My work in Hamburg was greatly helped by the good atmosphere of the HERMES target group, led by Dr. Paolo Lenisa. I had the pleasure of working with Dr. Mark Henoch, Dr. Alexander Nass, Dr. Davide Reggiani, Dr. Christian Baumgarten, Dr. Giuseppe Ciullo, Dr. Wang Siguang, Dr. Hrachya Marukyan, Ye Zhenyu and Marco Capiluppi, and would like to thank them all for their support and help in writing this thesis. I am particularly grateful for Alexander for his apprenticeship in looking after the ABS, to Zhenyu for his work on the intra-beam scattering in the ABS, and to Davide, Marco and Siguang for keeping my back free whilst I wrote this thesis.

The HERMES target is a rather mature piece of hardware, and that it still works is a tribute to the numerous pioneers who designed, built and optimised it. They are too numerous to mention, but I must individually thank Dr B. Braun, whose wonderfully flexible, adaptable, and undocumented molecular-flow Monte-Carlo I used, Dr. Hauke Kolster for his work on the depolarising resonances, Dr. Norbert Koch, whose work on the ABS test stand was particularly helpful for my studies, and to Prof. Dr. G. Graw, for his excellent work in modelling the beam-induced resonances that was particularly influential for this thesis.

It was a pleasure to work with my Erlangen colleagues Achim Hillenbrand, Martin Raithel, Christian Vogel, Nils Pickert, Markus Diefenthaler, Markus Ehrenfried, Caroline Riedl, Dr. Ralf Seidl, Dietmar Zeiler, Dr. Friedrich Stinzing and Eleonore Hassler.

This thesis would not have been possible without the support of the HERMES management, so I would like to thank Dr. Dirk Ryckbosch for his work as Spokesperson, Dr. Elke-Caroline Aschenauer for her work as Run Coordinator and Spokesperson, Dr. Matthias Hartig and Dr. Pasquale Di Nezza for their work and patience as Run Coordinators. I was immensely helped by the experience and advice of the three Technical Coordinators: Dr. James Stewart, Dr. M. Bouwhuis and Dr. Benedikt Zihlmann.

The most stressful times at HERMES were the access days (whether planned or accidental), and these were made partially bearable by Helmut Hirsemann, Carsten Berg and Volker Prahl, who generally kept their heads whilst I was losing mine.

Dr. Yorck Holler was a constant source of technical help and advice throughout my time at Hamburg.

Ulrike Elschenbroich helped to remove the most glaring mistakes from the section on Transversity, and is in no way responsible for the ones that remain. Marc Beckmann probably also did something to deserve a mention here, but I can't quite remember what.

My parents should also be mentioned for their unrelenting support during my time in Hamburg. I'm sure they would have visited more often if Hamburg wasn't so bleeding flat. Don't worry, I've taken the hint.

Last but not least I would like to thank Sörne Möller, who gave me courage when I

needed it most.

Curriculum Vitae

Personal Details

Name:	Philip Tait
Date of Birth:	16_{th} November 1978
Place of Birth:	Sheffield, England
Nationality:	British
Status:	Single
Parents:	David J. Tait, born 17_{th} February 1947
	Valerie A. Tait, born 15_{th} October 1946

Education

Friedrich-Alexander-Universität Erlangen, Germany September 2001 - Present
Wissenschaftlicher Mitarbeiter
Work on HERMES experiment at DESY in Hamburg

University of York, England 1997-2001
MPhys Degree, Physics with a Year in Europe
First Class Honours
Erasmus year in Erlangen, Germany 1999-2000
Summer Student at DESY in Hamburg, 2000
Masters thesis "Slowing of Visible Light in a Waveguide", 2000-2001.

Eckington Sixth Form, Derbys., England 1995-1997
A level courses: Physics : Grade A
Mathematics : Grade A
Chemistry : Grade A
German : Grade B
General Studies : Grade A

Eckington Comprehensive School, Derbys., England 1990-1995
10 GCSEs